Zinc Oxide Nanostructures: Synthesis, Doping and Growth Mechanism

by

Jinhyun Cho

Department of Electrical and Computer Engineering
Duke University

Date:_______________________
Approved:

____
Jungsang Kim, Supervisor

____
Jie Liu

____
Jeffrey T. Glass

____
Adrienne Stiff-Roberts

____
Martin Fischer

Dissertation submitted in partial fulfillment of
the requirements for the degree of Doctor
of Philosophy in the Department of
Electrical and Computer Engineering in the Graduate School
of Duke University

2013

<u>ABSTRACT</u>

Zinc Oxide Nanostructures: Synthesis, Doping and Growth Mechanism

by

Jinhyun Cho

Department of Electrical and Computer Engineering
Duke University

Date:_______________________
Approved:

____
Jungsang Kim, Supervisor

____
Jie Liu

____
Jeffrey T. Glass

____
Adrienne Stiff-Roberts

____
Martin Fischer

An abstract of a dissertation submitted in partial
fulfillment of the requirements for the degree
of Doctor of Philosophy in the Department of
Electrical and Computer Engineering in the Graduate School of
Duke University

2013

Abstract

Over the past decade, the study of zinc oxide (ZnO) II-VI semiconducting nanostructures has been a burgeoning research area because of this material's unique electrical and optical properties. Despite the promise of its characteristics for numerous applications, usage of ZnO in the fabrication of nanoscale devices on a commercial scale remains a challenge because of our lack of knowledge of the underlying physics and chemistry of nanostructures. Sustainable progress in nanowire manufacturing techniques requires that we first undertake basic studies to address these poorly understood underlying concepts before we embark on applied engineering. If these fundamental studies prove successful, then characterization, fabrication, and large-scale integration of nanostructures that use ZnO could be applied to a range of engineering fields. This doctoral dissertation is primarily concerned with the synthesis and doping required for the creation of novel ZnO nanostructures and the growth mechanisms of such structures. Numerous studies have been made of various kinds of ZnO nanostructures. However, no studies have been reported of systematic theoretical modeling that uses both density functional theory and as-synthesized nanostructures to explain the growth mechanisms involved in these devices. First, sulfur-doped ZnO nanostars, synthesized through a hydrothermal method, will be discussed. This section uses *ab initio* simulations in discussing the synthesis of novel ZnO nanostructures and

their proposed growth mechanisms. Moreover, this discussion also addresses the optical properties of ZnO structures that cause sulfur doping to enhance their emission of green light. The next section introduces a novel synthetic methodology to reliably produce well-aligned vertical ZnO nanowire arrays on amorphous substrates. Vertical alignment of nanowires significantly improves the performance of devices like LEDs and solar cells. Because these vertically aligned arrays have historically been made using sapphire substrates that hinder their commercialization, substantial effort has been invested in using ZnO nanocrystal seeds to grow vertically aligned ZnO nanowires on silicon substrates. Well-known synthetic methods, such as zinc acetate dissolved in methanol or zinc acetate combined with sodium hydroxide (or potassium hydroxide), have typically been used in pursuit of this goal without a detailed understanding of the mechanisms of seed creation. The consequence of this lack of knowledge has been inconsistent reproducibility in growing vertically aligned nanowires on silicon substrates. This discussion includes the details of mechanisms that explain the why and how of creation of vertical/misoriented ZnO nanocrystal seeds on silicon substrates. In addition, a preferential c-axis-oriented ZnO nanocrystal seed has been successfully synthesized using a solution composed of ammonium hydroxide (NH_4OH) and zinc acetate ($Zn(O_2CCH_3)_2$). Lastly, the synthesis of sea urchin-like microstructures known as ZnO sea urchins will be introduced. Among the various kinds ZnO structures, the ZnO sea urchin is a integrated structure composed of a 3-D microsphere and 1-D nanowires. Dye-

sensitized solar cells (DSSCs) made of ZnO sea urchins have shown a higher power conversion efficiency than planar nanowires. This is because ZnO sea urchins have a higher surface area per unit of volume than planar nanowire arrays. This larger surface area allows larger amounts of dye to access the semiconducting nanowires. We have synthesized the sea urchin structures composed of ZnO_xP_y microspheres, a mixed of zinc phosphide (Zn_3P_2) and ZnO phase, encapsulated in an array of ZnO nanowires. Synthesis of these interesting structures was achieved without resorting to the prefabricated 3-D microsphere templates that other groups used in previous studies. This new approach to the synthesis of ZnO sea urchin structures was accomplished by simply adding Zn_3P_2 powder to the C (graphite) and ZnO source powders in a chemical vapor transport method. The ZnO sea urchin's material properties and growth mechanism will be characterized and discussed in detail.

Dedication

I dedicate this dissertation to my parents and my wife, Jongmi Joanna Choi.

Contents

List of Tables

List of Figures

Acknowledgements

I am deeply appreciative of all the people who helped and encouraged me while I have pursued my doctoral studies.

First, I thank my two mentors, Professors Jungsang Kim and Jie Liu for their guidance, support, and commitment to my academic success. During my graduate studies, they have showed me how to be a true scholar and how to cultivate the proper frame of mind for research. I always have been touched by their passion and dedication to science. They have truly been like my academic parents.

I owe a debt of gratitude to my dissertation committee of Professors Jeffrey T. Glass, Qing H. Liu, Adrienne Stiff-Roberts, and Martin Fischer for their time and mentoring over the course of my studies and the labor of writing this dissertation.

Second, I want thank all of my group members, both in the Department of Electrical and Computer Engineering and in the Department of Chemistry. I appreciate the warm friendship and encouragement of Dr. Caleb Knoernschild, Rachel Noek, and Emily Mount who have always lifted my spirits when I have been troubled. I am grateful for all the help and kindnesses of Dr. Teahyun Kim, Dr. Felix Lu, Dr. Peter Maunz, Dr. Kyle McKay, Dr. Byoung-Soo Choi, Dr. Seo Ho Youn, Dr. So-Young Baek, Hui Son, Rayn Clark, Stephen Crain, Daniel Gaultney, Andre van Rynbach, and Seongphill Moon.

My chemistry lab mates — Dr. Hongbo Zhang, Dr. Pan Li, Jay Gee Simmons Jr., Yingweng Cheng, Yue Cai, Jinghua Li, Gyeonghee Lee, Danielle E. Gorka, Jennifer K. Wedebrock, Xiao Zhang, Carlos Blanco, and Aubrey Temple — have been invaluable allies, friends, and colleagues. Without their help, I would not have reached this finish line.

Numerous people have been of great help to me in both my private and academic life. Among them are Dr. Chul-Jin Lee, a roommate and old high school friend, Dr. Sehoon Keum, Professor Hyun-Seok Kim, Dr. Seungkirl Ahn, Dr. Il Hwan Kim, Professor Byoung-Eun Kim, Dr. Kirkil Choi, Dr. Junsu Kang, Professor Kinney H. Kim, Professor Ho Jae Lee, Professor Sang Eun Shim, Professor Sung Phil Chang, Dr. Tong-Ho Kim, Dr. Soojeong Choi, Dr. Jiil Choi, Dr. Soryong Chae, Dr. John V. Foreman, Professor Henry O. Everitt, and Dr. Congwen "Evonne" Yi.

Finally, I owe my deepest thanks to my parents, wife, family, and my old friends Sungmin Park, Eui Lim and Sejin Lim. I especially thank my wife, Jongmi Joanna Choi. Without their love and prayers, I could never have arrived at this milestone in my life.

1. Introduction

My research topic deals with controlled synthesis, doping, and growth mechanism of quasi one-dimensional (1-D) zinc oxide (ZnO) nanostructures for future nanotechnology. This chapter introduces the historical background and motivation for this research and explains why ZnO nanowire is a promising material for future solid-state lighting. Accordingly, I will discuss the bottom-up approach that is the new paradigm for synthesizing ZnO nanowires, proceed to the uniqueness of 1-D nanowire for highlighting dimensionality of structure, and, third, cover ZnO material characteristics and suitability for solid-state lighting.

1.1 Zinc Oxide (ZnO) Nanostructures for Future Nanotechnology

For 50 years, what is known as the top-down approach has dominated microelectronics[1,2]. The concept underlying this "top-down" approach refers to the use of lithography to resize something of bulk down to the micrometer realm[2]. This has long been the most common way to achieve micro-scale devices. Using this top-down approach, the channel length of a complementary metal-oxide-semiconductor (CMOS) has been continuously scaled down. Moore's First Law predicted this trend: Feature sizes would be reduced by 0.7 times every 18 months[2,3,4]

However, the top-down approach currently faces fundamental technological challenges. One of these is the etching process invariably inflicts both surface and crystallographic damage on the materials[5]. As a consequence, electronics fabricated through traditional scale-down methods degrade over the course of their service in devices[5]. This functional degradation generates a challenge in terms of device design and fabrication. A second fundamental problem is that the light source for photolithography is physically limited in wavelength. Feature sizes approaching 10 nm requires wavelength considerably shorter than the current minimum of 60 nm[6]. Moreover, as smaller mask sizes are used in the photolithography process, diffraction between UV light and these masks increases. This intensified diffraction, according to industry predictions, will rule out the possibility of precise patterning for a few nanometer sizes. High cost is the final challenge to continuation of the top-down approach and is a practical problem more than a fundamental one.

This cost problem parallels Moore's First Law in confirming his Second Law, which predicts just such a financial challenge: The cost of building fabrication lines doubles every 36 months[6]. The scale-down method embodied in the top-down approach inevitably needs complex processes and equipment to precisely fabricate nanodevices. In terms of economic value, this combination of high cost and complicated fabrication of nanodevices results in high-priced defective products.

Unsurprisingly, the concept of a "bottom-up" approach has been emerging and solidifying as a way to overcome the limitations on physical size that the top-down approach is encountering. This concept consists of using basic components such as atoms and molecules as building blocks in fabricating ever smaller microelectronic devices[1,2]. Because these are basic material components on the angstrom scale, they can be assembled through chemical synthesis and used to build nanodevices without resorting to expensive, complex instruments. Thus, this bottom-up paradigm has no fundamental limitations in terms of size and cost. Devices fabricated through the lithography-independent bottom-up approach also would have fewer defects and internal stresses than those produced through the top-down approach[7-9]. However, this new paradigm faces challenges in both the difficulty of manipulating nano-scaled building blocks to create integrated nanoelectronics and the problem of routinizing their mass production.

Despite the apparent advantages of this bottom-up concept, at this point it must be categorized as an emerging technology. In practical terms, this means that the remarkably successful scaled-down method represented by the top-down approach is likely to be continued in the integrated circuits (IC) industry for some time. This is because, despite the existing and looming challenges to conventional scaling methods, the top-down paradigm routinely supports the mass production of nano-scaled devices that are precise within a few hundred nanometers. Moreover, electron-beam lithography, an alternative to the diffraction limit of photolithography, supports features with a few nanometer sizes despite its high cost and beam drift problem[10].

To date, as mentioned earlier, versatile and reproducible assembly of nanodevices through the bottom-up approach alone remains difficult. Since 2000, nanotechnology has gone through a transition so that currently nanodevices are fabricated through a combination of the top-town and bottom-up approaches[2,11]. Over the course of this transition, consolidating methodology that uses both self-assembly and lithographic techniques has been developed and successfully applied to nanotechnology[11,12]. This consolidation of the top-down and bottom-up approaches is expected to continue indefinitely.

My research uses chemical synthesis, a bottom-up method, for atomic-level control of material composition and structure in the creation of ZnO nanowires. Nanowires usually have a cross-sectional dimension ranging from a few to hundreds of nanometers and a length of several micrometers. Because of their unique structure, nanowires characteristically allow electrons, holes, and photons to propagate freely along quasi one-dimension while prohibiting propagation along two other dimensions[8,13,14]. Since 2000, numerous research groups have invested substantial effort to use semiconductor nanowires to produce nanoscale electrical and photonic devices.

Consequently, significant progress has been made in the form of transistors[15], sensors[16], LEDs[17-21], solar cells[22], photodetectors[23,24], waveguides[25], and lasers[13,14,26,27] .

A couple of good examples demonstrate that 1-D semiconductor nanowires solve the intrinsic problems posed by bulk and thin film structures[13,14]. In the case of a III-V semiconductor, for an LED, epitaxial growth on silicon is an important step toward replacing a costly sapphire substrate with something more financially feasible. With current techniques, the relatively large crystalline lattice mismatch between the InGaN and silicon substrate causes high stresses at their interface that then generates crystal dislocations. These dislocations keep a device from achieving its potential. However, when III-V nanowire is used, the high aspect ratio of its ordered arrays causes less stress at the interfaces and consequently produces better crystallinity. Because of this higher crystal quality, the photons generated in nanowire LEDs have less internal reflection and consequently can achieve higher external quantum efficiency[13,14,21]. Solar cells made by using nanowires are another example. Compared to film structures, nanowires have considerable advantages in charge separation and carrier propagation, key elements for increased energy conversion efficiency[13,14]. Lastly, an interesting lasing phenomenon occurs with highly ordered ZnO or GaN nanowire arrays, in which both end facets of the nanowire serve as nanoscale cavities[13,14,21,26,27].

Despite these promising developments, the nanoscale regime is governed by quantum phenomena whose behavior is poorly understood. Sustainable progress in nanowire manufacturing techniques requires that we address our lack of knowledge of the physics and chemistry of nanostructures through further basic studies before we undertake applied engineering.

In the course of acquiring this knowledge, as a first step, preliminary studies of the growth mechanism of 1-D nanostructures should be completed. It is known that thermodynamically nonequilibrium growth kinetics govern 1-D ZnO nanostructures[28]. However, the details of the operation of this sophisticated growth mechanism are poorly understood. Moreover, as a step toward systematic creation of nanodevices, each nano building block should be synthesized and manipulated for large-scale integration. With a proven growth mechanism as a foundation, the second step should be a predictable and manipulable synthesis for hierarchical assembly. If these two studies prove successful, characterization, fabrication, and large-scale integration of nanodevices using arrays of nano building blocks could be applied to a range of engineering fields[28].

1.2 Doping of ZnO Nanostructures for Solid-State Lighting

1.2.1 Miller-Bravais Index in Wurtzite Crystal Structure

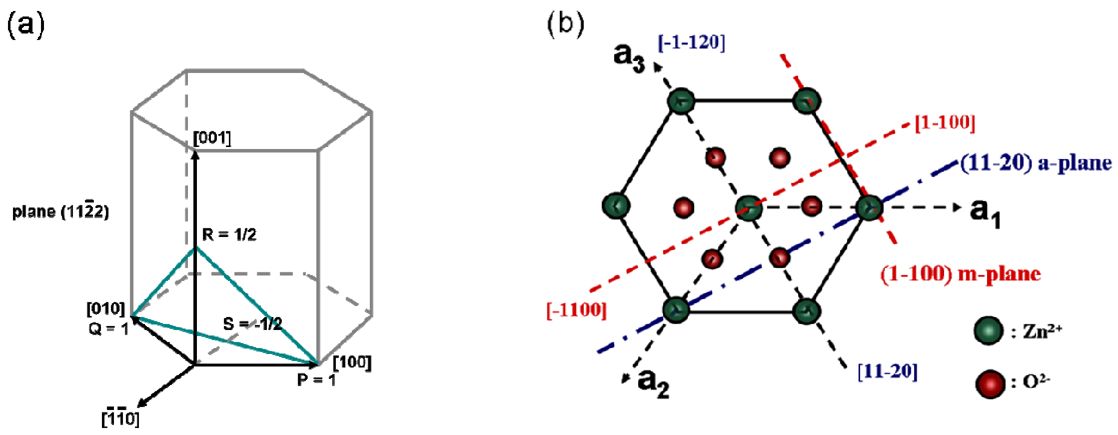

Figure 1.1: (a)[29] The (11$\bar{2}$2) plane; (b)[30] the orientation used in the wurtzite phase as projected along the (0001) basal plane

The Miller-Bravais index, which has four axes and four numbers, [*h,k,j,l*], has been used to indicate planes and directions in a hexagonal wurtzite structure. In this notation system, the first three indices represent the reciprocal number of intersection points on three axes that are 120° apart on the c-plane (basal plane). The fourth index represents the reciprocal number of intersections on the vertical c-axis. If a plane has no intersection points on a specific axis, this index is represented as zero.

For example, as illustrated in 1.3 (a)[29], a (11$\bar{2}$2) plane has intersection points, (1, 1, -1/2, 1/2), on the four axes, respectively. Therefore, the inverse numbers of these intersection points are used for the plane orientation. The a-plane shown in Figure 1.3

(b)[30] has intersection points (1, 1, -2) on the three axes without an intersection point on the vertical axis. Thus, the a-plane is expressed as $(11\bar{2}0)$ in this case.

In four-digit notation, the sum of the first two indices must be equal to the opposite signed third index. Therefore, this can be abbreviated through three-digit notation, which has no third index. Because of their anisotropic fast growth feature, the c- plane, a-plane, and m-plane shown in Figure 1.4 are the most notable facets of ZnO.

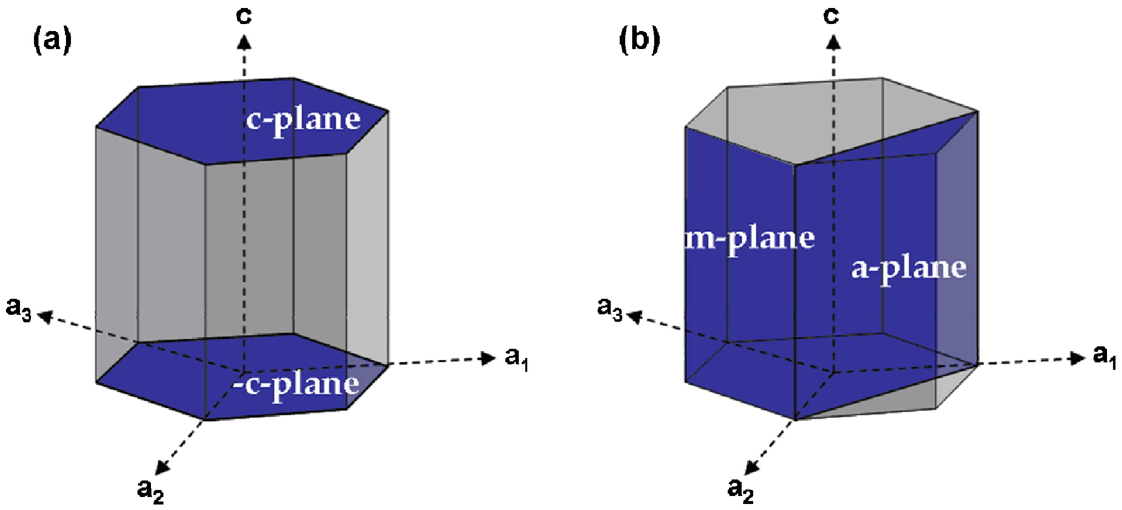

Figure 1.2 [31]: (a) polar + c-plane (0001) and – c-plane $(000\bar{1})$ and (b) the nonpolar m-plane $(1\bar{1}00)$ and the a-plane $(11\bar{1}0)$

1.2.2 ZnO Crystal Structural and Material Properties

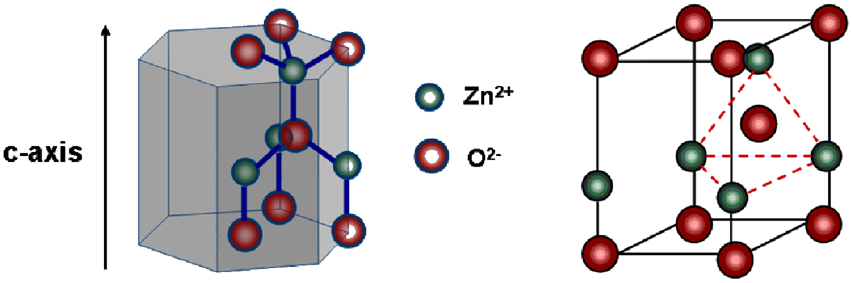

Figure 1.3[32]: Zinc oxide (ZnO) hexagonal wurtzite structure and its polarization

Many reports have been made on various kinds of 1-D nanostructures among II-VI or III-V heterogeneous semiconductors[2,33]. Among these materials, in terms of material properties, zinc oxide (ZnO), a II-VI metal oxide semiconductor, appears to be the most interesting and promising. ZnO is a wurtzite structure having noncentral symmetry and a hexagonal unit cell with a lattice parameter of a=3.2496, c=5.2065 Å[32] . It is also known to be a piezoelectric property, and this enables ZnO to be used for electromechanical coupled sensors and transducers[34,35]. The wurtzite structure is uniquely qualified for functional materials, including ZnO, GaN, AlN, CdSe, and ZnS.

As can be seen in Figure 1.3, the crystal structure of ZnO consists of alternating planes along the c-axis, thus stacking up tetrahedrally coordinated zinc cations (Zn^{2+}) and oxygen anions (O^{2-})[34,35] The Zhong Lin Wang group established a detailed theory to explain the growth kinetics and charge distribution in ZnO that account for its various morphologies[32]; According to their theory[32], ZnO crystallography uniquely distributes cations and anions in the ZnO crystal, although the crystal appears neutral. This phenomenon generates a polar surface comprised of positively charged or negatively charged ions. In ZnO, the c-planes (basal planes), the most common polar surface, is separated between the positively charged Zn-(0001) and negatively charged O-$(000\bar{1})$ planes. These surfaces with opposed charges generate a normal dipole along the c-axis and spread the surface energies. The ionic charge distribution on the facets determines the interaction energy between them and tends to minimize any electrostatic energy. This is regarded as a pivotal cause in explaining the creation of numerous nanostructures in materials influenced by polar surfaces. The side surfaces, which are $\{01\bar{1}0\}$, $\{2\bar{1}\bar{1}0\}$, are nonpolar surfaces because of their lower surface energy compared with {0001}[32,33].

There are also three types of fast directions that are determined by surface polarity. These are <0001>, $<0\bar{1}\bar{1}0>$, and $<2\bar{1}\bar{1}0>$[33]. These anisotropic different fast growth directions, which under certain conditions determine the relative activity in various growth facets, induce the various morphologies encountered in nanostructures, such as nanohelices, nanorings, nanopropellers, nanocombs, nanodisks, and nanosprings[33].

1.2.3 Potential and Challenges of Doping ZnO: Solid-State Lighting

Awareness of limited fossil fuel reserves has motivated academia and industry to emphasize research into new energy sources generally referred to as “green technology.” These include solar cells, nuclear power, and wind power. Although tapping new sources of energy is important, it also is essential to increase the efficiency of existing electrical devices.

Table 1.1: Comparison of features of various lighting sources commercialized in the current market; OLED (organic light-emitting diode), HID (high intensity discharge lamp), CFL (compact fluorescent lamp) (Reference: Solid-State Lighting Research and Development, Multi-Year Program Plan, U.S. Department of Energy (April, 2013))

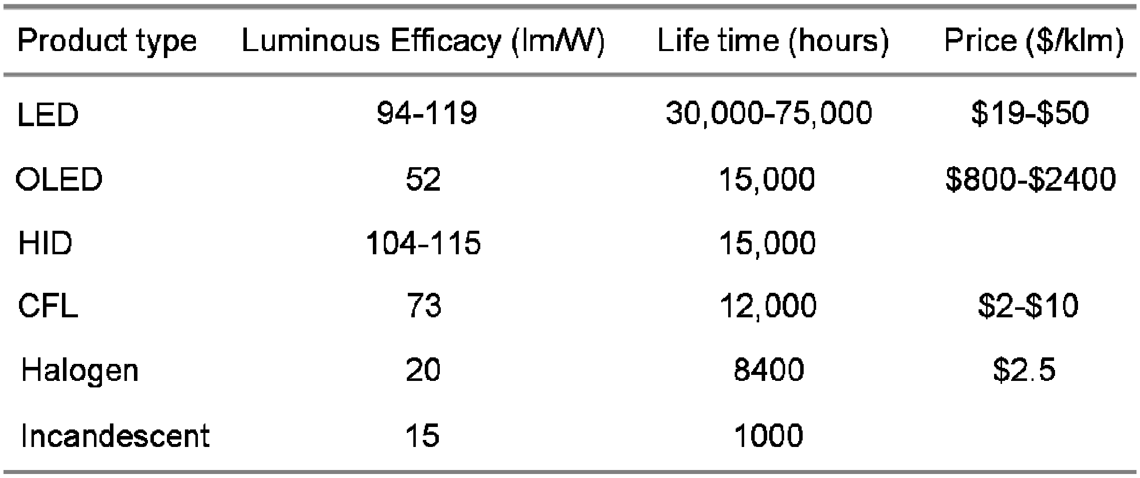

Product type	Luminous Efficacy (lm/W)	Life time (hours)	Price ($/klm)
LED	94-119	30,000-75,000	$19-$50
OLED	52	15,000	$800-$2400
HID	104-115	15,000	
CFL	73	12,000	$2-$10
Halogen	20	8400	$2.5
Incandescent	15	1000	

Since ancient times, humans have sought and used sources of light, ranging from fire through incandescent bulbs and fluorescent lamps to the more recent use of LEDs[36,37]. In modern society, lighting accounts for a large part of the energy consumed. According to an estimate by the U.S. Energy Information Administration (EIA) in 2011, for example, lighting consumed 12% of the total energy used in the U.S. and accounted for 13% of residential energy consumption and 21% in the commercial sector. Table 1.1 summarizes the features of commercialized lighting sources in both the conventional way and in terms of a solid-state system. Here, luminous efficacy is defined as the ratio of luminous flux (or visible light output) to unit input power, i.e. the efficiency with which the visible light was produced in terms of consumption of electricity[38]. Because maximum luminous efficacy is 683 (lm/W), this value is equivalent to 100% luminous efficiency. By this measure, LEDs have a 13-17% efficiency rating, which is higher than the 10% of compact fluorescent lighting and the 2% of incandescent[36,37].

However, although the price of LEDs has decreased significantly, LEDs still are more expensive than compact fluorescent lamps. Moreover, most LEDs have a single color[37] and still need improvement in luminous efficiency. To overcome these shortcomings, scientists have recently focused their attention on white light-emitting diodes (white LEDs) that can cover the entire visible wavelength from 400 nm to 800 nm. The current white LEDs use a combination of blue light from indium gallium nitride (InGaN) and yellow light re-emitted from the phosphor coating in the cap of the LEDs[39,40]. Although human eyes register this blend as white light, this quasiwhite light still carries a low efficiency rating. The Department of Energy (DOE) has a goal of 32% luminous efficiency (224 lm/W) in cost-effective white LED packages by 2025[41].

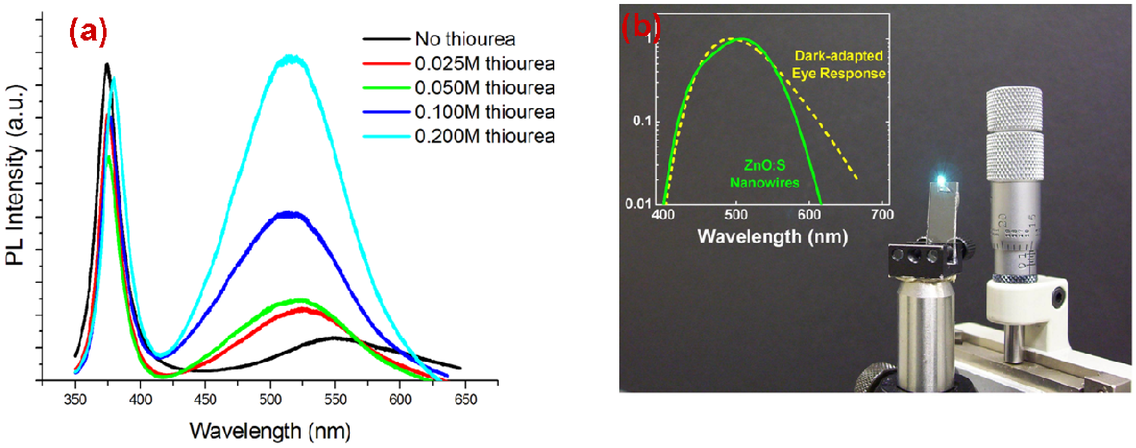

Figure 1.4: (a) Sulfur-doped ZnO nanowires photoluminescence spectra; (b)[37,42] comparison of the sulfur-doped ZnO photoluminescence spectra to the scotopic human eye response under dim light conditions

In terms of this DOE goal, ZnO nanowire is a suitable material for white LEDs and generally exhibits both excitonic band-edge emissions ranging from 3.236 eV to 3.307 eV[43] and visible green emissions generated by intrinsic defects. Photoluminescence (PL) in ZnO powders doped with sulfur (S), selenium (Se), and tellurium (Te) emit light covering the entire visible range.

As demonstrated in Figure 1.4 (a), PL in S-doped ZnO nanostructures also displayed green light enhancement as increments of thiourea (CH_4N_2S) concentration. Furthermore, as can be seen in Figure 1.4 (b), the PL spectrum from S-doped ZnO is well suited for the scotopic human eye response under dim light conditions[37,42]. Consequently, the ZnO nanostructure could be a strong candidate for white LEDs with high luminous efficiency.

Used as a wide II-VI direct band-gap semiconductor (3.37 eV), ZnO has long been regarded as a suitable ultraviolet (UV) and blue LED. Among the rare direct wide band-gap semiconductors, each material has unique drawbacks that result in narrowed options. For example, silicon carbide (SiC) (2.86 eV) has a low luminous efficiency, and zinc selenide (ZnSe) (2.7 eV) has a reputation for early failure in high voltage uses[37,44,45].

In contrast with the above materials, ZnO has several intrinsic advantages for use with optoelectronic devices. In terms of such optoelectronic devices as laser diodes (LDs), achieving high gain in lasing action has conventionally required the high density of electron-hole-plasma (EHP)[26]. However, this high EHP concentration inevitably causes inefficient high threshold voltage. Another approach to effective lasing action uses exciton recombination. If at room temperature the exciton binding energy is considerably greater than the thermal energy (26 meV), the lasing action can be even more efficient[26]. In terms of these specifications, ZnO exciton binding energy (60meV) exceeds that of GaN (24 meV) and room-temperature thermal energy (26 meV)[26,33]. As a result, ZnO exhibits strong band-edge excitonic emissions and efficient lasing action at room temperature[26,33]. Thus, because of these advantages, ZnO has routinely been compared with the III-V direct GaN (3.4 eV) semiconductor and its alloys such as InGaN or AlGaN, which have dominated the current LEDs market.

ZnO has other advantages, namely the feasibility of low-cost mass production. In my experiments, I readily created ZnO micro- and nanostructures through a simple chemical vapor deposition (CVD) system. In contrast, GaN typically can only be fabricated at high cost and with complex instruments in molecular beam epitaxy (MBE) or metal-organic CVD (MOCVD) systems.

Moreover, ZnO is more durable in LEDs than GaN[37]. When GaN LEDs are exposed to air, they are easily oxidized over time. This oxidation restricts their lifetime to about 25,000 hours, considerably less than what can be expected with ZnO, which is an intrinsic metal oxide material[46]. Lastly, ZnO is an eco-friendly material. In our daily life, we can easily observe numerous ZnO applications such as in tires, cosmetics, food additives, pigments, and medicines[42,47]. Because it is eco-friendly, ZnO transparent glass is expected to replace conductive glass made with indium tin oxide (ITO), which is toxic. Finally, ZnO resists high-energy radiation, a characteristic highly desirable in space applications[33].

Nanostructured ZnO promises to add unique advantages, such as those mentioned above with ZnO, in either film or powder form[37]. These additional advantages are, first, 1-D nanostructure is a more efficient platform to confirm the increments of dopants and relates with the intensity of the emitted photons; second, films made of nanowires have less of a crystalline boundary than films made of ZnO powder. Thus, we can expect higher conductivity in films made using nanowires. Third, a nanostructure permits fabrication of flexible devices without degrading their performance. Fourth, the size of a 1-D nanowire is well matched with the wavelength of an emitted photon, facilitating the extraction of photons with less internal reflection.

In particular, nanowire stands out in its capability to increase luminous efficiency. For instance, nanowire LEDs are expected to be used for integrated nanophotonics, microscale displays, optical storage, and biological analysis[13]. Compared with current InGaN-based LEDS made using a 2-D quantum well, core-multishell InGaN-based nanowire LEDs have shown estimated gains in external quantum efficiency (EQE) of 5.8% at 440 nm and 3.9% at 540 nm[13,14,48]. These promising results created the impetus to investigate another type of nanostructural material, ZnO, which has long been touted, because of its promise as a UV and blue emitter, as an alternative material for making even more efficient and longer lasting LEDs.

Table 1.2: P-type doping in ZnO in the publications: this table was made by David C. Look and his colleagues[49,50]

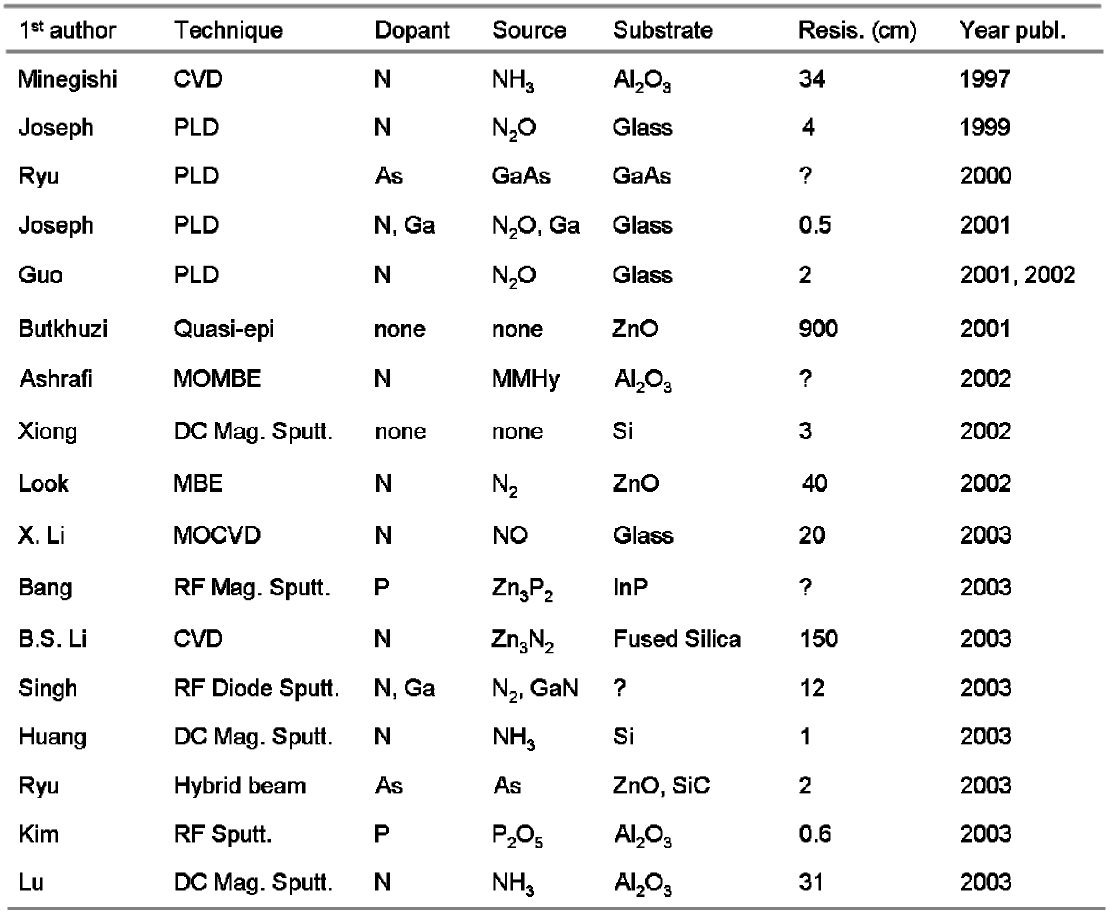

1st author	Technique	Dopant	Source	Substrate	Resis. (cm)	Year publ.
Minegishi	CVD	N	NH_3	Al_2O_3	34	1997
Joseph	PLD	N	N_2O	Glass	4	1999
Ryu	PLD	As	GaAs	GaAs	?	2000
Joseph	PLD	N, Ga	N_2O, Ga	Glass	0.5	2001
Guo	PLD	N	N_2O	Glass	2	2001, 2002
Butkhuzi	Quasi-epi	none	none	ZnO	900	2001
Ashrafi	MOMBE	N	MMHy	Al_2O_3	?	2002
Xiong	DC Mag. Sputt.	none	none	Si	3	2002
Look	MBE	N	N_2	ZnO	40	2002
X. Li	MOCVD	N	NO	Glass	20	2003
Bang	RF Mag. Sputt.	P	Zn_3P_2	InP	?	2003
B.S. Li	CVD	N	Zn_3N_2	Fused Silica	150	2003
Singh	RF Diode Sputt.	N, Ga	N_2, GaN	?	12	2003
Huang	DC Mag. Sputt.	N	NH_3	Si	1	2003
Ryu	Hybrid beam	As	As	ZnO, SiC	2	2003
Kim	RF Sputt.	P	P_2O_5	Al_2O_3	0.6	2003
Lu	DC Mag. Sputt.	N	NH_3	Al_2O_3	31	2003

Despite its numerous outstanding material advantages, ZnO has not yet been commercialized in the current LED market. The main bottleneck is the difficulty of p-type doping in ZnO. In order to fabricate LEDs, a p-type semiconductor that is reproducible, stable, and has a high hole-concentration is mandatory for the p-n junction[49,50]. In general, undoped ZnO has n-type conductance because of such intrinsic defects as oxygen vacancies (V_o), zinc interstitials (Zn_i), and zinc vacancies (V_{Zn})[33]. High quality undoped ZnO shows an electron concentration of mid-10^{16}/cm^3 and mobility of 225 cm^2/V.s at 300 K[49,50].

Over the past 30 years, many groups have tried to solve the p-type doping problem in ZnO. They have frequently failed. In 1997, Minegishi *et al.*[51] reported nitrogen (N) doped p-type ZnO using a CVD system. In their report, hole concentration and mobility as measured by the Hall effect were 1.5×10^{16}/cm^3 and 12 cm^2/V.s, respectively[49,50]. Subsequently, p-type doping trials have been undertaken by others[49]. Table 1.2 summarizes efforts to make p-type ZnO. To measure p-type conductivity, the Hall effect measurement has typically been used and requires that strict conditions ($p\mu_p^2 > n\mu_n^2$) must be met to discern the positive Hall voltage[49,50]. However, although measurement of the Hall effect is credible, the tiny Hall voltage is sensitive to noise interference and the difficulty of making a p-type ohmic contact often produces an n-type signal or an extremely high p-type conductance[49,50]. Therefore, resistivity is alternatively used to evaluate the quality of a p-type ZnO once p-type conductance is proved, as shown in Table 1.2.

In theoretical calculations using density functional theory (DFT), nitrogen has been used for a shallow acceptor whose acceptor energy level lies at 0.40 eV above the valence band[49,50,52]. Nitrogen also has a similar ionic radius with oxygen. Thus, nitrogen was mainly used as a dopant, as shown in Table 2. In DFT, phosphorous (P) and arsenic

(As), respectively, show much deeper acceptor energy levels of 0.93 eV and 1.15 eV above the valence band[49,50,52]. However, contrary to what was predicted, p-type ZnO made using P and As achieves good results[53,54]. Thus, it is still controversial which dopant in Group V is the best choice for p-type doping in ZnO. Group I elements such as lithium (Li), sodium (Na) and potassium (K) were also investigated as candidates for p-type dopant on the basis of the DFT calculations. Theoretical calculations show much shallower acceptor energy levels above the valence band; 0.09 eV of Li, 0.17 eV of Na, and 0.32 eV of K, respectively[49,50,52]. However, these elements usually do not substitute zinc atoms but create many interstitials, serving as donors. Subsequently, it is known that these interstitials make semi-insulating ZnO[49,50]. Although several reports have claimed success in p-doping ZnO, the credibility of these reports remains suspect[49,50]. They are usually considered to have unreasonable hole concentrations or mobility[49,50]. When p-doping in ZnO has been successful, conversion to p-type conductance has readily reverted to n-type conductance within a few months[50,55,56]. This phenomenon is caused by the self-compensation effect, which is induced by native defects killing acceptors. Nevertheless, the positive aspect is that there is clearly p-doped ZnO, which represents a step forward in this challenge[49,50,55,56].

PL using photoexcitation is a convenient method for verifying the existence of an acceptor energy level in the bandgap. Free excitons, electron-hole pairs generated in a semiconductor after photoexcitation, are usually trapped by defects or impurities and then localized below the lattice temperature of 230 K[42]. Once either an electron or hole of exciton is trapped by donor or acceptor impurities, this trapping generates distinct localization energy by the bound exciton. Thus PL generated from bound excitons is red-shifted as diminutions subtracted from free exciton energy (E_x) to localization energy (E_{loc}) of bound exciton to these donors or acceptors[42]. Because ZnO has a lot of native defects in serving as a donor for crystal, we can identify abundant PL spectra generated from excitons that are free or bound to defects (i.e., donors) or acceptors.

Table 1.3: A list of bound excitons of ZnO at low temperatures, as summarized by Dr. John V. Foreman in Professor Henry O. Everitt's group in Duke Physics[42]. According to Foreman's report, all energy value is averaged based on several publications[57-59], and the standard deviations in parentheses are also expressed from this averaged value. A dash in parentheses means no averaging because of a lack of data.

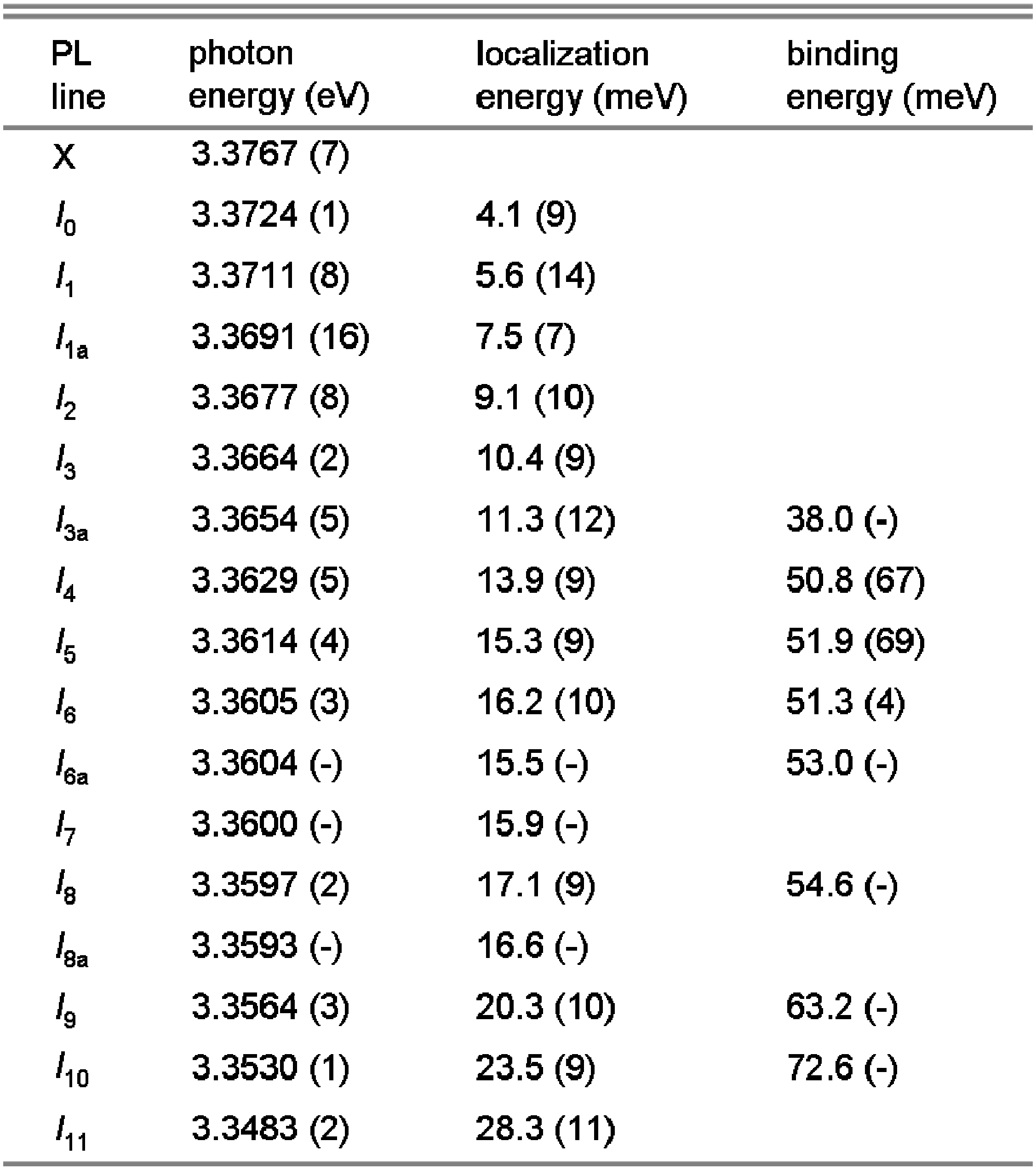

PL line	photon energy (eV)	localization energy (meV)	binding energy (meV)
X	3.3767 (7)		
I_0	3.3724 (1)	4.1 (9)	
I_1	3.3711 (8)	5.6 (14)	
I_{1a}	3.3691 (16)	7.5 (7)	
I_2	3.3677 (8)	9.1 (10)	
I_3	3.3664 (2)	10.4 (9)	
I_{3a}	3.3654 (5)	11.3 (12)	38.0 (-)
I_4	3.3629 (5)	13.9 (9)	50.8 (67)
I_5	3.3614 (4)	15.3 (9)	51.9 (69)
I_6	3.3605 (3)	16.2 (10)	51.3 (4)
I_{6a}	3.3604 (-)	15.5 (-)	53.0 (-)
I_7	3.3600 (-)	15.9 (-)	
I_8	3.3597 (2)	17.1 (9)	54.6 (-)
I_{8a}	3.3593 (-)	16.6 (-)	
I_9	3.3564 (3)	20.3 (10)	63.2 (-)
I_{10}	3.3530 (1)	23.5 (9)	72.6 (-)
I_{11}	3.3483 (2)	28.3 (11)	

Table 1.3 shows the PL transition energies caused by numerous bound excitons from ZnO at low temperature[42]. No consensus exists about the origin of each emission line. I_0-I_2 seems to be made from either B excitons bound to neutral excitons or from A excitons bound to a neutral or ionized donor, but I_3-I_8 are generally generated from neutral donors. I_9-I_{11} seem to originate from neutral donors or acceptors[42].

Table 1.4[55,60,61]: Summary of exciton peaks of PL in p-type doped ZnO at low-temperature

	Bin Xiang *et al.*	Meng Ding *et al.*	Dae-Kue Hwang *et al.*
Free exciton	3.372 eV (P-doped), 3.380 eV (P-doped)	3.375 eV (undoped)	
Acceptor-bound exciton	3.357 eV (P-doped), 3.353 eV (P-doped)	3.353 eV (N-doped)	Bound exiton ~3.356 eV (undoped and P-doped)
Donor-bound exciton	3.360 eV (P-doped), 3.357 eV (undoped), 3.361 eV (undoped), 3.365 eV (undoped), 3.377 (undoped)		Bound exiton ~3.356 eV (undoped and P-doped)
LO-phonon replicas of exciton	3.31 eV (P-doped), 3.24 eV (P-doped), 3.18 eV (P-doped)	3.316 eV (undoped), 3.246 eV (undoped)	
TES (two-electron satellite)	3.31 eV (undoped), 3.24 eV (undoped), 3.16 eV (undoped)		
Free electron from conduction to acceptor level (FA)		3.312 eV (N-doped)	~3.32 eV (P-doped)
Donor-acceptor pair (DAP) transition		3.237 eV (N-doped)	~3.1 eV (undoped), ~3.24 eV (P-doped)
1-LO phonon replica of DAP		3.168 eV (N-doped)	~3.028 eV (undoped)
2-LO phonon replica of DAP			~2.956 eV (undoped)
Green emission	1.67 -1.69 eV (red emission in P-doped NWs)		~2.25 eV (undoped), ~2.4 (P-doped epilayer)

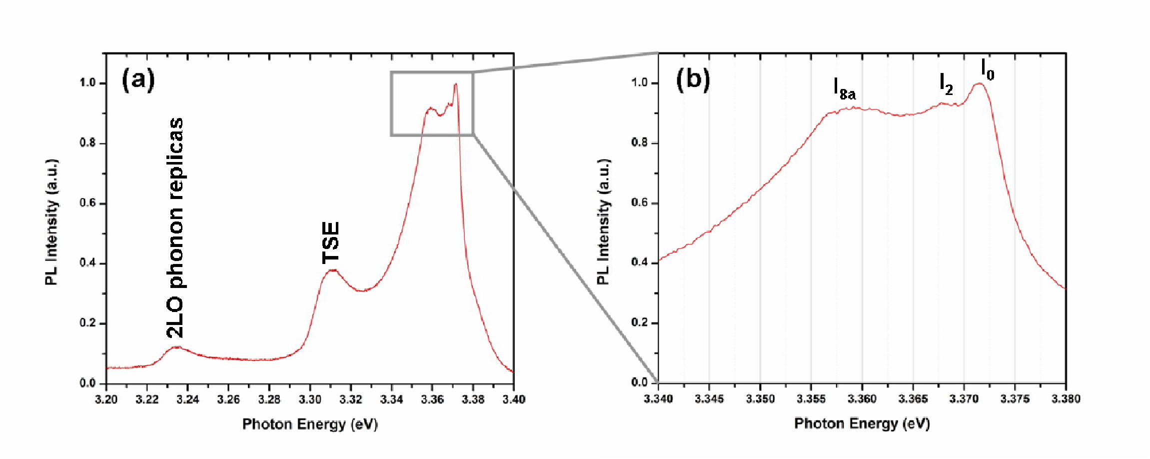

Figure 1.5: (a) PL spectrum of undoped ZnO nanowires measured at 11 K; here 2LO means two longitudinal optical (2LO) phonon replicas and TES means a two-electron satellite; (b) enlarged view in the regions of 3.34 eV-3.38 eV

Although Table 1.3 summarizes the PL spectra of undoped (n-type) ZnO at low-temperature, Table 1.4 summarizes previous reports about the peaks of PL spectrum in p-type ZnO at low-temperature[55,60,61]. In this summary, Bin Xiang *et al.*[55] and Dae-Kue Hwang *et al.*[61] used phosphorous as a dopant for p-type doping, whereas Meng Ding *et al.*[60] used nitrogen as a dopant. Using this information on the low-temperature PL data of ZnO shown in tables 1.3 and 1.4, we can readily compare the free/bound exciton peaks made from our doped samples with the previous data library. This comparison yields insight into whether or not as-doped ZnO is the p-type. For example, Figure 1.5 shows, at 11 K, the PL spectrum of undoped (i.e., n-type) ZnO nanowires grown in our lab by using the CVD-VLS technique. According to information in Table 1.3, we are able to label three peaks in the range of 3.355 eV to 3.375 eV as I_0 (3.3714 eV), I_2 (3.3677 eV), and I_{8a} (3.3591 eV), respectively. We labeled two other peaks as the two-electron satellite

(TES) peak near 3.31 eV, which originated from a donor bound exciton, and the longitudinal-optical (LO) phonon replicas peak near 3.23 eV[57].

So far, we have reviewed the potential of ZnO for achieving more efficient solid-state lighting and the challenges it faces in fulfilling this potential. Hence, my Ph.D. study focuses on examining the synthesis, doping, and growth mechanism of ZnO nanostructures from the viewpoint of solid-state lighting.

To reach this goal, we took the following three strategic steps. First was the establishment of a systematic synthesis methodology for ZnO nanowires. Execution of this step used either the CVD or aqueous solution (hydrothermal) method. Based on the knowledge acquired in this step, controllable doping in ZnO nanostructures and *ab initio* simulation to reveal the growth mechanism were undertaken as the fundamental approach to this problem. Second was the epitaxial growth of vertically aligned ZnO nanowire arrays on silicon wafers. In this step we synthesized and then routinely reproduced ZnO nanocrystalline seeds with normal orientation to the silicon substrates. This epitaxial growth for vertically aligned ZnO nanowires promises to commercialize nanoscale devices on silicon wafers. The third step was the design and synthesis of a 1D nanostructure grown onto 3D microspheres. It was made with the CVD-VLS technique. The growth mechanism of novel nano- and microstructures known as sea urchins were studied. This sea urchin is composed of both ZnO nanowires and ZnO_xP_y microsphere, a combination of Zn_3P_2 and ZnO phase.

1.3 Outline of Document

In this Ph.D. dissertation, I will discuss 1-D ZnO nanowires from a bottom-up perspective and also their optoelectronic applications, especially in solid-state lighting. Chapter 1 introduces this discussion. Chapter 2 enlarges upon it with a discussion of sulfur-doped ZnO nanostars, which are synthesized through the hydrothermal method. This discussion includes their growth mechanism and optical properties of green light enhancement. In Chapter 3, I will introduce the growth mechanism involved in the vapor-liquid-solid (VLS)-CVD method and discuss synthetic methodologies for creating ZnO nanocrystalline seeds with normal orientation to their substrates. In Chapter 4, I will introduce the synthesis and material nature of urchin-like nanostructures known as ZnO sea urchins. These are composed of ZnO nanowires grown on ZnO_xP_y microspheres. The growth mechanism of this structure will also be discussed.

2. Sulfur-Doped ZnO Nanostars: Synthesis and Simulation of Growth Mechanism

2.1 Introduction to Sulfur-Doped ZnO Nanostars

ZnO nanostructures can be prepared by various growth processes, including radio frequency (RF) magnetron sputtering, molecular beam epitaxy (MBE), pulsed laser deposition (PLD), chemical vapor deposition (CVD), and a low-temperature hydrothermal method[33]. Of all these techniques, the low-temperature (e.g., a 90ºC -100ºC environment) hydrothermal method is favored for the fabrication of ZnO nanostructures because of its simplicity[62] and large-scale patterned growth[63]. In this chapter, we present bottom-up synthesis, spectroscopic characterization, and *ab initio* simulations of star-shaped hexagram zinc oxide (ZnO) nanowires. The ZnO nanostructures were synthesized by a low-temperature hydrothermal growth method. The cross section of the ZnO nanowires transforms from a hexagon to a hexagram when sulfur dopants from thiourea ($SC(NH_2)_2$) are added into the growth solution, but no transformation occurs when urea ($OC(NH_2)_2$) is added. X-ray photoemission and photoluminescence spectra comparing undoped and sulfur-doped ZnO confirm that sulfur is responsible for these novel morphologies. Large-scale theoretical calculations were conducted to understand the role of sulfur doping in the growth. The *ab initio* simulations demonstrate that the addition of sulfur causes a local change in charge distribution that is stronger at vertices than at edges, leading to the observed transformation from hexagon to hexagram nanostructures.

2.2 Hydrothermal Approach to Growing ZnO Nanostructures

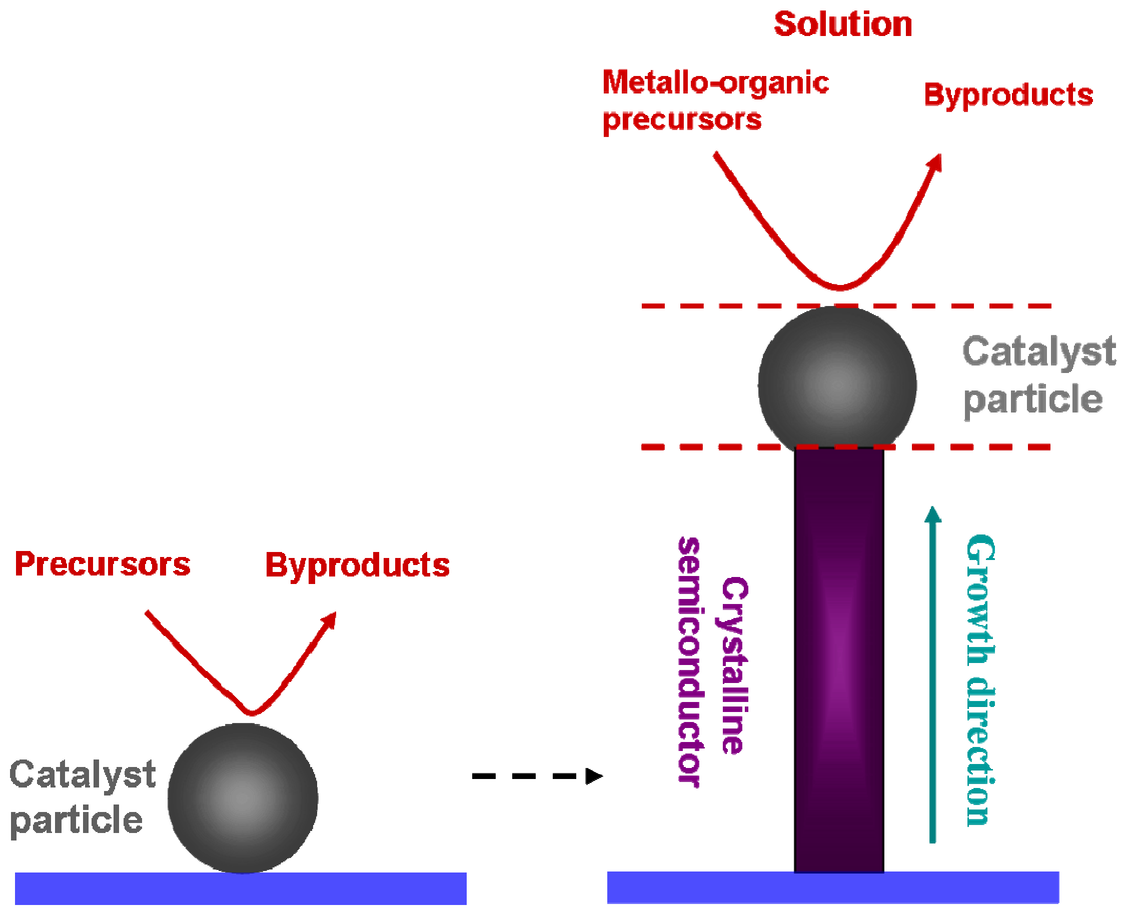

Figure 2.1[64]: Schematic of the growth mechanism of a solution-liquid-solid (SLS) process

Of the various nanowire growth techniques available, the vapor-liquid-solid (VLS) process is generally preferred as the way to fabricate high-quality nanowires[62]. On the other hand, the hydrothermal method, termed a solution-liquid-solid (SLS) process, is the simplest way to grow nanowires because of its accessibility and low-growth environment of 90-100^{o}C. In this method, as-prepared catalyst particles play a role as a seed. Unlike gas-phase precursors involved in the VLS process, in the SLS process solution-phase precursors are supplied to catalytic particles by relatively low thermal energy. In my experiment, an equal molar mixture solution of zinc nitrate, $Zn(NO_3)_2$, and hexamine, $(CH_2)_6N_4$, was used as a nutrient solution. Although the Zn^{2+} ions required for formation of the ZnO nanowires are supplied from $Zn(NO_3)_2$, the necessary O^{2-} ions are supplied from the water in the solution. In these reactions, $(CH_2)_6N_4$ was involved to produce OH^{-}[32]. Moreover, if $(CH_2)_6N_4$ decomposes too quickly and consequently generates a lot of OH^-, the Zn^{2+} ions are quickly precipitated out with a high pH[32]. As a result, the nutrient solutions will no longer support ZnO nanowire growth. ZnO nanowire can be controlled in the five reaction channels listed below[32].

$$(1)\ (CH_2)_6N_4 + 6H_2O \rightarrow 4NH_3 + 6HCHO$$

$$(2)\ NH_3 + H_2O \rightarrow NH_3.H_2O$$

$$(3)\ NH_3.H_2O \rightarrow NH_4^+ + OH^-$$

$$(4)\ Zn^{2+} + 2OH^- \rightarrow Zn(OH)_2$$

$$(5)\ Zn(OH)_2 \rightarrow ZnO + H_2O$$

All of these reactions are in equilibrium and controlled by several parameters such as solution concentration, growth time, and temperature[32]. In general, although precursor concentrations control the density of nanowire, growth time and temperature define the morphology and aspect ratio[32].

2.3 Experimental Procedures to Growing Sulfur-Doped ZnO Nanostructures

The ZnO nanowires are synthesized in solution according to the procedures developed by Greene and Pacholski[62,65]. In this approach, a solution of 0.01 M zinc acetate dihydrate [$Zn(O_2CCH_3)_2(H_2O)_2$ (Fluka, assay>>99.5%)] and 0.03 M sodium hydroxide [NaOH (Fisher Chemical, assay=98.6%)] was first prepared by diluting them in a methanol solvent. Then, 26.32 mL of 0.01 M $Zn(O_2CCH_3)_2(H_2O)_2$ and 13.68 mL of NaOH were combined and stirred for 2 hours at 60°C. The resulting solution was used to create ZnO seed crystals by drop-coating it onto a silicon substrate, rinsing the substrate with methanol, and blow-drying it with air. This drop-coating process was repeated several times. The ZnO seed crystals were then formed by annealing the substrate at 350°C for 20 minutes.

Hydrothermal growth of the ZnO nanowires was achieved by placing the substrate in an aqueous solution containing 0.025 M zinc nitrate [$Zn(NO_3)_2{*}xH_2O$ (Alfa Aesar, assay=99%)] and 0.025 M hexamine (hexamethylenetetramine) [$(CH_2)_6N_4$ (Alfa Aesar, assay=98%)] and heating this solution to 90-95°C for 2 hours. The ZnO nanostars studied in this report were obtained by adding various concentrations of a thiourea [$SC(NH_2)_2$ (Alfa Aesar, assay=99%)] doping solution to the hydrothermal growth process. The thiourea concentration was varied over 0.025 M, 0.05 M, 0.1 M, 0.2 M and 0.5 M, and a control experiment was performed with 0.1 M urea [$OC(NH_2)_2$ (Acros Organic, assay=99%)]. Afterward, all samples were characterized with scanning electron microscopy (SEM, FEI XL 30), photoluminescence spectroscopy (PL), and X-ray photoelectron spectroscopy (XPS, Kratos Analytical Axis Ultra). PL measurements were performed at room temperature using the 325 nm line of a He-Cd laser and a Horiba Jobin Yvon LabRam ARAMIS grating spectrometer.

2.4 Synthesis of Hexagram-Shaped ZnO Nanostars: Morphology and Photoluminescence Variations Caused by Adding Sulfur

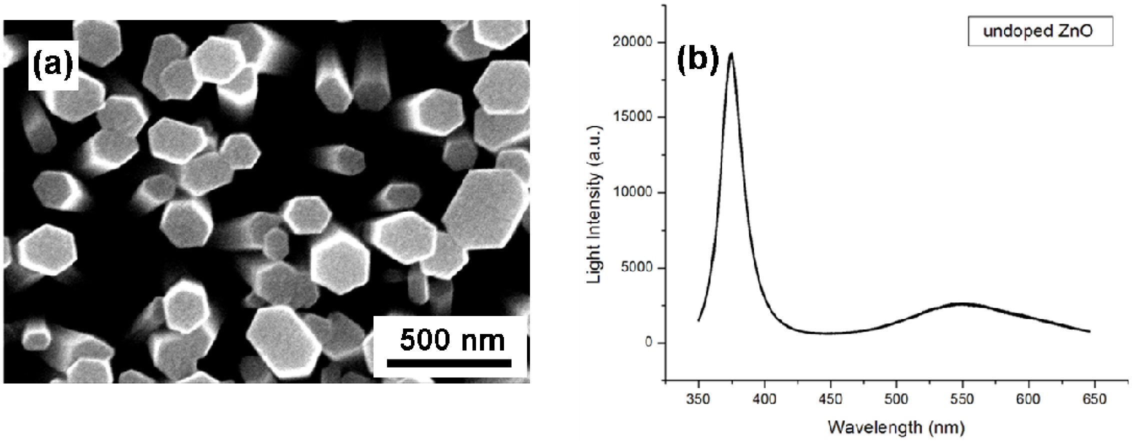

Figure 2.2: (a) A SEM image of as-grown undoped ZnO nanowires: (b) Photoluminescence (PL) spectra of undoped ZnO nanowires. Although the high-intensity band-edge emission is generated from exciton recombination, the low-intensity green emission originates from native defects in ZnO.

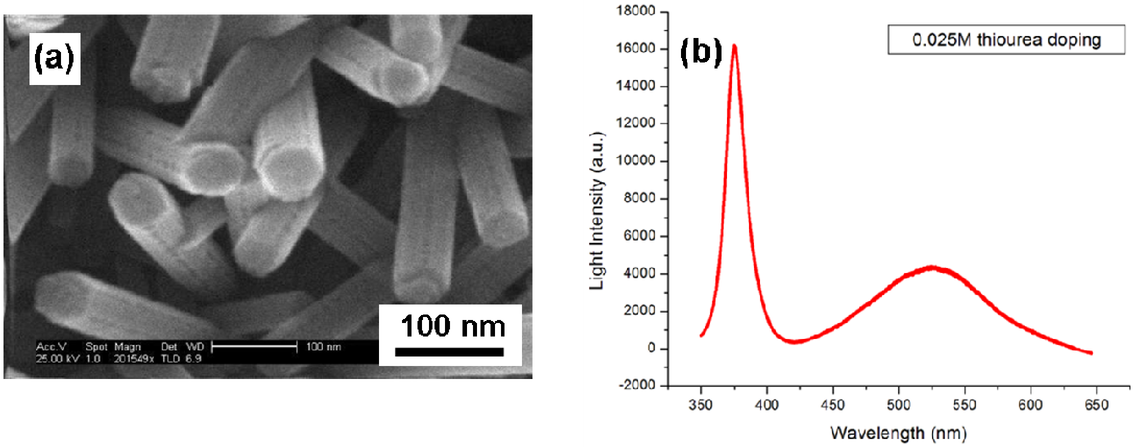

Figure 2.3: (a) A SEM image of an as-grown S-doped ZnO nanostructure. The hexagonal structures slowly become cylindrical: (b) PL spectra of 0.025 M thiourea, ($(NH_2)_2CS$), doped ZnO nanostructures. In these spectra, sulfur (S) doping gradually enhances the green PL emission.

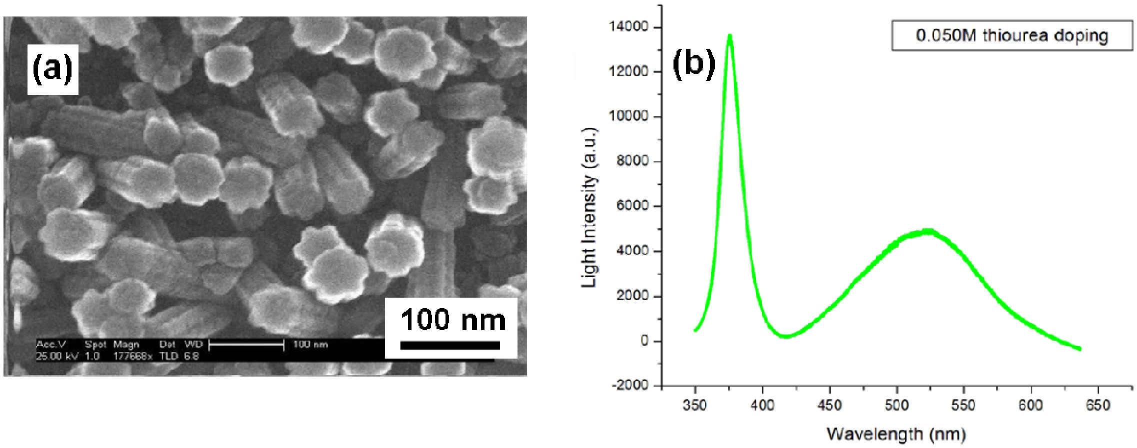

Figure 2.4: (a) A SEM image of an as-grown S-doped ZnO nanostructure. Six arms can be generated to create flower shapes: (b) PL spectra of 0.050 M thiourea, ($(NH_2)_2CS$), doped ZnO nanostructures. In this illustration, sulfur doping enhances the green emission more than does 0.025 M thiourea.

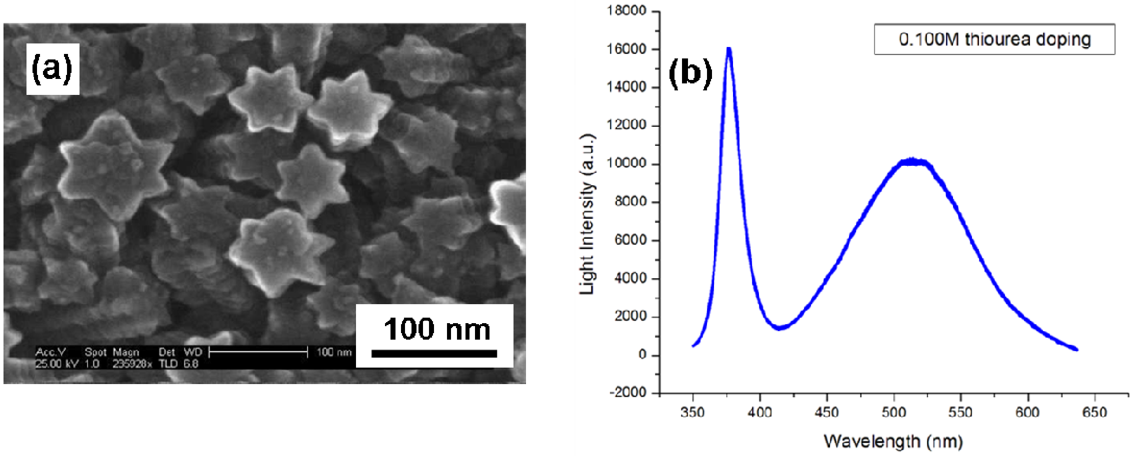

Figure 2.5: (a) A SEM image of an as-grown S-doped ZnO nanostructure. A six-arm hexagram, a nanostar, is clearly shown: (b) PL spectra of 0.100 M thiourea, ($(NH_2)_2CS$), doped ZnO nanostructures. Here, green emission enhancement is remarkably larger than before.

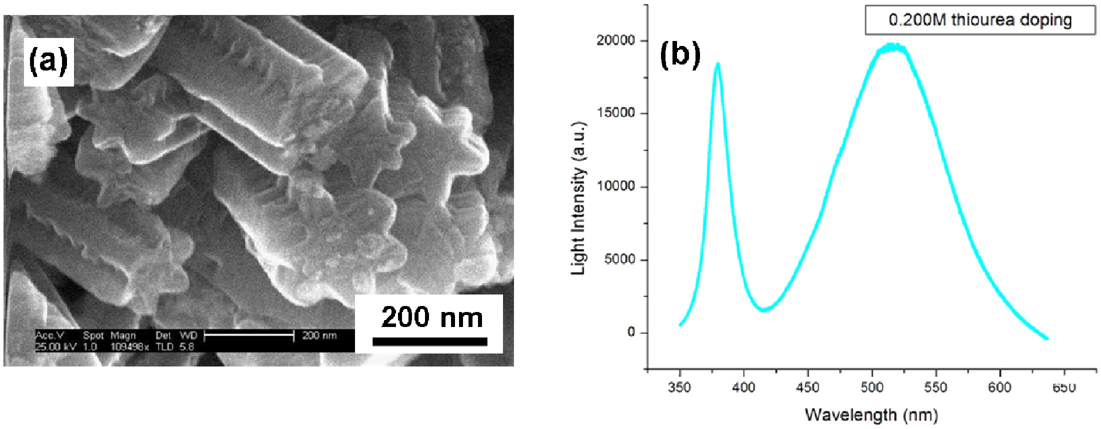

Figure 2.6: (a) A SEM image of an as-grown S-doped ZnO nanostructure. Nanostar morphology is perfectly identified: (b) PL spectra of 0.200 M thiourea, ($(NH_2)_2CS$), doped ZnO nanostructures. Here the green emission enhancement is almost equivalent to the UV emission. The green emission is tremendously enhanced.

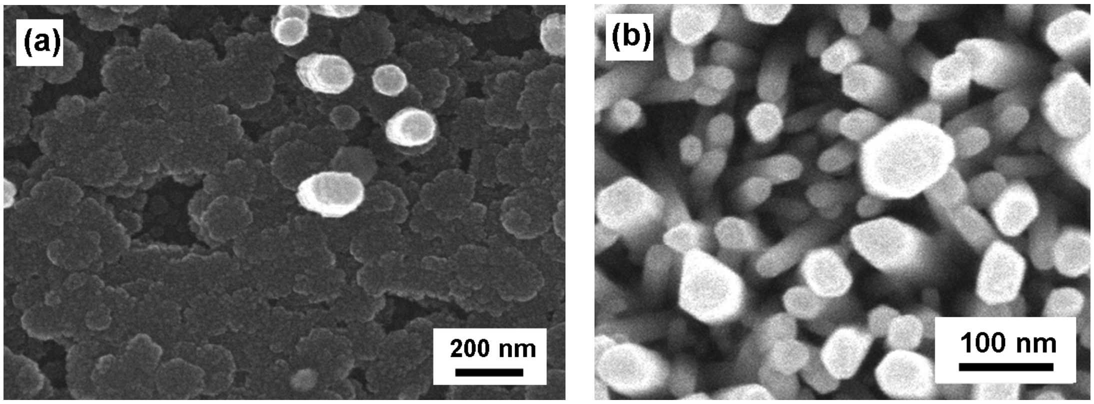

Figure 2.7: (a) A SEM image of ZnO structures obtained by using a high concentration (0.5 M) of thiourea in the reaction mixture. No ZnO nanowires and/or nanostars were observed: (b) A SEM image of ZnO nanostructures synthesized from the combined aqueous solutions of 0.025 M zinc nitrate and 0.025 M hexamine with 0.1 M urea as a control sample.

Systematic evolution from hexagon- to hexagram-shaped nanostructures is observed as the concentration of thiourea is increased in the growth solution. Figure 2.2-2.6 shows SEM images of the resulting nanowires as the concentration of thiourea is increased. Without the addition of thiourea, undoped ZnO nanowires show a typical hexagonal cross section in their top surfaces (Figure 2.2 (a)). Addition of a low concentration [0.025 M] of thiourea leads to the growth of material on the outside edges of the nanowires, leading to a circular cross section (Figure 2.3 (a)). As the concentration of thiourea is increased to 0.05 M (ratio of zinc nitrate, hexamine, and thiourea = 1:1:2), the cylindrical cross section evolves into a flower-like cross section (Figure 2.4 (a)). Upon increasing the concentration of thiourea further to 0.1 M and 0.2 M (ratio of zinc nitrate, hexamine, and thiourea = 1:1:4 and 1:1:8, respectively), ZnO nanostars with a hexagram cross section were generated (Figures 2.5 (a) and 2.6 (a)).

It is noteworthy that the nanowire diameters depend on such growth parameters as seed coating conditions, initial seed size, growth temperature, and kinetics. Increasing the thiourea concentration beyond 0.2 M did not lead to the creation of ZnO nanostars but to a circularly shaped aggregation (Figure 2.7 (a)). This suggests that there is an optimum molar ratio of original nutrient components to thiourea for the growth of hexagram structures. To verify the role of sulfur in the formation of the hexagram nanostars, a control experiment was performed by replacing thiourea with urea ($OC(NH_2)_2$. The molecular structure of urea is identical to thiourea, except that an oxygen atom replaces the sulfur atom. Addition of 0.1 M urea solution does not lead to any deviation from the hexagonal cross section of standard ZnO (Figure 2.7 (b)); this confirms the importance of sulfur in causing the structural change. The detailed optical properties observed in sulfur-doped ZnO nanostructures, shown in Figure 2.2-2.6, will be discussed in next section 2.5.

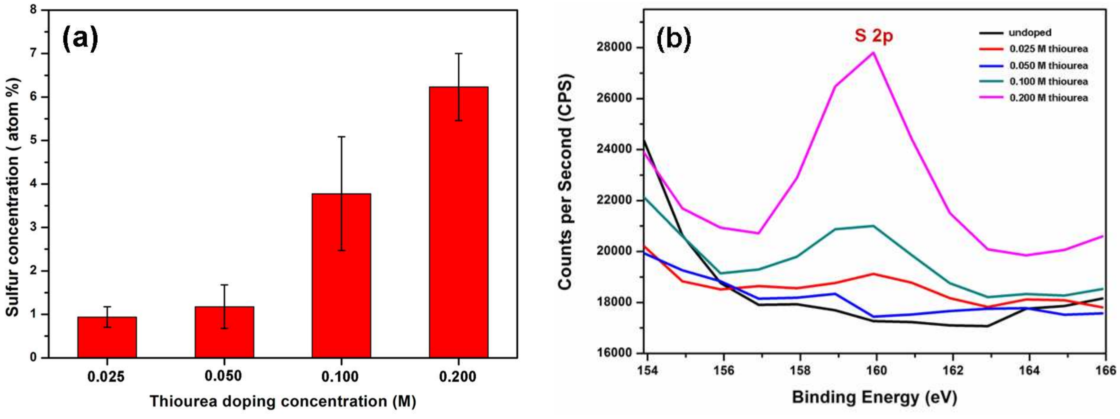

Figure 2.8: (a) Averaged sulfur concentrations of various sulfur-doped ZnO nanostructures in XPS. (b) Core-level XPS corresponding to the sulfur 2p peak for ZnO nanostructures with various concentrations of thiourea.

X-ray photoelectron spectroscopy (XPS) was also performed on these samples for direct verification of the presence of sulfur on the surface of the nanostructures. Figure 2.8 (a) shows the averaged atomic concentrations of sulfur in XPS corresponding to Figures 2.3(a)-2.6(a). As the thiourea concentration is increased in the samples, the average sulfur concentration detected by XPS increases accordingly. In addition, Figure 2.8 (b) shows that the core-level spectra of the sulfur 2p peak gradually increases with increasing sulfur concentration and morphology variation for the samples corresponding to Figures 2.3(a)-2.6(a).

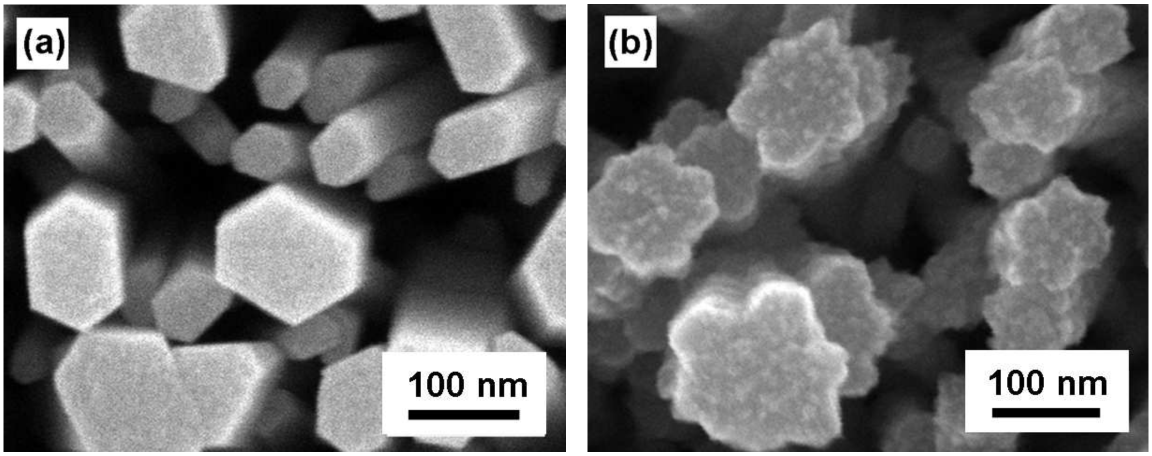

Figure 2.9: (a) and (b) are SEM images of nanowires and nanostars, respectively. To verify the formation mechanism of nanostars, nanowires were grown in advance. These nanowires were re-grown in a mixture of zinc nitrate, hexamine, and thiourea. Figure (b) contains nanostars originated from as-grown nanowires.

The correlation between the cross-sectional shape of the nanostructures and the presence of sulfur suggests that sulfur is responsible for creating the sharp points of the hexagram structure. We propose two mechanisms for the growth of ZnO nanostars: (1) the addition of six triangular attachments, which comprise elements from thiourea and ZnO, to the lateral faces of the hexagonal wurtzite structure; (2) etching the lateral faces of the hexagonal wurtzite structure by using the selective binding characteristics of thiourea. To confirm this, we performed an additional experiment to correlate the sharp points of the hexagram with the presence of sulfur. First, standard hexagonal ZnO nanowires were grown in the original growth solution of 0.025 M zinc nitrate and 0.025 M hexamine. Then, these hexagonal nanowires were either re-grown in an identical growth solution (Figure 2.9 (a)) or in a combined growth solution with 0.1 M thiourea

(Figure 2.9 (b)). The re-grown sulfur-free ZnO nanowires in Figure 2.9 (a) show hexagonal cross sections identical to the original nanowires in Figure 2.2 (a). However, the re-growth of hexagonal nanowires with thiourea produced the hexagram cross-sectional shape as shown in Figure 2.9 (b), suggesting that the sharp points have been "added" to the hexagonal cross section. The ionic structure in ZnO consists of a tight cluster of elements in a metastable top plane (001), a metastable bottom plane ($00\bar{1}$) and six very stable lateral planes (100) perpendicular to the top and bottom[66,67]. This stability, especially in the six lateral faces of the wurtzite structure, also corroborates the first growth mechanism by preventing any etching that would accompany the second hypothesis.

2.5 Optical Properties of Sulfur-Doped ZnO Nanostars

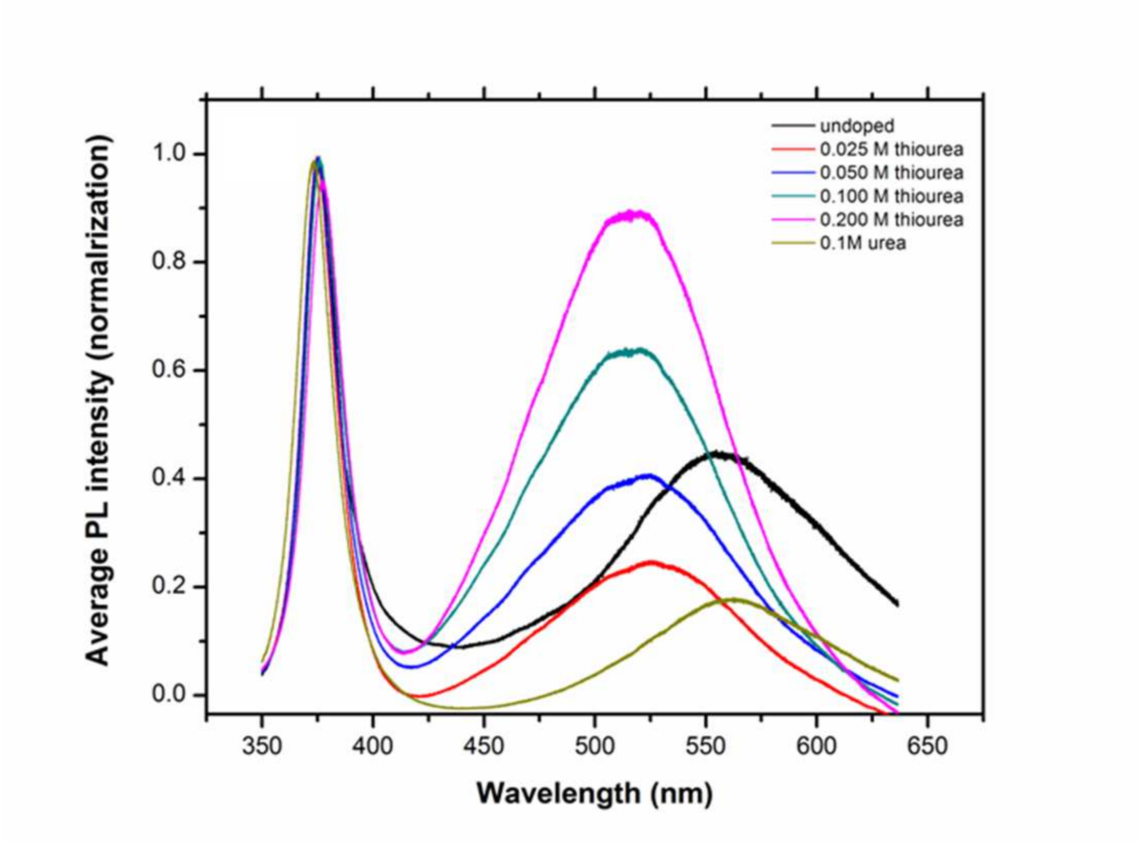

Figure 2.10: Superimposed PL spectra of samples of ZnO nanostars fabricated from a combined aqueous solution of 0.025 M zinc nitrate, 0.025 M hexamine, and various concentration of thiourea, compared with undoped and 0.1M urea reference samples.

The optical properties of the nanostars were studied with photoluminescence (PL) spectroscopy using a 325 nm He-Cd laser as a pump source at room temperature. Figure 2.10 shows the normalized PL spectra of the ZnO nanowires doped with various thiourea concentrations. Undoped nanowires feature strong UV emission at the band edge (~375 nm) and weak visible emission centered near 557 nm. As the concentration of thiourea increases, the visible emission is enhanced relative to the UV emission, and the emission peak blue-shifts to near 517 nm as expected for sulfur-doped ZnO[68]. No significant enhancement or blue-shift of visible emissions was observed in urea-doped samples.

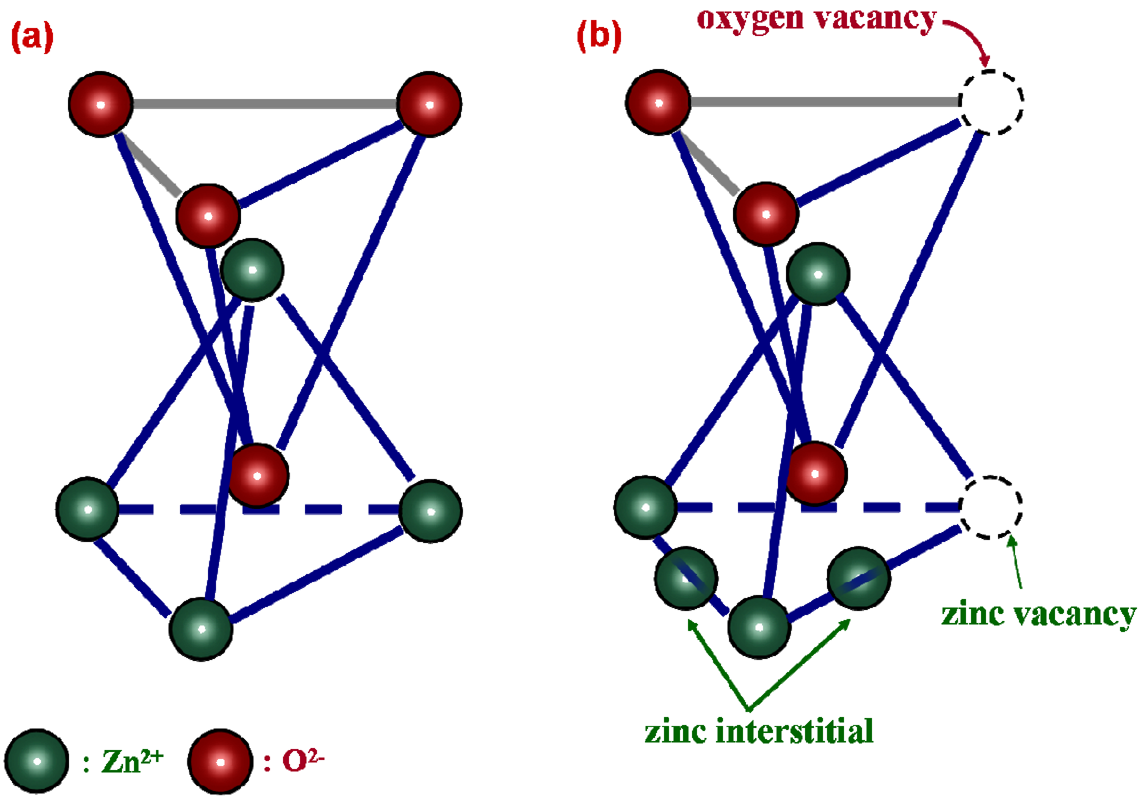

Figure 2.11: Schematics of a ZnO structure: (a) ideal ZnO structure (b) native defects causing a green emission from the ZnO structure

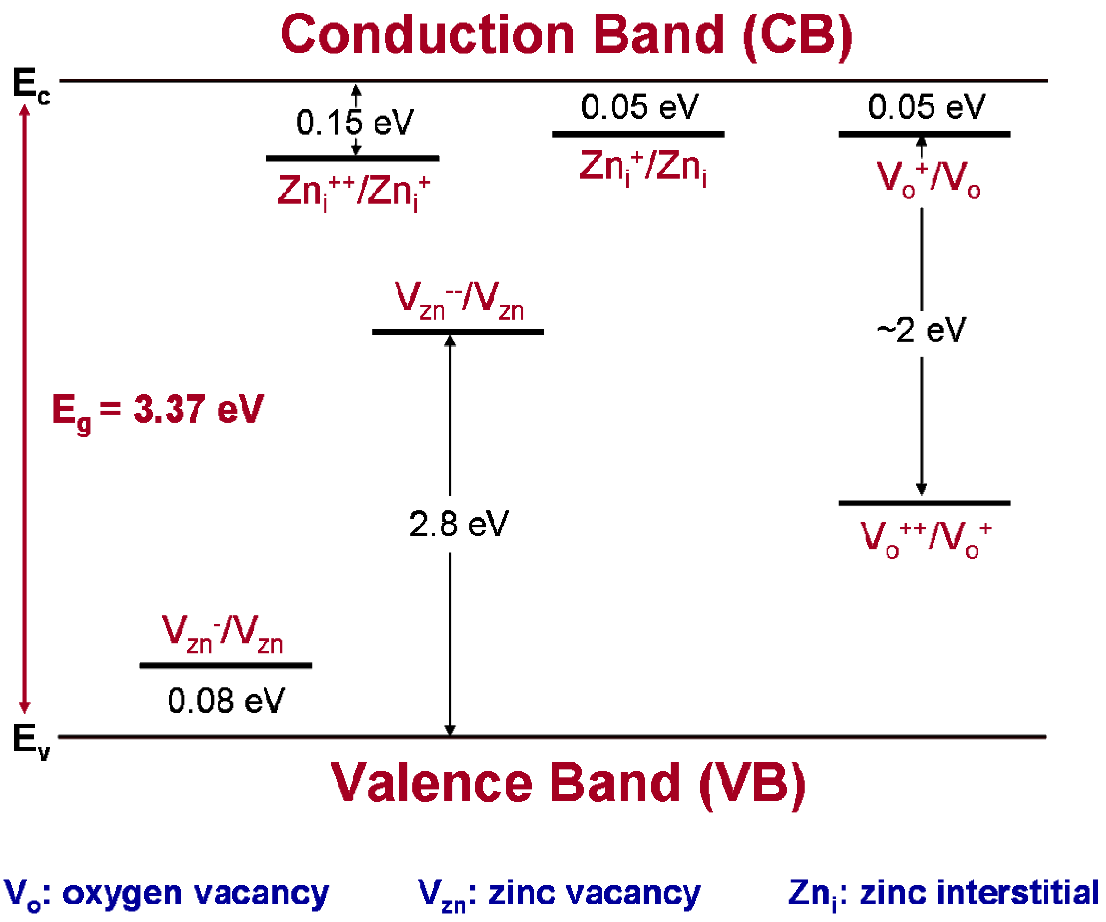

Figure 2.12[69,70]**: Schematics of intrinsic defects and impurity energy levels in the ZnO band-gap: Zn_i^+ and Zn_i^{++} are singly and doubly ionized zinc interstitials, respectively. V_o^+ is a singly ionized oxygen vacancy. V_o^{++}, V_o^+, V_o, Zn_i^{++}, Zn_i^+, Zn_i are donor defects. V_{Zn}^{--} and V_{Zn}^- are acceptor defects.**

Figure 2.11 schematics show representative crystal defects such as zinc interstitials and vacancies and oxygen vacancies in ZnO. Although the exact origin of the green emission in undoped ZnO has yet to be identified[71,72], several hypotheses have been advanced that explain the green emission as the result of such defects as (i) singly ionized oxygen vacancies[72-77]; (ii) antisite oxygen[72,78,79]; (iii) oxygen vacancy and zinc interstitials[72,80]; (iv) Cu impurity[72,81]; and (v) intrinsic defects like donor-acceptor transition[72,82], zinc vacancy[72,83,84], and surface defects[71,72]. It is noteworthy that doping with sulfur in ZnO nanostars enhances the green emission.

Figure 2.12 shows intrinsic defects and extrinsic impurity energy levels in the band-gap of ZnO[69,70]. In nano-materials that feature a small scale length and a large surface to volume ratio, intrinsic defects largely affect the material properties and functionality of applications[69]. In ZnO, although both the oxygen vacancy (V_o) and the zinc interstitial (Zn_i) are dominant defects and play roles as donors, the zinc vacancy (V_{Zn}) acts as an acceptor. Based on the energy diagram in Figure 2.12, the energy level of the sulfur impurity in the band-gap is assumed to be positioned at about 2.4 eV above the valence band according to the enhancement of the green emission.

2.6 Ab Initio Simulation Results for the Growth mechanism of Sulfur-Doped ZnO Nanostars

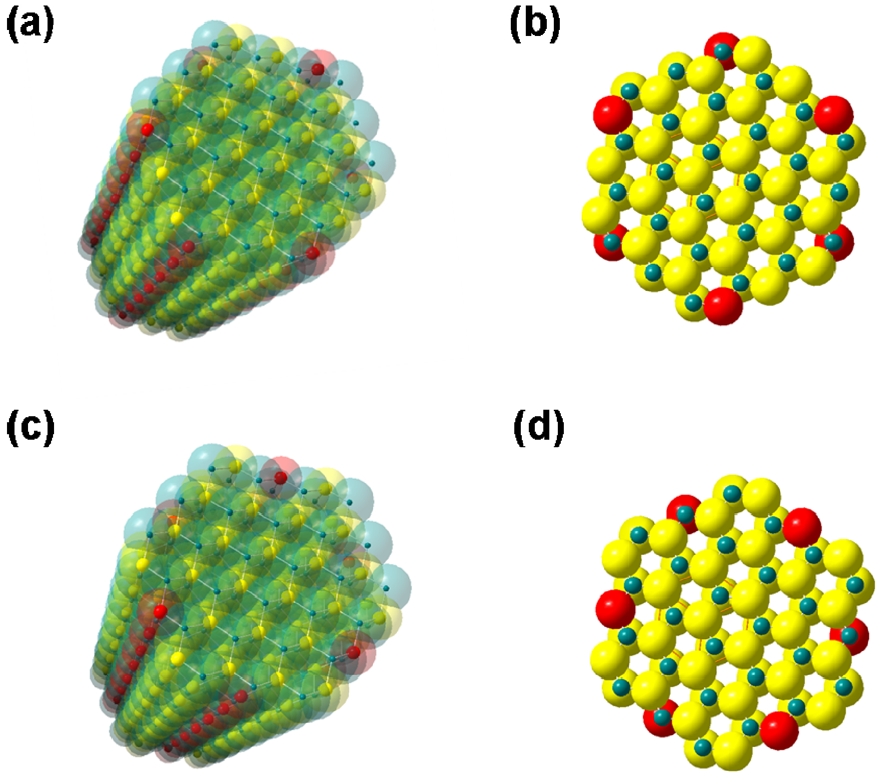

Figure 2.13: (a) and (b) show schematics of sulfur replacements at the vertices of the hexagon in ZnO, whereas (c) and (d) show schematics of sulfur replacements at the edges of the hexagon in ZnO. In the spheres shown here, sulfur is red, zinc is green, and oxygen is yellow (Courtesy of Professor Weitao Yang Group in Duke Chemistry).

Ab initio simulation was performed by Professor Weitao Yang's Group in Duke Chemistry, our collaborator. In order to understand the role of sulfur in the formation of nanostars, the energy configurations corresponding to two distinct scenarios of nanowire structure have been calculated. First, the ZnO nanowires were modeled as wurtzitic hexagonal structures (space group C6mc) with lattice parameters a = 0.3296 nm and c = 0.52065 nm. Then, in one scenario, sulfur atoms replace the oxygen atoms at the corners of the nanowire surface (Figure 2.13 (a) and (b)). In the other scenario, sulfur atoms replace the oxygen atoms at the edges of the nanowire surface (Figure 2.13 (c) and (d)). The binding energy for each scenario was calculated using the Vienna *ab initio* simulation package (VASP)[85,86], which is based on the density functional theory in the plane-wave basis and on the projector augmented wave (PAW) representation. The exchange and correlation energy was described according to the generalized gradient approximation (GGA) of Perdew *et al.*[87]. Brillouin-zone integrations are approximated by using the special 1×1×30 grid k-point sampling of the Monhkorst-Pack scheme[88] for the nanowire (z direction is chosen as the nanowire axis), in conjunction with the Gaussian-smearing method with $\sigma = 0.01$ eV. The cutoff for the plane-wave kinetic energy in this calculation was chosen as 400 eV. The convergence of the total energy with respect to *k*-point sampling (Table 2.1) and the plane-wave energy cut-off were both examined.

Table 2.1: Calculated total energy of the supercell as a function of the number of k-points used

Number of k-points	1	30	40
E_1/eV	453.884765	445.646002	445.648226
E_2/eV	453.256291	445.405713	445.407931
E_2- E_1/eV	0.628474	0.240289	0.240295

E_1: The total energy of the supercell with corner replacement by six S atoms per plane.
E_2: The total energy of the supercell with edge replacement by six S atoms per plane.

The calculation indicates that the sulfur-replacement binding energy is 0.04 eV higher per atom with corner replacement than with edge replacement. In other words, the corner replacement of oxygen by sulfur is significantly more stable, suggesting a preferred pathway for the growth of sulfur-doped nanostructures. Sulfur atoms provided by thermally decomposed thiourea prefer to bind at the stable corner sites, thereby hindering growth from the corners. Wedge-shaped growth of S-doped material from the edges leads to the observed hexagram-shaped structures. This wedge-shaped growth occurs because of differences in the Zn–S bonds between the corner and edge replacement configurations. In edge replacement, one of the three zinc ions bonded with a sulfur ion has a dangling bond, whereas in corner replacement, two of the three zinc ions have a dangling bond.

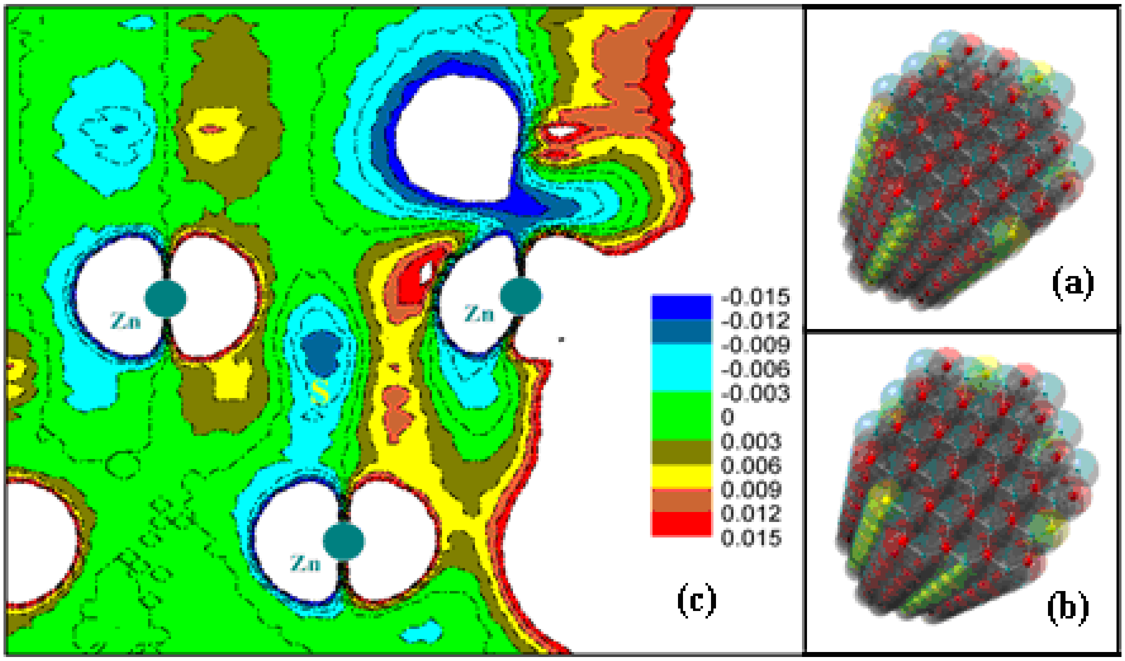

Figure 2.14: (a) O (red) is replaced by S (yellow) at the corners of the nanowire surface; (b) O (red) is replaced by S (yellow) at the edges of the nanowire surface (c) A spatial contour plot of the charge density difference (units of e/Å^3) between edge and corner replacement of S calculated in the plane of Zn atoms in the surface. The yellow letter "S" indicates the position of the S nucleus above this plane.

These different bond configurations are caused by differences in the charge density distribution that ultimately affect structural stability. This can be seen in Figure 2.14 (c), which plots the calculated charge density difference $\Delta\rho = \rho_2 - \rho_1$ in the plane of the Zn atoms in units of e/Å^3, where ρ_2 is the charge density after edge replacement, and ρ_1 is the charge density after corner replacement in plane $\{01\bar{1}\frac{8}{15}\}$, but shifted to the same replacement position to enable direct subtraction. The white areas represent regions in the plane of Zn atoms with (unplotted) large charge density variations (>0.015

e/Å^3) of little interest because they are far removed from the region of the S atom. Small but important charge density differences are revealed in Figure 2.14 near the region of the sulfur atom. Specifically, the blue region in the plane beneath the position of the sulfur nucleus, where $\Delta\rho \approx -0.01$ e/Å^3, shows that electrons concentrate more tightly near the sulfur ion in the corner replacement geometry. This confirms the stronger bond strength that makes corner replacement more stable.

2.7 Summary

We developed a simple hydrothermal growth process for sulfur doped ZnO nanowires. As the degree of doping with sulfur increase, the hexagonal nanowires develop into nanostars with hexagram cross sections. The role of sulfur in the transformation of the cross-sectional morphology was verified by various experiments and calculations. Through *ab initio* simulation, we revealed that sulfur atoms placed at the vertices in a hexagon lead to wedge-shaped growth of the S-doped material from the edges in hexagons. Sulfur-doped nanostar structures feature enhanced, slightly blue-shifted visible light emission, which might be of interest in applications for devices that emit visible light.

3. Novel Synthetic Methodology for Controlling the Orientation of ZnO Nanowires Grown on Amorphous Silicon Oxide Substrates

Although early 2000 brought progress in the alignment of ZnO nanowires, this technology has not yet reached the point where aligned nanowires can be grown on silicon in cost-effective, large-scale quantities. Both conditions must be met for commercialization of nanoscaled devices. In addition, successful aligned growth of nanowire arrays on silicon is expected to influence the feasibility of device design and fabrication in nanowire LEDs and any subsequent increase in lighting efficiency.

This chapter encompasses my research into achieving well-aligned ZnO growth and also the efforts of others to meet this challenge. The discussion is organized as follows: first, ZnO nanowire growth based on the vapor-liquid-solid (VLS) process of the chemical-vapor-deposition (CVD) system; second, gold (Au) seed effects for ZnO nanostructures in the VLS process; and, third, ZnO nanocrystalline seeds made using novel synthetic methods for vertically aligned ZnO nanowires.

3.1 The VLS Process in the CVD System

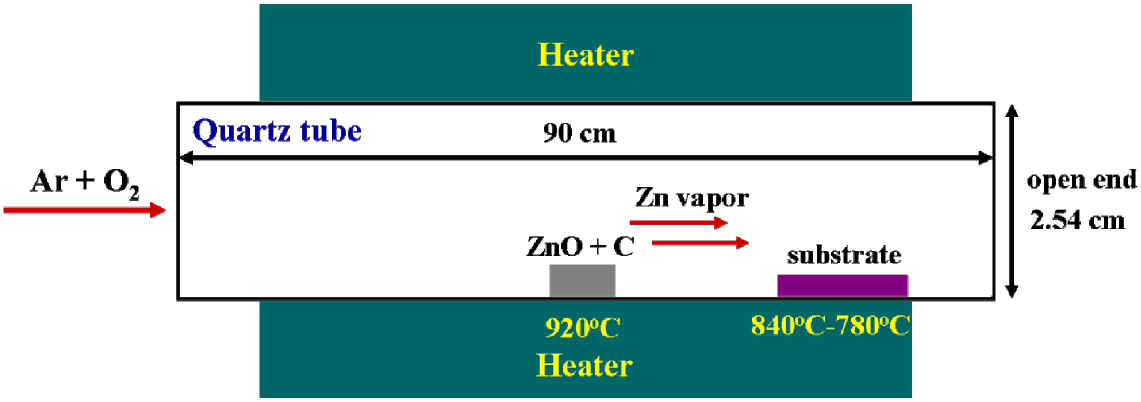

Figure 3.1[89]: Schematic of the chemical vapor deposition (CVD) system

Crystallization is a key feature in the growth of 1-D nanowire and is mainly composed of nucleation and growth[1]. As the concentration of vapor- or solution-phase reactants, such as ions or atoms, exceeds a critical point, nucleation occurs in a concentrated spot and acts as a seed[1]. If an adequate supply of these fundamental reactants is continued during this nucleation process, a nanowire will begin to grow from this nucleus. In this process, the vapor phase reactants can originate from molecular beam epitaxy (MBE) or pulsed laser ablation (PLA) or from the decomposition of precursors in the chemical vapor deposition[90]. Of these techniques, CVD is the most accepted because of its simplicity and accessibility. Figure 3.1 schematically illustrates the CVD system. In the CVD system, source materials on the alumina boat and substrates are loaded, respectively, into the highest temperature zone and downstream from the source in the quartz tube. Reactant gases such as argon (Ar) and oxygen (O_2) introduced at high temperatures convey source vapors to the substrate, where a chemical reaction is generated.

The CVD system has two mechanisms for growing nanowires. One is the vapor-liquid–solid (VLS) process; the other is the vapor-solid (VS) process. A metal catalyst is used in the VLS system, but not in the VS process. In the VLS process, the substrate is coated with 20-100Å of thin gold (Au) film or nanoparticles, both of which in this approach play an essential role as seeds.

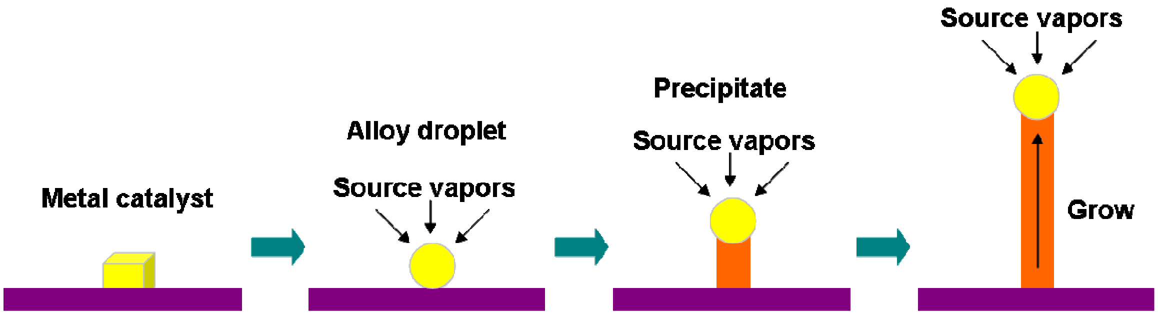

Figure 3.2[2]: Schematic of the vapor-liquid-solid (VLS) process

Figure 3.2[2] illustrates the sequences of the VLS process. Above the eutectic temperature, this Au film is molten and transformed into droplets[90]. A continuous supply of vapor reactants supersaturates these Au droplets, which become alloy droplets[90]. Nanowire growth occurs in the interface between the alloy droplets and the substrate.

The CVD-VLS process has numerous advantages. Unlike the VS process that does not exploit a metal catalyst, the VLS process allows preferred-site growth. This process also allows control of the wire diameter. In addition, an Au seed serves to guide wire growth and usually determines the diameter of the nanowire. Consequently, a nanowire grown by the VLS process usually can be identified by an Au particle at its tip[33]. Tip diameter is comparable to the connected nanowire[33].

In the VLS process, 800-900° C is generally accepted as a moderate temperature range for growing well-aligned ZnO nanowire arrays[91]. This temperature is reached by using a source material created by grinding ZnO powder and graphite (C) together, a process known as the gold-catalyzed carbon-thermal reduction method[92]. This method is based on the disassociation of both solid phase ZnO and C at temperatures above 800°C. This disassociation generates both vapor phase zinc (Zn) and carbon dioxide (CO). The zinc vapors thus generated, along with oxygen vapors that are supplied from the outside, are conveyed to the Au liquid droplets and ultimately form ZnO nanowires. Since the advent of this carbon-thermal method, the chemical reaction temperature used in CVD has been lowered to 900° C from 1300° C[93].

3.2 Au Catalysts Generating Various ZnO Nanostructures on Silicon Substrates in CVD-VLS Process

3.2.1 Formation of Various ZnO Nanostructures Based on Temperature Gradient

The synthesis of ZnO nanostructures involves critical factors such as temperature, vapor flux, and types of substrate. Of these, temperature is the most sensitive and crucial component. Because heat losses are inevitable in a furnace, it is difficult to sustain a consistent input temperature throughout all sections of the tube. As vapors are fed through the tube in the furnace, their velocity, partial pressure, viscosity, and density vary because of temperature changes during transit. Consequently, these varied “local” growth environments result in the creation on substrates of various morphologies of ZnO nanostructures.

My experiments used oxidized Si substrates coated with 2-nm-thick Au films. Vapors were fed into the tube from left to right at a rate of 49 standard cubic centimeters per minute (sccm), along with 2% oxygen at 1 sccm. Input temperatures in the furnace varied from 850^{o}C to 990^{o}C, with the changes occurring in increments of 10^{o}C.

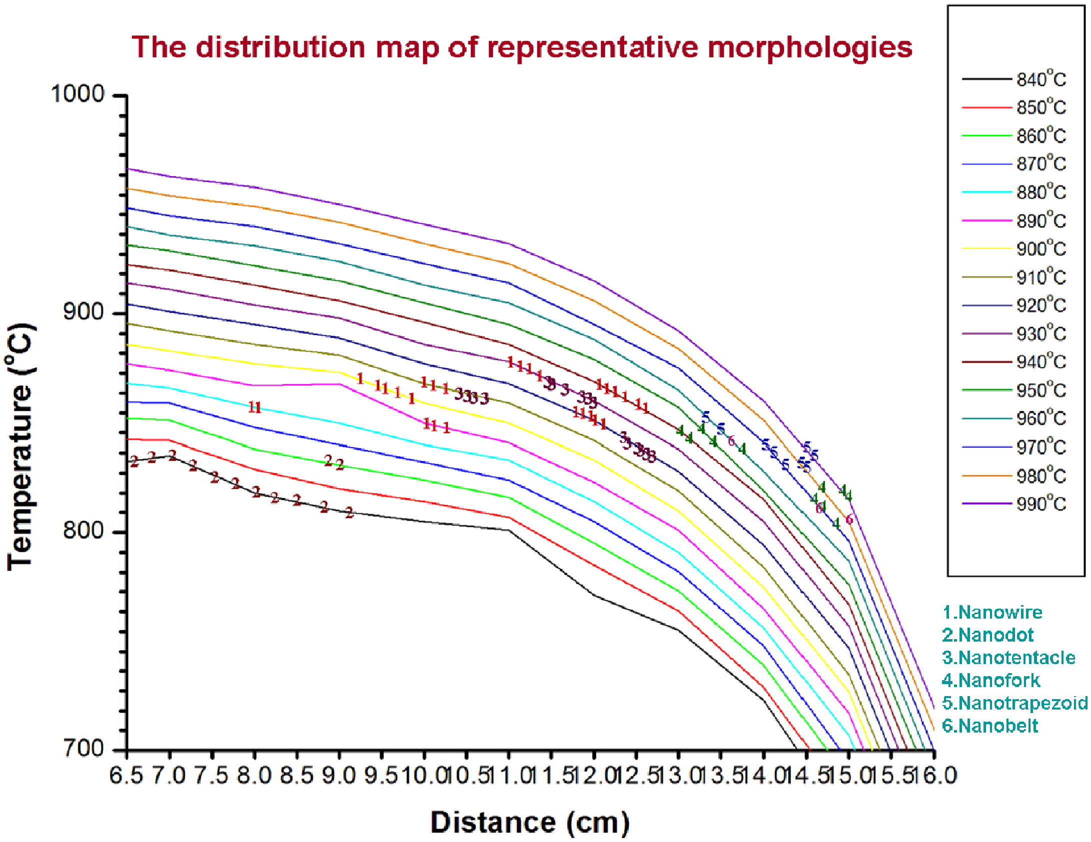

Figure 3.3: This graph maps the distribution of representative morphologies. Dots, spaced 1mm apart, were marked using a pen in each as-grown sample to take sequential SEM images. Each color line indicates a different input temperature in the furnace. Each number marks a different nanostructure and the position at which it was found.

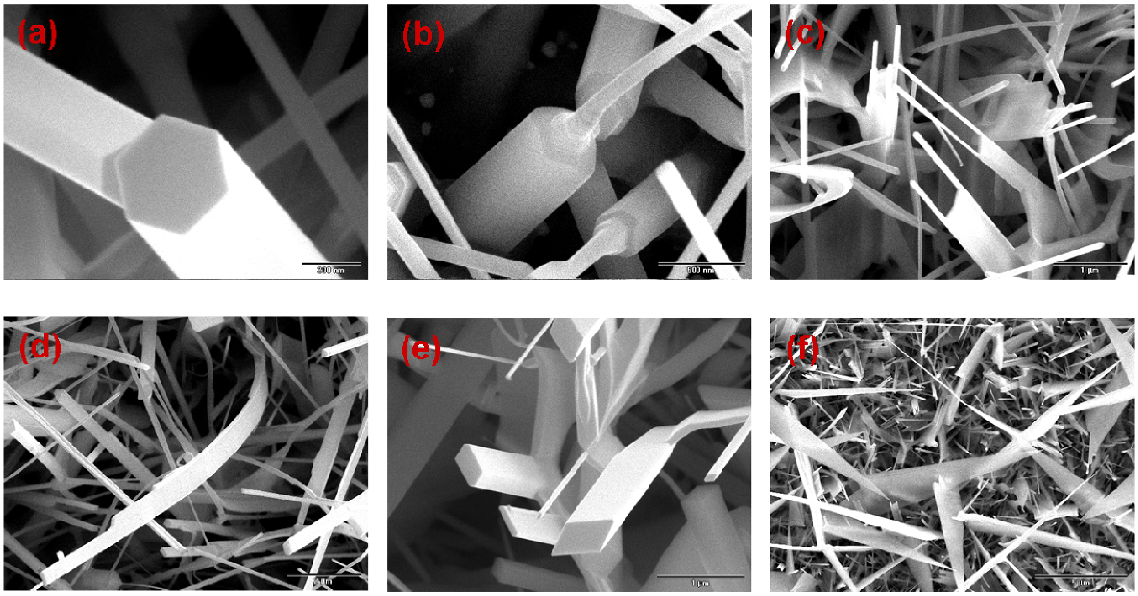

Figure 3.4: SEM images of representative ZnO nanostructures according to their reflection of local temperatures: (a) nanowire, (b) nanotentacle (or nanofeeler), (c) nanofork, (d) nanobelt, (e) nanotrapezoid, and (f) nanoblade.

Figure 3.3 shows the distribution of representative morphologies as determined by local temperatures in as-grown substrates. This map shows that variations in local temperature from the center of tube shaped the formation of various ZnO nanostructures. The six types of nanostructure morphologies displayed in Figure 3.4 are defined as follows: (a) a nanowire has a filled inner core and a top surface with hexagonal geometry; (b) a nanotentacle (or nanofeeler) has a second thin wire shape growing from its hexagonal top surface; (c) a nanofork has two or more tips grown on the edge of a belt-like structure; (d) a nanobelt has a parallelpiped morphology and side surfaces; (e) a nanotrapezoid has a trapezoidal top surface with side surfaces; and (f) a nanoblade has thin, sharp triangular sheet surfaces.

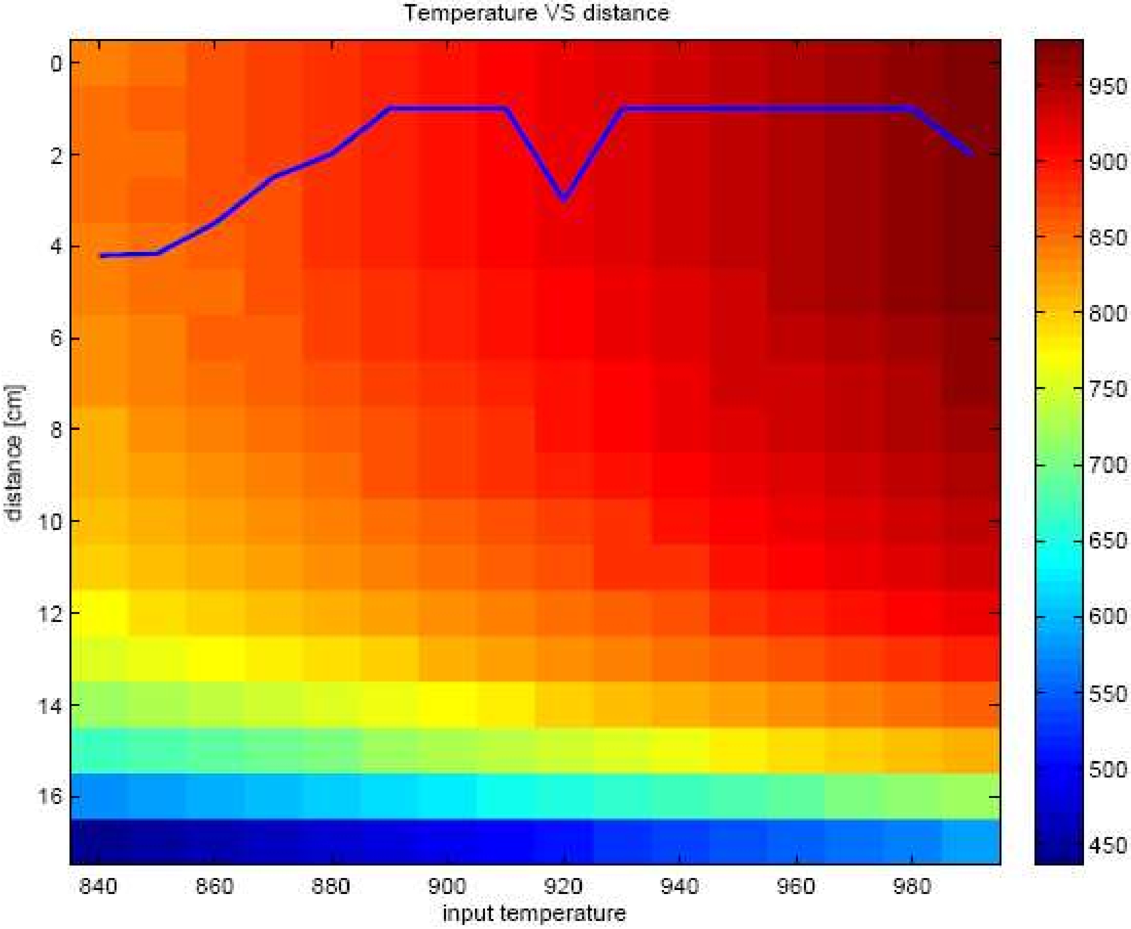

Figure 3.5: A map of local temperature distribution in a quartz tube. Dark red represents the highest temperature in the quartz tube and dark blue the lowest. The x-axis is the input temperature of the furnace ranging from 840°C to 990°C. The y-axis is the distance from the middle of the furnace (the highest temperature zone) to its end. Local tube temperatures diminish gradually with distance from the middle of the tube. The blue line on the map approximates the location that matches input temperatures.

Figure 3.5 shows the local temperature distribution in the quartz tube of the furnace. The temperatures at various locations within the tube were calibrated during a controlled experiment by inserting a thermocouple into the quartz tube during input temperatures ranging from 840°C to 990°C. Dark red represents the highest temperature of 979°C; dark blue shows the lowest temperature, 436°C. As can be seen, the temperatures within the tube gradually decline with distance from the middle of the tube.

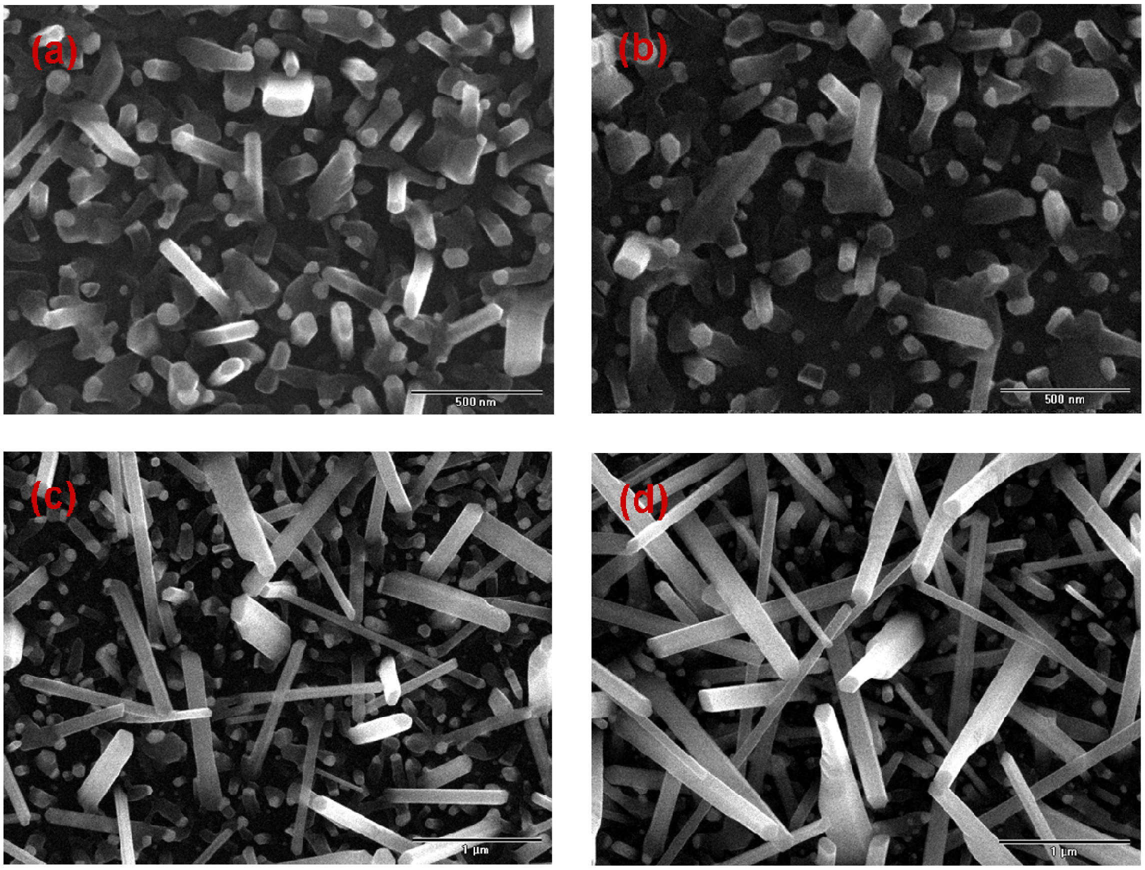

Figure 3.6: SEM images of generated wire-like morphology grown at (a) 850°C, (b) 860°C, (c) 870°C, and (d) 880°C. In these experiments, Ar and O_2 were fixed at a flow rate of 49 sccm and 1 sccm, respectively.

As shown in Figure 3.6, small yield and poor quality nanowires were generated in (a), (b), and (c); all were generated at input temperatures lower than 880^{o}C. Thus, 880^{o}C is a minimum input temperature for moderate nanowire growth. Although a wire-like morphology was identifiable at input temperatures ranging from 880^{o}C to 940^{o}C, local temperatures in the tube determined the quality and density of the nanowires.

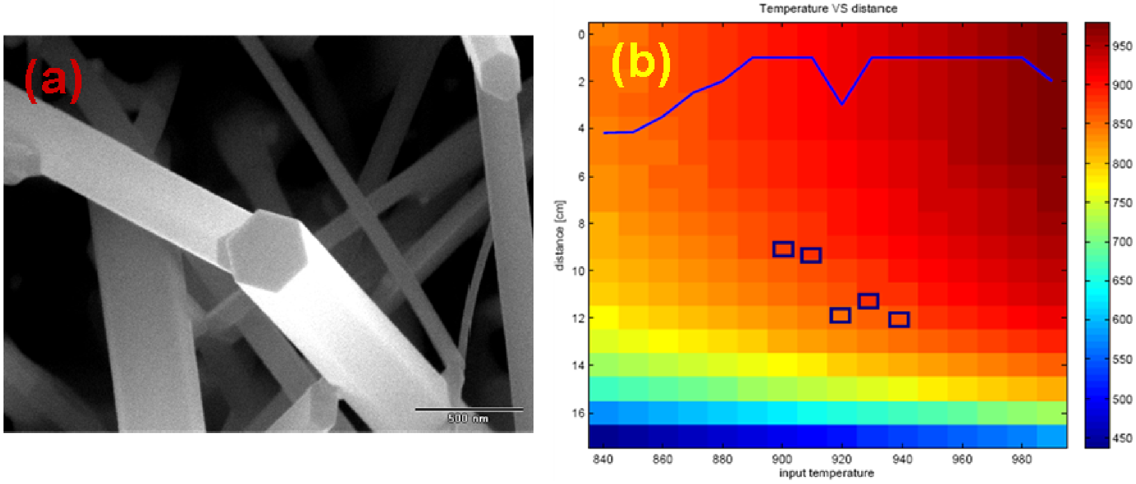

Figure 3.7: (a) A SEM image of a high quality nanowire at a furnace input of 930^{o}C; (b) a distribution map of a wire-like morphology. Nanowires of varying quality and yields were discovered in the sections marked by the blue boxes.

In Figure 3.7, (a) is a SEM image of high quality nanowire produced at a furnace input temperature of 930^{o}C; (b) shows the sections in which all wire-like nanostructures were found without regard to their quality and yield. High quality nanowires were mainly discovered at furnace input temperatures ranging from 930^{o}C to 940^{o}C, whereas relatively low quality nanowires were discovered at temperatures ranging from 890^{o}C to

920°C. The moderate local temperatures for the growth of wire-like morphology were at temperatures ranging from 850°C to 880°C. A range from 860°C to 870°C was the most suitable for growth of nanowires with the highest quality and yield and excellent hexagonal top surfaces. Wire-like morphology, accompanied by traces of other nanostructures, was found laterally in an area of 1-2 mm within a 3-4 cm textured nanostructure area. This result implies that nanowire is sensitive to local temperatures and that the successful growth of nanowire structures occurs within a narrow range of temperatures that also serve to localize the region in which this growth occurs.

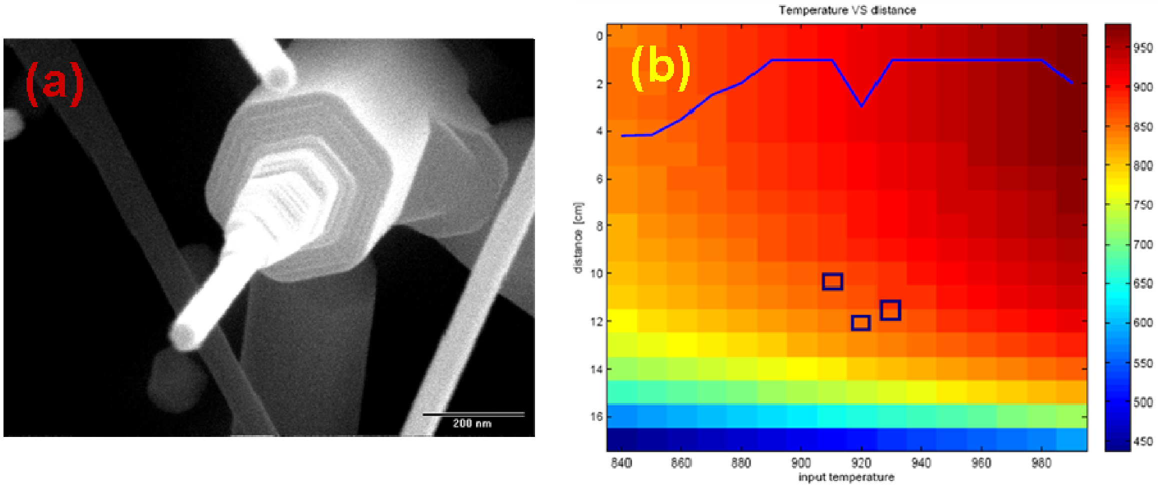

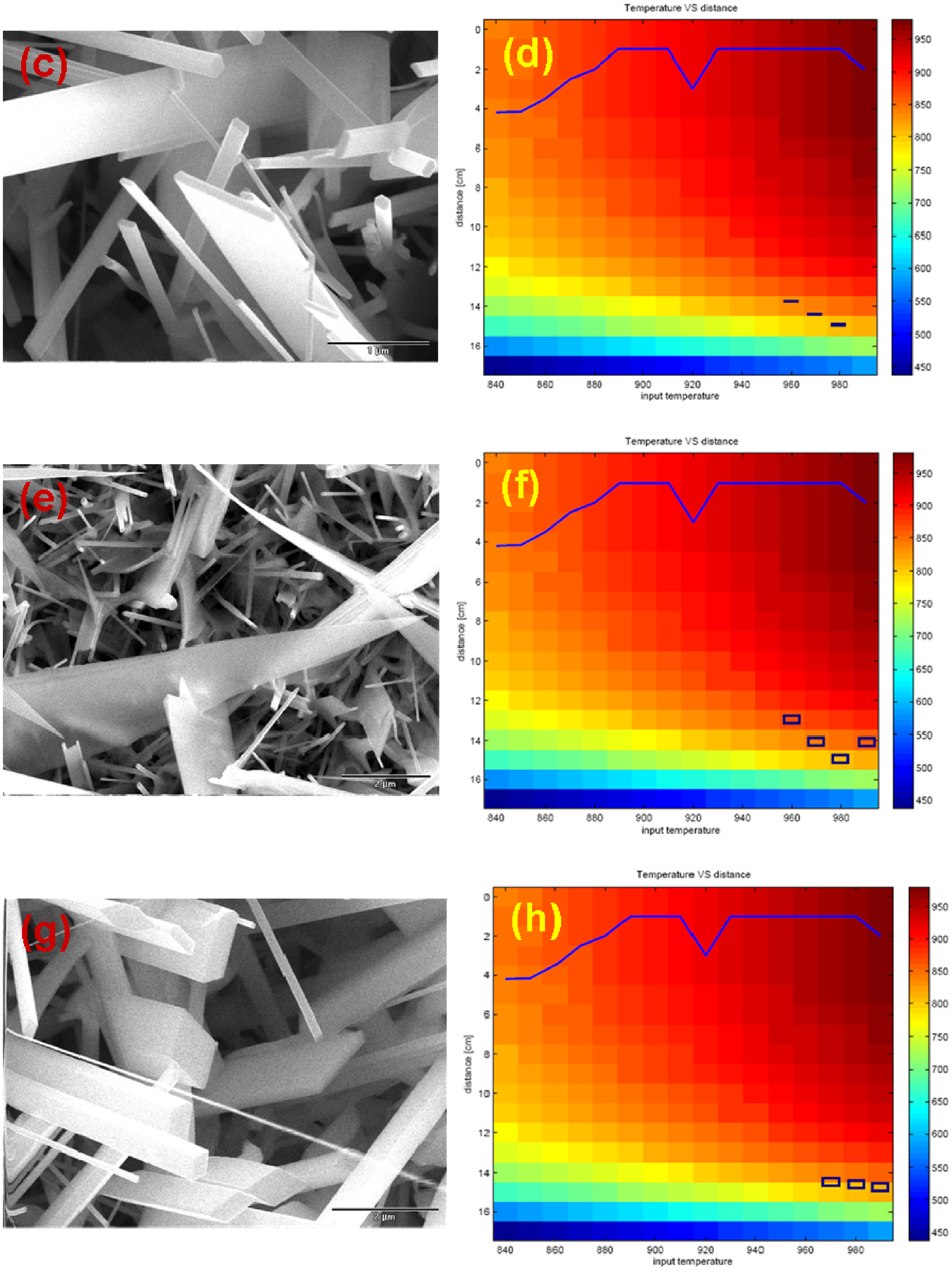
(c)
1 µm
Temperature VS distance
(d)
distance [cm]
0
2
4
6
8
10
12
14
16
840
860
880
900
920
940
960
980
input temperature
950
900
850
800
750
700
650
600
550
500
450
(e)
2 µm
Temperature VS distance
(f)
distance [cm]
input temperature
(g)
2 µm
Temperature VS distance
(h)
distance [cm]
input temperature

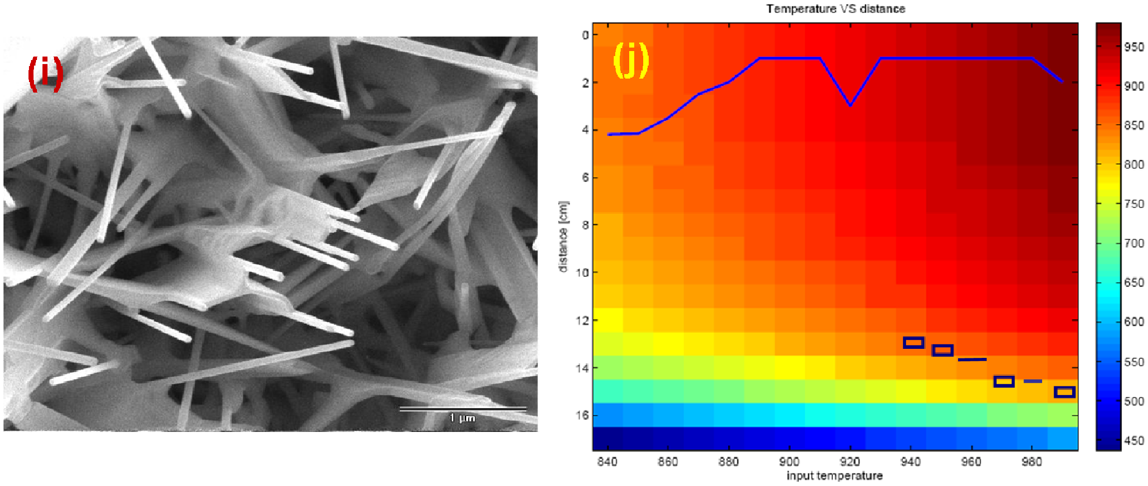

Figure 3.8: SEM images of various ZnO nanostructures and their occurrence on a local temperature distribution map: (a) a nanotentacle, (b) blue boxes indicate the range of local temperatures in which nanotentacles were discovered; (c) a nanobelt, (d) blue boxes indicate the range of local temperatures in which nanobelts were discovered; (e) a nanoblade, (f) blue boxes indicate the range of local temperatures in which nanoblades were discovered; (g) a nanotrapezoid, (h) blue boxes indicate the range of local temperatures in which nanotrapezoids were discovered; and (i) a nanoforks, (j) blue boxes indicate the range of local temperatures in which nanotrapezoids were discovered

The most interesting phenomenon was that various nanostructures were always accompanied by traces of nanowires on a substrate. Figure 3.8 displays various ZnO nanostructures and locates them on a local temperature distribution map. As shown in 3.8 (a) and (b), nanotentacles were broadly detected at temperatures ranging from 835°C to 870°C when furnace input temperatures were set at 910-930°C. Nanotentacles occurred in a row immediately behind nanowires. As shown in 3.8 (c) and (d), a few nanobelts were discovered together with nanotrapezoids at about 806°C, 811°C, and 840°C when input temperatures were at 960°C, 970°C, and 980°C, respectively.

Nanotrapezoids, which have a trapezoidal top surface, can be considered the result of the deformation of hexagonal nanowires by high thermal energy; this conclusion is because they were discovered at high input temperatures ranging from 960°C to 990°C. Nanoforks were found widely at input temperatures of 940-990°C. As furnace input temperatures increased, the local temperatures at which the formation of nanoforks was detected tended to decrease from 845°C to 825°C. Table 3.1 presents more detailed correlations between input and local furnace temperatures in the formation of various ZnO nanostructures.

Table 3.1: Correlations between input and local furnace temperatures in the formation of various ZnO nanostructures.

	Input temperature (^{o}C)	**Local temperature (^{o}C)**
Nanotentacles	910	850-860
	920	836-845
	930	860-870
Nanoforks	940	840-845
	950	840-845
	960	840
	970	830-840
	980	825-830
	990	836-840
Nanotrapezoid	960	845-854
	970-990	830-840
Nanobelts	960	840
	970	811
	980	806

The minimum radius of a nanowire is determined by the following Wagner formula[13]:

$$R_{\min} = \frac{2V_1}{kT \ln s} \sigma_{lv}$$

where $R_{\min}$ is the minimum whisker radius, V_1 is the molar volume of a metal droplet, σ_{lv} is the liquid-vapor surface energy, s is the vapor phase supersaturation, k is the Boltzmann constant, and T is the temperature in Kelvin. When Au nanoparticles sized 2-50 nm and synthesized by solutions are used as seeds, they are dispersed on a substrate by the spin-casting method. At high temperatures, scattered nanoparticles are formed as liquid droplets while retaining their gap consistency. Consequently, there is no limitation on growing small nanowires with a diameter of 2-3 nm. In contrast, thin Au film inhibits the formation of small diameter nanowires. At high temperatures above 900^{o}C, the thin Au film is molten so as to form a cluster of a few hundred liquid droplets. At this moment, the minimum radius of an Au liquid has a thermodynamic limitation imposed by the operation of the Wagner formula. For this reason, the diameters of the nanowires in my experiments were relatively large, 300-600 nm.

In theory, two different mechanisms likely account for the generation of various morphologies. Under quasi-equilibrium conditions of low temperature and a low supersaturation ratio (the ratio between actual and equilibrium pressure), the preference dictated by thermodynamics is to grow along the c-direction to minimize area and total free energy[94]. Thus, quasi-equilibrium conditions generate a wire-like morphology. Conversely, under nonequilibrium conditions of high temperature and a high supersaturation ratio, kinetics and native defects lead to the generation of sheet-like morphologies[94]. Under nonequilibrium conditions, a lot of defects, such as oxygen vacancies and zinc interstitials, are created in ZnO nanostructures. These defects lower the surface polarity of the (001) surface, thereby reducing the preferential adsorption of vapor ZnO in a Zn-terminated polar (001) surface[94]. Although growth in the c-direction is reduced, other growth directions, particularly those perpendicular to the c-direction, are improved[94]. Thus, directions normal to the (110) plane and the ($\bar{1}$20) plane lead to the creation of sheet-like morphologies.

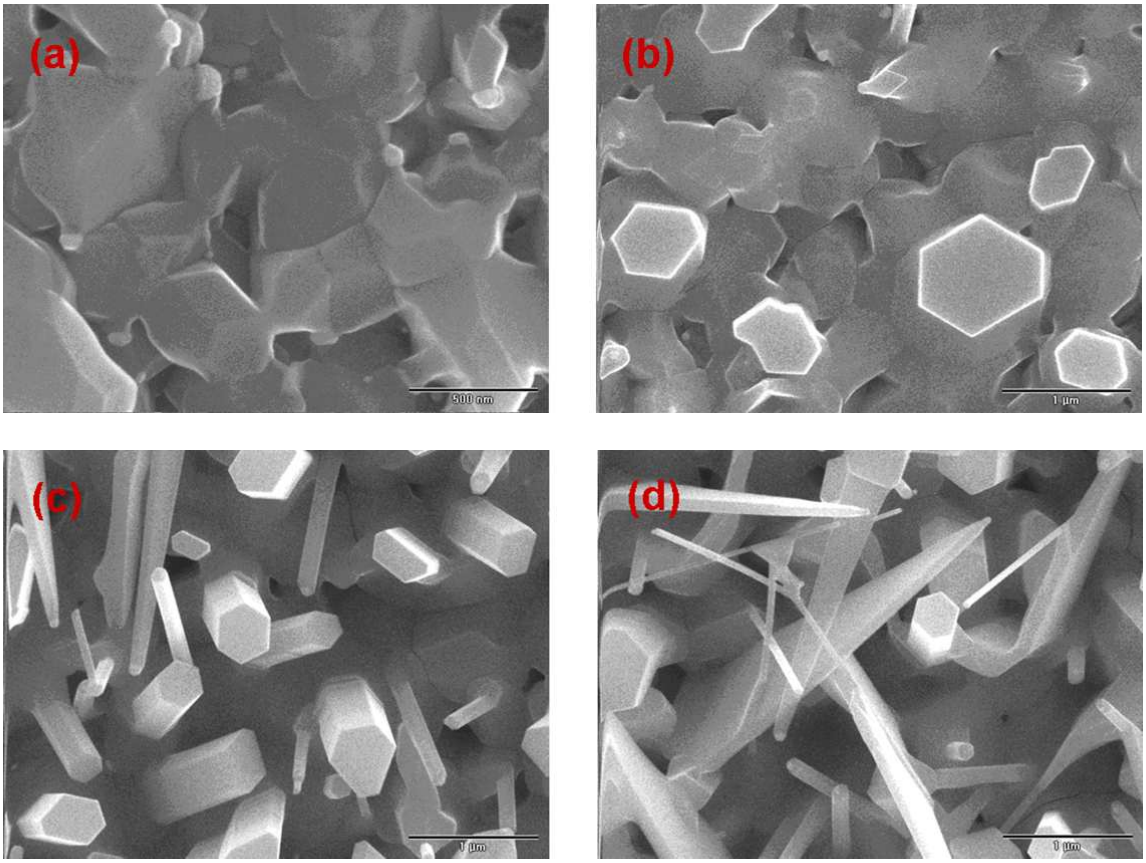

Figure 3.9: Illustrations of as-grown samples (a), (b), (c), and (d) sequentially show variations in surface morphology according to their formation at different locations. These images confirm that ZnO nanostructures originate from amorphous ZnO layers. The gap between locations was 0.5-1 mm. Growth conditions were 1 sccm O_2 with 49 sccm Ar at a furnace input temperature of 970°C.

Unlike previous studies[90,95], a significant aspect of my experiment is the lack of a role by Au liquid droplets in guiding the growth of the nanowire. As shown in Figure 3.9, the Zn vapors that were supplied were adsorbed in molten Au liquid droplets and then formed amorphous ZnO layers. It is noteworthy that the surface of this amorphous ZnO layer could not consist of c-planes but instead was made up of the diverse planes common to a ZnO wurtzite structure. In these structures, directions perpendicular to the c-plane (001), a-plane (110), or r-plane (012) are their anisotropic fast growth directions. Under these surface conditions, when ZnO nanowires are grown from the amorphous ZnO layer, interference is inevitably generated between the fast and slow growth facets. This interference then results in elastic deformation energy on their surfaces. The local temperature of a substrate determines the degree of interference and elastic deformation energy. Thus, because of varying temperatures in the furnace, various morphologies of ZnO are generated.

3.2.2 Gas Flux Feeding Effect for the Formation of ZnO Nanostructures

Optimized growth conditions may be the most important step toward growth arrays of well-aligned ZnO nanowires for a study. In the CVD-VLS process, ZnO nanostructures are sensitive to such growth parameters as variances in local temperatures, flux ratio, and the partial pressure of gases fed into the tube. To synthesize ZnO nanostructures, equal amounts of ZnO powder (~0.6g) and C (~0.6g) were ground up and placed at the center of a quartz tube (90 cm long with a 1-inch inner diameter). A silicon substrate coated with about a 2 nm thickness of Au was placed downstream from the precursor materials. This quartz tube was inserted into a horizontal tube furnace that was heated to 850-1000^{o}C. Argon (Ar) and oxygen (O_2) were supplied to the tube as feeding gases. The Ar flow rate was varied from 50 sccm to 200 sccm. The effects of an O_2 flow rate varying from 0 to 12 sccm also were explored.

In the carbon-thermal evaporation method, Zn vapor originates as a source at a temperature of 900°C as a result of the following reaction[93]:

$$(1)\ ZnO_{(s)} + C_{(s)} \rightarrow Zn_{(v)} + CO_{(v)}$$

Additionally, O_2 may be involved through three possible routes[2]:

$$(2)\ 2C_{(s)} + O_{2(v)} \rightarrow 2CO_{(v)}$$

$$(3)\ 2CO_{(v)} + O_{2(v)} \rightarrow 2CO_{2(v)}$$

$$(4)\ 2Zn_{(v)} + O_{2(v)} \rightarrow 2ZnO_{(s)}$$

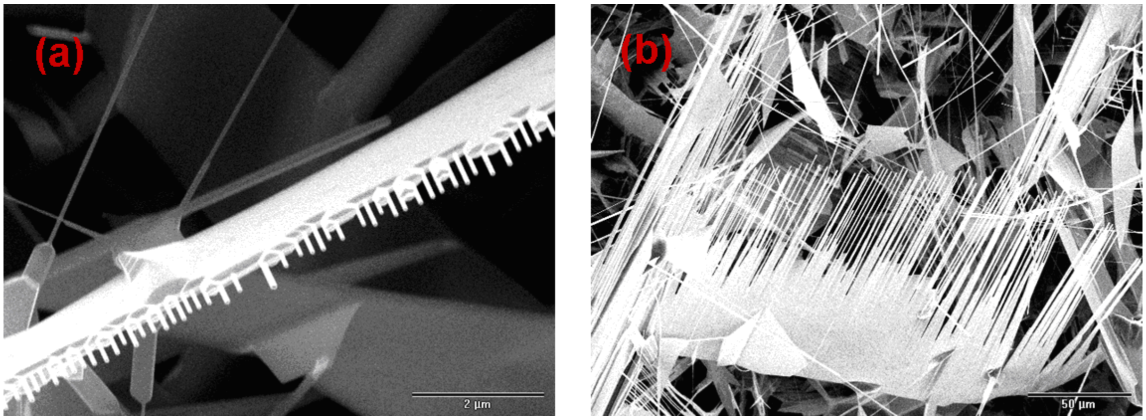

Figure 3.10: SEM images of ZnO nanostructures: The growth conditions for (a) and (b) were both Ar 50 sccm and 100 sccm at 1000°C.

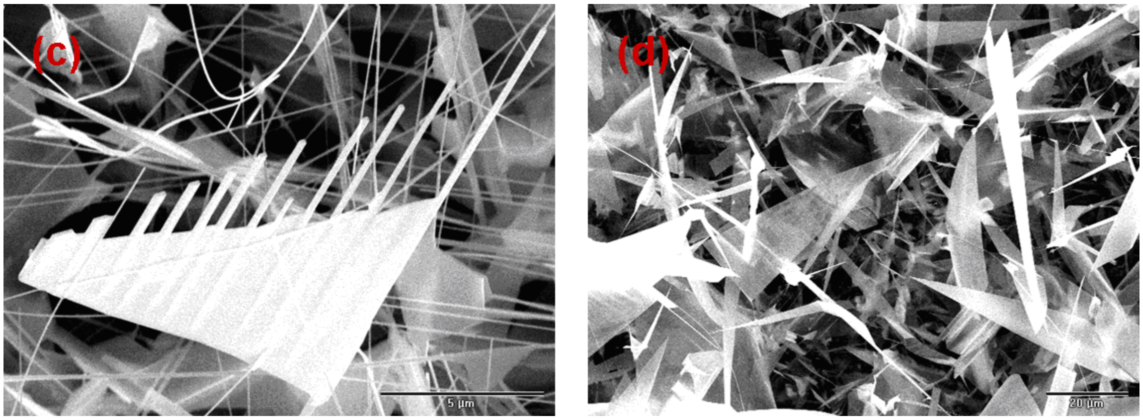

Figure 3.10: SEM images of ZnO nanostructures: The growth conditions for (c) and (d) were both Ar 50 sccm and 150 sccm at 950°C.

Figure 3.10 displays as-grown nanostructures without any supply of O_2 flux. Although no O_2 was supplied from outside the tube, the presence of less than 0.1% O_2 — either because it was residual in the tube or leaked in from outside — contributed to chemical reactions. Increases in Ar flux in 50 sccm increments from 50 sccm to 150 sccm created comb-like (Figure 3.10, a and c), saw-like (Figure 3.10, b), and blade-like (Figure 3.10, d) nanostructures in each sample without regard to temperature.

According to the previously mentioned stoichiometry, if the partial pressure of O_2 is too low, most of the O_2 is consumed simply to generate CO (2). In an equilibrium status, the increased CO partial pressure decreases the Zn partial pressure (1). As a result, too few Zn vapors exist to grow the nanowire. However, unlike the expected reactions previously mentioned, enriched Zn growth conditions are nevertheless built up on the substrate because increasing the Ar flux conveys more Zn vapor ions to the substrate.

The morphology that occurs under these conditions is determined both by kinetics (the growth environment) and surface energy[96]. The nanocomb and nanosaw structures are the result of the surface polarity of ZnO. According to a previous report[96], a Zn-terminated (001) polar surface is chemically active, whereas an O-terminated ($00\bar{1}$) polar surface is inactive. In the case of nanocombs and nanosaws, the backbone of the structure (the comb ribbon) grows in the fast-growth direction, which is [$2\bar{1}0$] or [010]. At the same time, slow growth occurs along the Zn-terminated [001] direction and then forms the "teeth" or "tip" structure. In these structures, Zn clusters on the (001) plane of nanocombs could induce second growth on one edge of the comb ribbon similar to what occurs in the VLS process[96]. Therefore, the polarity of the ZnO (001) surface affects the formation of the nanostructures.

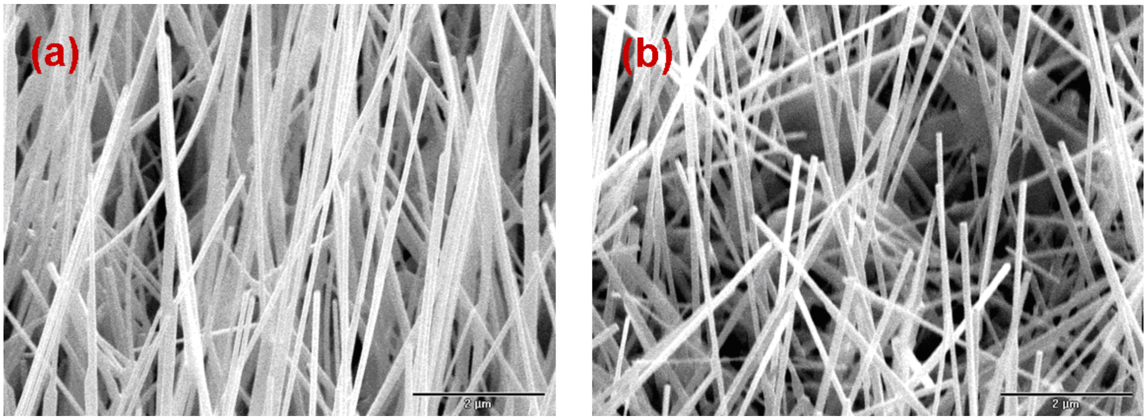

Figure 3.11: SEM images of ZnO nanowires from a 52° angle. The growth condition of (a) was 49 sccm Ar at 920°C; the growth condition of (b) was 49 sccm Ar with 1 sccm O_2 at 920°C.

Figure 3.11 (a) and (b), respectively, show SEM images of as-grown ZnO nanowires without O_2 and with 2% O_2 supplied at a rate of 1 sccm at a temperature of 920°C. The Ar flow rate was fixed at 49 sccm (98%) in both cases. As mentioned before, although no O_2 was supplied, a small amount of O_2 leaking into the tube was involved in the chemical reactions in 3.11 (a). The diameters of the nanowires generally range from 100 nm to 200 nm, with lengths up to 10 µm. As the O_2 partial pressure is gradually increased, O_2 reacts with CO and then forms CO_2 (3). In the course of this reaction, the CO partial pressure is lowered. As a result, because the CO partial pressure is reduced in the equilibrium status of the reaction (1), a moderate increase in zinc vapors occurs. These zinc vapors are supplied to the Au seeds and lead to the growth of nanowires.

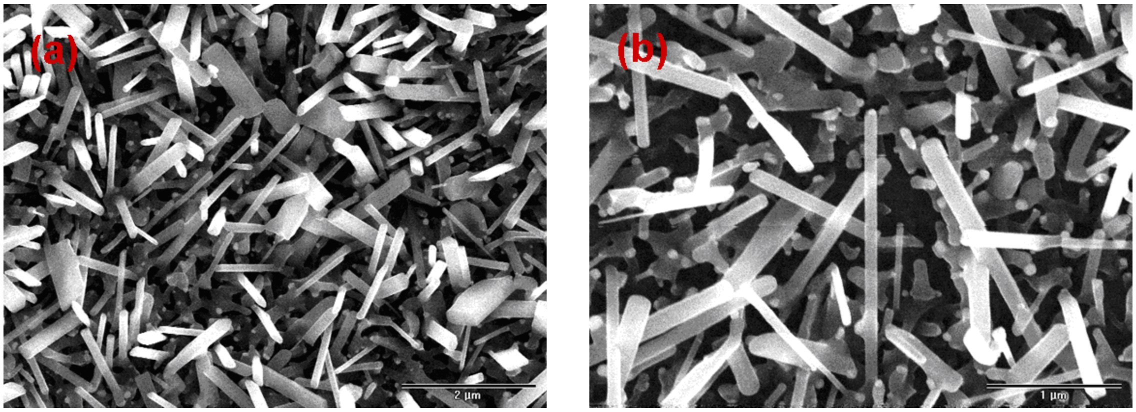

Figure 3.12: SEM images of ZnO nanorods. The growth conditions for (a) consisted of O_2 at 4 sccm with 49 sccm Ar at 920°C; growth conditions for (b) were O_2 at 12 sccm with 49 sccm Ar at 920°C.

Figure 3.12 (a) and (b) show SEM images of as-grown ZnO nanowires grown in an environment of 4 (7.5%) sccm and 12 (19.7%) sccm O_2 at a fixed Ar flow rate of 49 sccm at 920°C. As the images demonstrate, the yields and dimensions of the ZnO structure degrade under conditions of increased O_2. If the O_2 partial pressure is too high, the surplus O_2 reacts directly with the zinc vapor. In this case, therefore, ZnO film or grain can be formed, depending on the reaction (4).

In summary, experiments conducted with a controlled gas flux indicate the formation of nanostructures is sensitive to the partial pressure of O_2 that occurs in the growth environment. According to the experiments conducted for this thesis, 1 sccm (2%) O_2 flux with 49 sccm Ar (98%) is a moderate O_2 partial pressure for growing nanowires. As shown in Section 3.2.1, various nanostructures were created as local temperatures waned in the tube. However, the formative mechanism for these nanostructures remains poorly understood. Nevertheless, this phenomenon can be accounted for through correlation of the local temperatures and the corresponding fluid dynamics that occur in the tube. As the supplied reactant vapors flow through the tube, the density and velocity of the flowing gases are affected by different local temperatures. Consequently, the next study will investigate fluid dynamics in the tube. Computational modeling of gas distribution in the tube is expected to provide a clear understanding of the growth mechanism behind various nanostructures.

3.3 ZnO Nanocrystal Seeds Generating Vertically Aligned ZnO Nanowires on Silicon Oxide Substrate in the CVD-VLS Process

The oriented growth of ZnO nanowires has been realized by Au-catalyzed hetero-epitaxy on single crystalline substrates such as sapphire or nitride[97]. However, because of both the large lattice mismatch rate between Au and a silicon substrate and the generation of an amorphous ZnO layer, an Au-coated silicon substrate has inevitable limitations for the alignment of nanowires. Consequently, my research has focused on a new synthetic approach to nanowire alignment that uses ZnO nanoparticles. According to a previous study[98], vertically aligned nanowires were grown at temperatures ranging from 400°C to 500°C in the metal-organic chemical vapor deposition (MOCVD) system by using zinc organometallic precursors without seeds. It is noteworthy that in this earlier experiment, either the self-generated ZnO nuclei cluster or the reservoir on the sapphire substrate could be the cause of the vertical alignment. Therefore, introduction of the aligned ZnO seed texture for the homo-epitaxy on the silicon substrate before the growth occurs carries the possibility of manipulation of the orientation, diameter, and density of the resultant nanowires. With this strategy in mind, solution-phase ZnO nanocrystal seed will be discussed in this section as a way to synthesize aligned vertical ZnO nanowire arrays.

3.3.1 Introduction to Controlling C-Axis Alignment in ZnO Nanocrystal Seeds

It has been shown that the performance of LEDs and solar cells are significantly influenced by the directionality, uniformity, length, and spacing of the nanowire arrays[92,99,100]. The challenge in growing well-aligned vertical nanowires is attributed to either a lattice mismatch between ZnO and the substrate or to accumulated strain in the material during the growth process that typically results in randomly oriented nanowires[101,102]. Vertically aligned ZnO nanowires are normally obtained on single crystalline substrates, such as ZnO, sapphire (Al_2O_3), and gallium-nitride (GaN)[91,97,103,104]. The diameter and position of nanowires can be determined by patterns of catalysts using e-beam or laser interference lithography[103-105]. The drawbacks of this approach include the requirement for specialized and costly substrates and the presence of catalyst impurities in nanowires that potentially affect their electrical and optical performance[104].

Homoepitaxy methods using ZnO nanocrystalline seeds coated on the surface of silicon (Si) substrates provide a more favorable approach in terms of cost and versatility.

Previous reports suggest recourse to synthetic methods of generating ZnO nanocrystal seeds to initiate their growth, deriving these seeds from either zinc acetate combined with either sodium hydroxide (NaOH) or from potassium hydroxide (KOH), or simply from zinc acetate alone[62,65,92]. Despite the successful growth of vertically aligned nanowires through these methods[92], consistent alignment from these synthetic methodologies remains a challenge. Some groups have successfully obtained vertically aligned ZnO nanowires, but others have not[22,62,92,104,106]. We have noticed that in earlier reports the concentration of NaOH was altered as a way to control the size and the crystalline properties of the seed particles[107]. In our own experiments, we have noticed that, although vertically aligned nanowires were consistently obtained at low levels of NaOH, insoluble $Zn(OH)_2$ aggregated on the substrate and caused uneven surface coverage. On the other hand, at higher concentrations of NaOH, these particles fully dissolved to form zincate ions ($Zn(OH)_4^{2-}$) but the nanowires that were grown were randomly oriented. This study explores the mechanism that leads to this misorientation and demonstrates an alternative approach to seed formation that reliably yields vertically aligned nanowires with consistent coverage. As zincate ions dry on the surface, Na (or K) is incorporated into the seed material to maintain a neutral charge. These metallic impurities, upon annealing, tend to disorient the crystal axis of the ZnO seeds on the surface. However, when we changed our base for the formation of ZnO nanocrystalline seeds from NaOH (or KOH) to ammonium hydroxide (NH_4OH), we consistently realized well-aligned vertical ZnO nanowire arrays with high surface coverage at all levels of NH_4OH concentration. The existence of metallic impurities on nanocrystalline seeds made using NaOH- or KOH-based solutions was confirmed by x-ray photoelectron spectroscopy (XPS). We used transmission electron microscopy (TEM) to analyze the lattice-resolved images and electron diffraction patterns. This analysis confirmed that unlike the seeds resulting from NaOH and KOH solutions, the NH_4OH-based seed solution results in seed layers whose c-axis crystal orientation is aligned normally with the substrate over a wide concentration range.

3.3.2 Experimental Procedures to Synthesize ZnO Nanocrystal Seeds

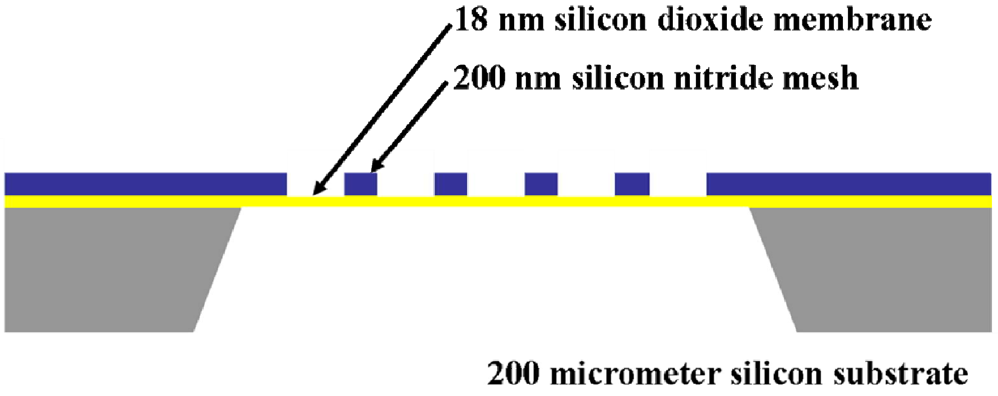

Figure 3.13[108]: Schematic of a TEM grid made of thin silicon dioxide membrane

ZnO nanowires were grown on an amorphous substrate (silicon dioxide layer on top of a silicon substrate) using nanometer-scale crystalline ZnO seeds. The ZnO seeds were synthesized from a seed solution prepared by mixing 0.01 M zinc acetate dihydrate [Fluka, assay>>99.5 %] with various concentrations (0.03 M, 0.06 M, and 0.09 M) of either sodium hydroxide (NaOH) [Fisher Scientifics, assay>>98.6 %], potassium hydroxide (KOH) [Fisher Scientifics, assay>>85.9 %], or ammonium hydroxide (NH_4OH) [Fisher Scientific, assay=29.5 %, 14.8 normality] dissolved in methanol [OmniSolv, assay=99.9 %]. For control experiments, 0.06 M or 0.27 M sodium acetate (CH_3COONa) [Alfa Aesar, anhydrous, assay = 99%], 0.06 M sodium nitrate ($NaNO_3$) [Acros Organics, assay = 99+%] and 0.09 M sodium chloride (NaCl) [Fisher Scientific, assay>99%] were also added to the above seed solutions to control the concentrations of Na in the solutions without changing their OH^- concentrations. The mixtures were thoroughly stirred at 60 ^oC for 2 hours in water baths[62,92]. Silicon substrates with a thin silicon dioxide layer were coated with 6-7 droplets of the prepared seed solution, then rinsed with clean methanol several times to ensure deposition of zinc hydroxide ($Zn(OH)_2$) on the substrates. The drop-coated substrates were subsequently annealed at 350^oC for 20 minutes to decompose the zinc hydroxide into ZnO and water[62,92]. This synthesis procedure created ZnO crystalline seeds. These were then used as a template for growth of ZnO nanowires via chemical vapor transport in an experimental setup as shown in Figure 3.1[89].

In the growth process, equal amounts of ZnO powder [Acros Organics, 99.5+%] and graphite (C) powder [Alfa Aesar, crystalline, ~300 mesh, assay 99%] (~0.6 g) were ground and placed in an alumina boat located in the middle of the tube furnace [Lindberg Blue M, TF55035A], where the substrate was located downstream in the quartz tube (inner diameter: 2.54 cm; length: 90 cm). The furnace temperature was ramped to 920 ^{o}C in approximately 15 minutes and maintained for 30 minutes under an argon (~50 sccm) and oxygen (~1 sccm) flow. After the growth process, the characteristics of the nanowire were investigated by using a scanning electron microscope (SEM, FEI XL 30 SEM-FEG), an x-ray diffraction system (XRD, Panalytical X'Pert PRO MRD HR X-Ray Diffraction System) and x-ray photoelectron spectroscopy (XPS, Kratos Analytical Axis Ultra). The analysis of seed alignment was conducted using bright field imaging and a diffraction contrast mode in a transmission electron microscope (TEM, FEI Tecnai G^2 Twin). Samples observed under TEM were grown on a special TEM grid made up of a thin silicon dioxide membrane on a silicon nitride mesh (Figure 3.13[108]).

3.3.3 Growth of Vertically Aligned ZnO Nanowire Arrays Made Using ZnO Nanocrystal Seeds

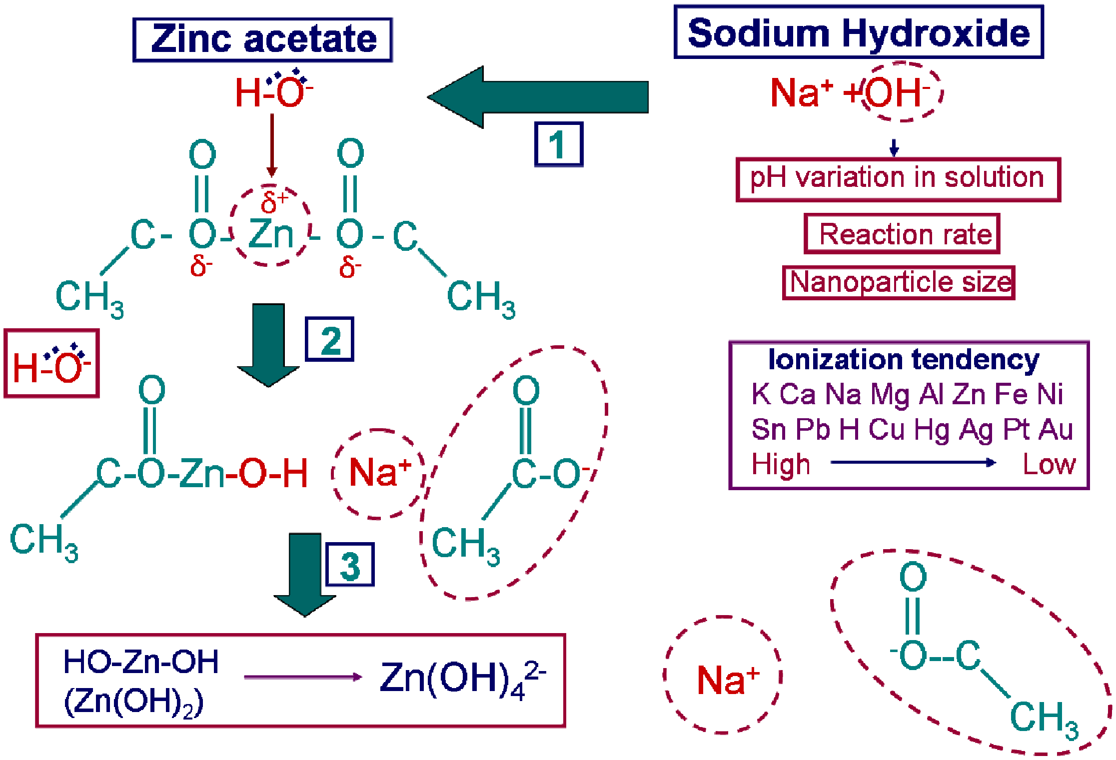

Figure 3.14: Schematic of the chemical reactions in a complex solution of 0.01 M zinc acetate ($Zn(O_2CCH_3)_2$) and 0.03 M sodium hydroxide (NaOH). In this reaction, a hydroxyl group (OH^-) combined with a divalent zinc ion (Zn^{2+}) generates zinc hydroxide ($Zn(OH)_2$). As OH^- increases, $Zn(OH)_2$ reduces the zincate ion ($Zn(OH)_4^{2-}$.

An approach using a solution that combined zinc acetate ($Zn(O_2CCH_3)_2$) with sodium hydroxide (NaOH) in methanol was originally introduced in 2002 by C. Pacholski *et al.*[65]. The ZnO nanoparticle seeds that were used were prepared through the decomposition of 0.01M zinc acetate with 0.03M sodium hydroxide in methanol. To obtain divalent zinc ions in this solution, hydrothermal stirring at 60 ^{o}C was performed for 2 hours in a water bath.

Figure 3.14 illustrates how ZnO nanoparticles can be synthesized in this complex solution. Because of the high ionization tendency of sodium (Na), the NaOH is easily decomposed to sodium cation (Na^+) and hydroxide anion (OH^-) in the organic solvent, methanol. In this process, the OH^- affects the pH of the complex solution. As a result, the concentration of OH^- influences both the reaction rate and the size of the nanoparticle. To induce ZnO from the zinc salt , the zinc ionic force on the equilibrium of the aqueous complex inevitably requires a hydrothermal condition or neutralization of the chemical complex[109]. Therefore, the stirring process in this mixed solution was performed at 60^{o}C for 2 hours in a water bath. Zn is a transition metal that has an unstable d-orbital. Oxygen has high electro-affinity. Consequently, oxygen, which has four unbound electrons in OH^-, easily breaks the chemical bond between the zinc and acetate group in zinc acetate and then creates zinc hydroxide ($Zn(OH)_2$). As NaOH increases, this precipitate of $Zn(OH)_2$ can change to zincate ions ($Zn(OH)_4^{2-}$) in this aqueous solution. Finally, a thermal annealing treatment at 350^{o}C for 20 min in air causes this $Zn(OH)_2$ to transform the layer of ZnO nanocrystal seeds on the silicon substrate.

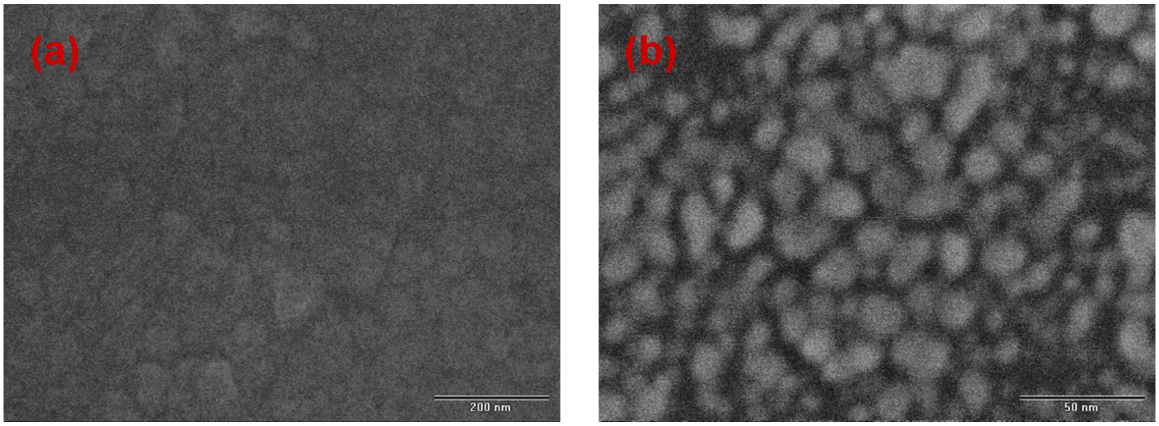

Figure 3.15: SEM images (a) and (b), respectively, show ZnO nanocrystal seeds on a silicon substrate before and after a 350°C annealing treatment for 20 min in air.

SEM images (a) and (b), respectively, show in Figure 3.15 the ZnO nanocrystal seeded silicon substrate before and after a 350°C annealing treatment for 20 min in air. For ease of imaging, the SiO_2 layer on the silicon substrate was eliminated with a hydrogen fluoride (HF) solution. Differences in the surface topology of these two substrates before and after the annealing treatment are clearly visible. A moderate annealing treatment created the ZnO nanocrystal seed cluster. The seeds were quite uniform, and their diameters were 5-20 nm. In order to grow ZnO nanowire arrays from these textured seeds, furnace input temperatures ranging from 900 °C to 940 °C were used in 50 °C/min increments. To monitor variations in the morphology of the seed layer during the process of increasing temperatures in the furnace, the silicon substrate coated with ZnO seeds, which was loaded at 800 °C for 5 min, was removed from the furnace.

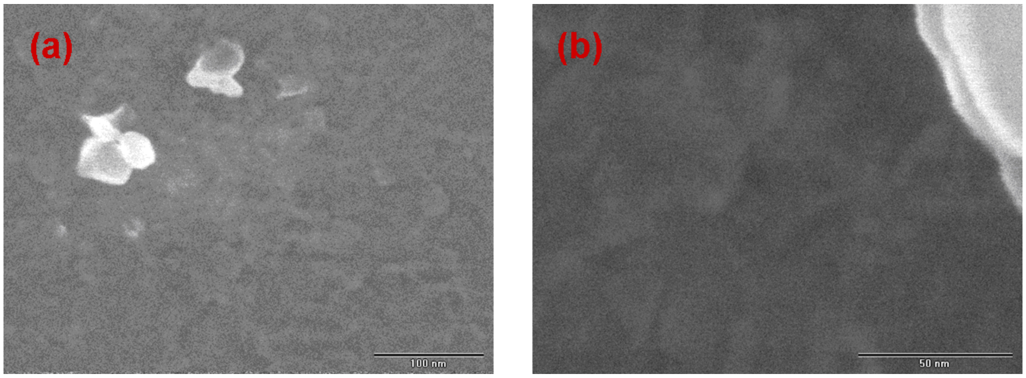

Figure 3.16: SEM images (a) and (b) show the topological variation from ZnO nanocrystal seeds to ZnO thin film on a substrate during the growth process. This sample was removed from the furnace at 800°C.

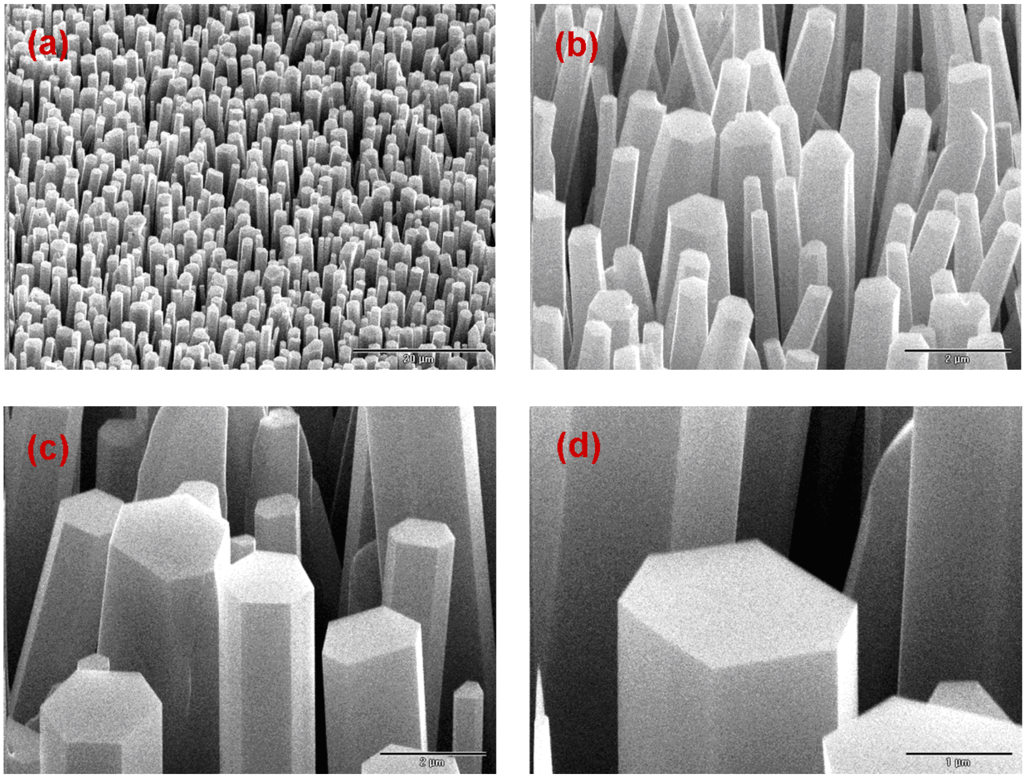

Figure 3.17: SEM images (a), (b), (c), and (d) show aligned vertical ZnO nanowire arrays on a silicon substrate. These nanowires were grown from textured ZnO nanocrystal seeds. Details of the growth conditions were 1 sccm O_2 mixed with 49 sccm Ar at 930°C.

As shown in Figure 3.16, the cluster of ZnO nanocrystal seeds coalesced and then formed the textured ZnO thin film. Figure 3.17 displays SEM images of as-grown vertical ZnO nanowire arrays on this preexisting textured ZnO thin film. In these experiments, the mixture of 49 sccm Ar and 1 sccm O_2 were supplied as feeding gases at input furnace temperatures of 900-940^{o}C.

Unlike Au film seeds, ZnO seed film generated only high density and aligned vertical nanowires in sizes with diameters of 200 nm to 2 μm and lengths of 7 to 10 μm. Seed aggregation at high temperature causes the large diameters. An interesting feature of the growth from these ZnO textured seeds was that the length dispersion of the nanowires resembled a Gaussian distribution. This means that the specific local temperature in the tube determines the longest length of ZnO nanowires. Therefore, application and maintenance of optimal local temperatures during the growth of these nanowires can use silicon wafers to easily synthesize high quality vertical ZnO nanowire arrays.

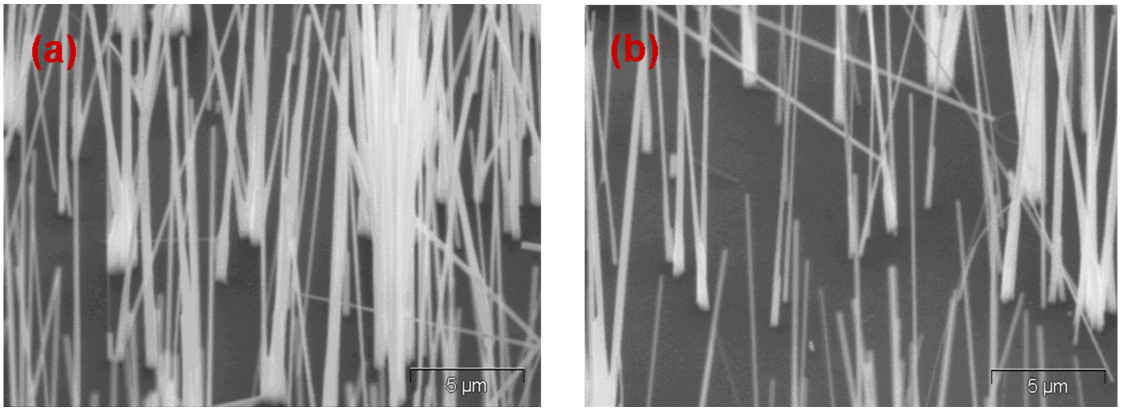

Figure 3.18: SEM images (a) and (b) show a low density area in an as-grown sample. In these images, each nanowire was vertically aligned regardless of area density.

Two hypotheses have been advanced to explain the generation of vertically aligned nanowire arrays from ZnO nanocrystal seeds. One is that high density seeds prohibit random oriented growth because they compress neighboring nanowires during their growth. The second hypothesis holds that all of the ZnO nanocrystal seeds in the experiment undertaken here are textured to the c-axis, which is perpendicular to the substrate[92]. Figure 3.18 supports the latter hypothesis as more realistic. In this figure, despite the low density and large spaces between the as-grown nanowires, the alignment was normal to the substrate.

According to previous reports[92], the polar {001} surface of ZnO has been known to be unstable electrostatically. This polar surface energy has been known to be 60% higher than such nonpolar surfaces as {100} planes and {110} planes[92]. Additionally, the c-direction is the direction of fastest growth for ZnO regardless of the substrates or growth methods involved[92]. Based on these facts, the c-axis texturing of the ZnO seed layer is contradictory because generation of the polar {001} surface requires higher energy than energy generation for the others. Several hypotheses could be advanced to explain and resolve this contradiction[92]. One is that molecules adsorb on the {001} facet[92]. Thus, these adsorbed molecules stabilize the polar surface and lower the polar surface energy. In this experiment, either an acetate or hydroxyl group could serve as these molecules. A second hypothesis is that the thickness of the seed layer affects the {001} surface energy of the planes[92]. Therefore, the thin seed layer generates the low surface energy in the {001} facet. A third hypothesis is that the structural alteration on the outside of the seed layer occurs in the generation of the {001} facet[92]. The graphitic arrangement can exist in the thin ZnO film and then be transformed into the {001} wurtzite facet. To date, however, there has been no clear demonstration of a preferential c-plane alignment in a ZnO wurtzite structure. And the stability of polar {001} facets is an issue in the field of crystalline science.

3.3.4 Formation Mechanism of Preferential C-Axis Oriented ZnO Nanocrystal Seeds

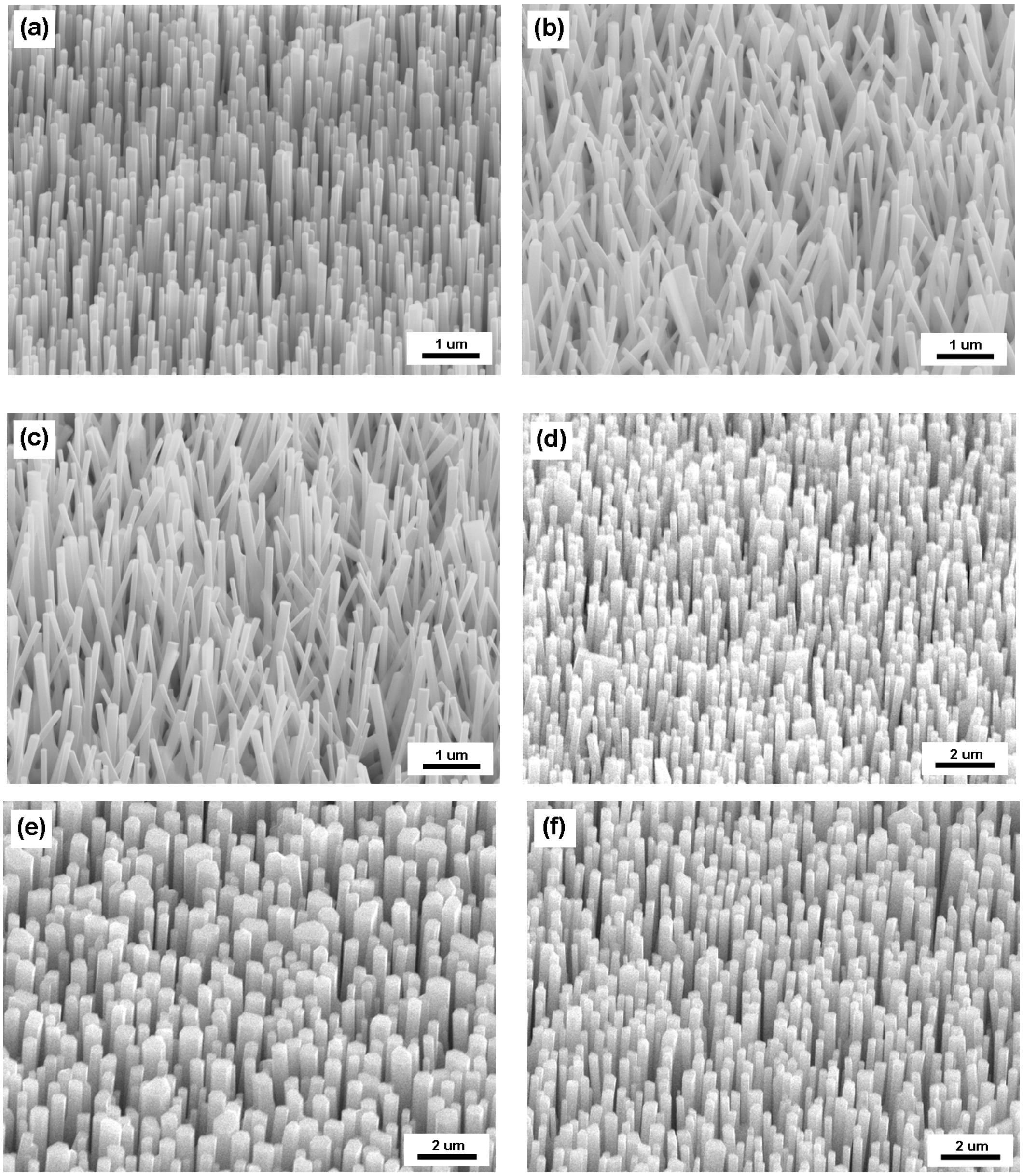

Figure 3.19: SEM images of ZnO nanowire arrays grown from (a) 0.03 M, (b) 0.06 M and (c) 0.09 M NaOH-derived seeds; (d) 0.03 M, (e) 0.06 M and (f) 0.09 M NH_4OH-derived seeds. Images were taken at a 52° angle with respect to the substrate.

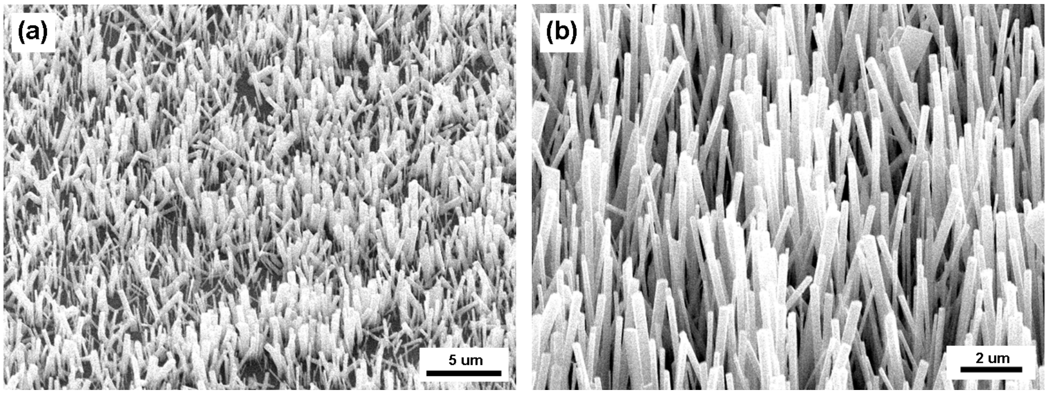

Figure 3.20: (a) and (b) show 52° angle views of SEM images of nonvertical ZnO nanowires on the SiO_2/Si substrate. Here, misaligned ZnO nanowires were grown from seeds using 0.01 M zinc acetate alone ($Zn(O_2CCH_3)_2$).

Figure 3.19 (a) shows vertical nanowires grown from the ZnO seeds synthesized using 0.03 M sodium hydroxide (NaOH) combined with 0.01 M zinc acetate ($Zn(O_2CCH_3)_2$). One can confirm that supplying hydroxide ions (OH^-) to zinc acetate ($Zn(O_2CCH_3)_2$) plays a critical role in the formation of ZnO nanocrystalline seeds; this is particularly true in comparison with the nanostructures grown from seeds made using zinc acetate ($Zn(O_2CCH_3)_2$) alone, as shown in Figure 3.20.

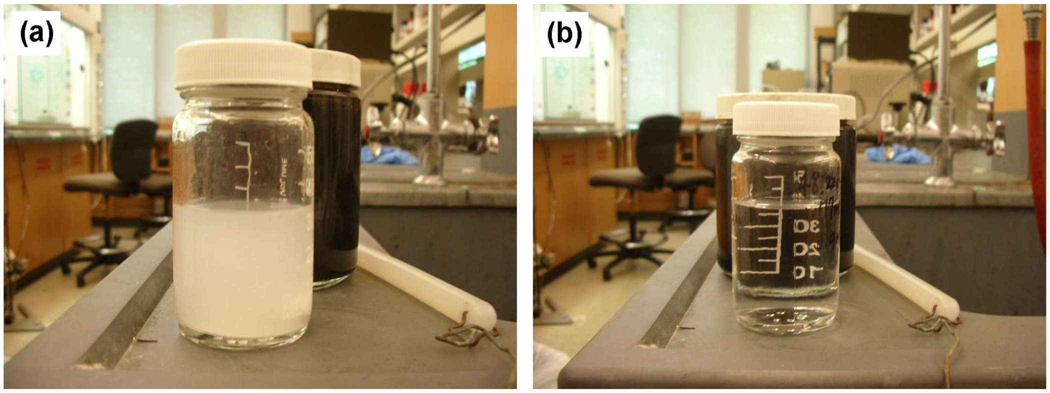

Figure 3.21: ZnO seed solutions made using (a) 0.03 M NaOH combined with 0.01 M zinc acetate and (b) 0.06 M NaOH combined with 0.01 M zinc acetate.

The reaction of hydroxide ions (OH^-) with zinc acetate ($Zn(O_2CCH_3)_2$) results in zinc hydroxide ($Zn(OH)_2$), which is insoluble in methanol and forms a suspension of micron-scale precipitate in the solvent (Figure 3.21 (a)). These neutral $Zn(OH)_2$ particles of varying sizes in the seed solutions are deposited on the substrate surface and reduce to ZnO nanocrystal seeds upon annealing with c-axis alignment normal to the substrates. These events lead to the growth of vertically aligned ZnO nanowires (Figure 3.19 (a)).

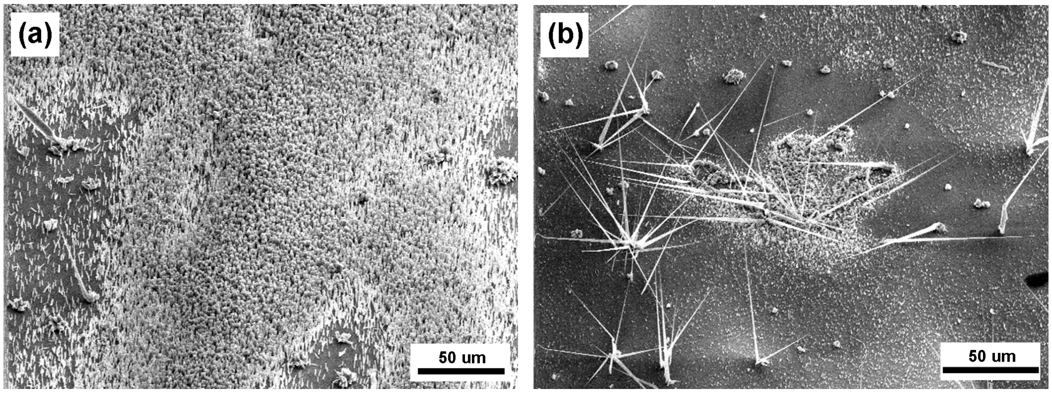

Figure 3.22: (a) and (b) show a 52° angular view of SEM images of ZnO nanostructures on a SiO_2/Si substrate. These images show the white precipitate residuals that occur in a seed solution of 0.03 M NaOH combined with 0.01 M zinc acetate. These precipitates inhibit uniform and high density nanowire growth.

However, we often observed the origination of nonuniform ZnO nanowire growth from large white precipitates in the seed solutions adsorbed to the substrates as shown in Figure 3.22 (a) and (b). At higher concentrations of NaOH, more hydroxide ions (OH^-) bind with the zinc hydroxide ($Zn(OH)_2$) to form zincate ions ($Zn(OH)_4^{2-}$), which are soluble in methanol, and turn the mixture transparent as shown in Figure 3.21 (b). The transparent seed solutions prepared in this way lead to uniform and high density seeds on the substrates that are free of clumps originating from the precipitates. However, increasing the sodium concentration leads to the growth of misaligned nanowires as shown in Figure 3.19 (b) and (c). This misalignment is attributed to the incorporation of metallic Na atoms into the ZnO seed crystals (See below). Similar behavior was observed when NaOH was replaced with KOH.

To solve this problem, we turned to ammonium hydroxide (NH_4OH), an analogue of NaOH in which an ammonium ion (NH_4^+) is substituted for the sodium ion (Na^+). Because the ammonium ion (NH_4^+) will decompose under heat and dissipate from the substrate in the form of ammonia (NH_3), we can prevent the incorporation into the seed crystals of metallic impurities that might otherwise impede seed alignment. This approach yielded immediate improvement in the orientation of ZnO nanowires at all concentrations of NH_4OH in the seed solutions. Figure 3.19's (d), (e), and (f) show, respectively, vertically aligned uniform nanowire arrays grown from ZnO seeds synthesized using 0.03 M, 0.06 M, and 0.09 M NH_4OH combined with 0.01 zinc acetate ($Zn(O_2CCH_3)_2$) in methanol. In contrast to the creation of misaligned nanowires at high NaOH concentrations, the vertical alignment of nanowire arrays was unaffected by different concentrations of NH_4OH. These experiments show that NH_4OH yields a complete ZnO seed layer without incorporating metallic impurities and maintains the vertical alignment of nanowires grown from these seed crystals.

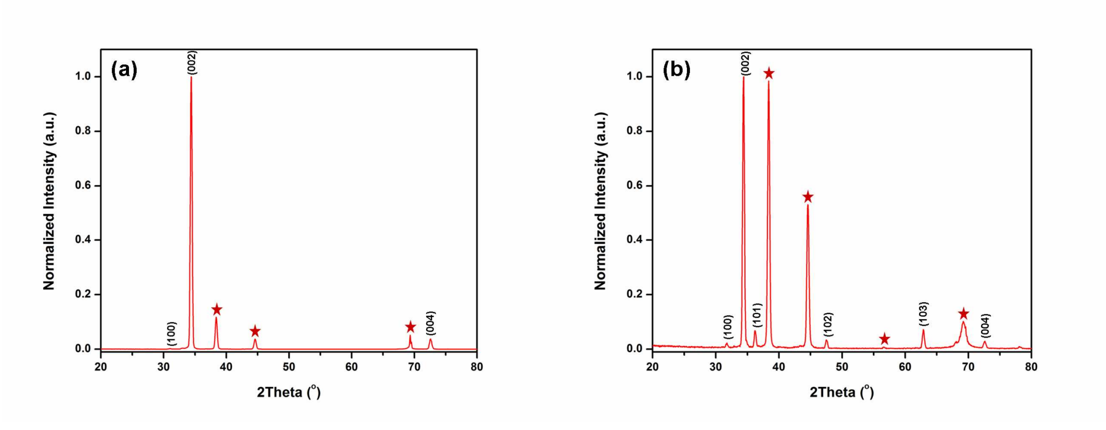

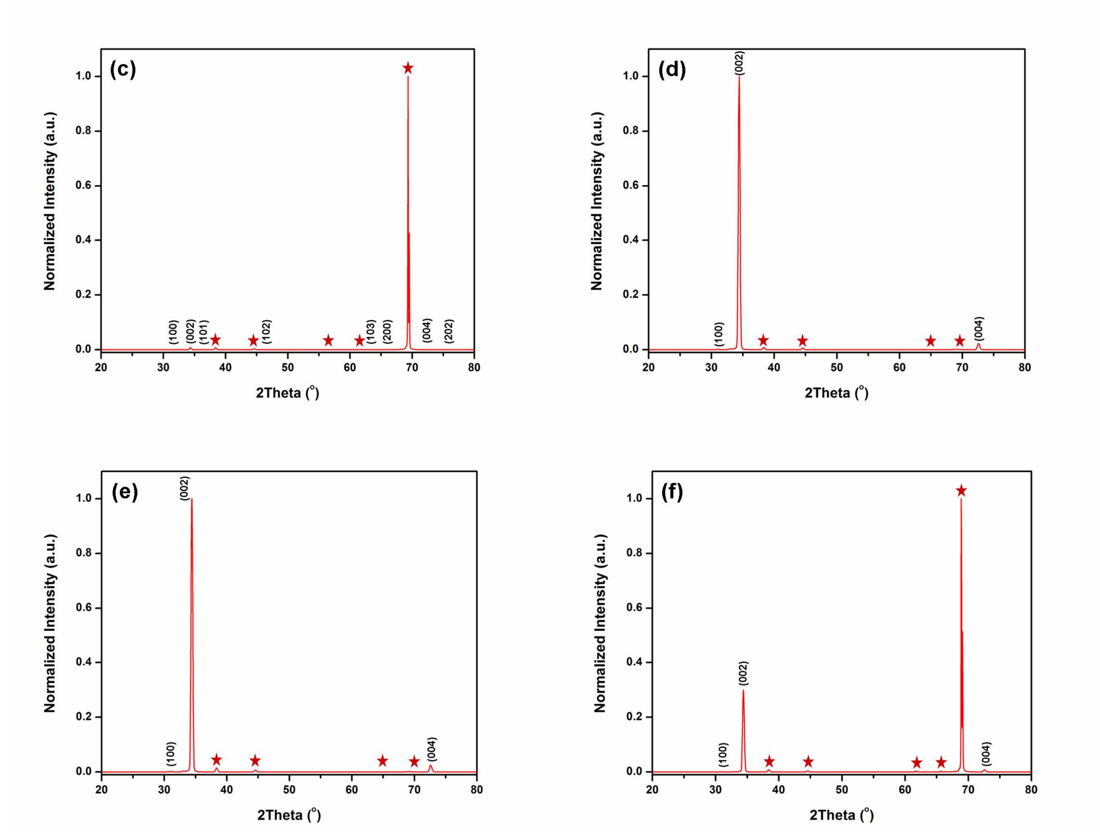

Figure 3.23: (a), (b), and (c) show the X-ray diffraction (XRD) patterns of nanowires grown from seeds using 0.03 M, 0.06 M, and 0.09 M NaOH combined with 0.01 M zinc acetate; (d), (e), and (f) illustrate the XRD patterns of nanowires grown from seeds using 0.03 M, 0.06 M, and 0.09 M NH_4OH combined with 0.01 M zinc acetate. Asterisks indicate peaks generated from SiO_2/Si substrates. Small peaks of (100) and (004) were common to all our samples.

In addition to the SEM images, the vertical alignment of nanowires is also confirmed through x-ray diffraction (XRD) patterns as shown in Figure 3.23. The samples grown from NaOH-derived seeds, except 0.03 M, show different peaks originating from all of the crystal surfaces of ZnO, which indicates the nonuniform crystal orientation of ZnO nanowires on the substrate. The samples grown from

NH_4OH-derived seeds present a high intensity peak at (002) and (004). This indicates that the c-axis of the ZnO crystal is aligned perpendicular to the substrate and that no other crystal orientation exists in the substrate plane. Although we tried to use the XRD technique for direct observation of the crystal orientation of the seeds, the thin seed samples did not yield enough XRD signals for us to arrive at unambiguous measurements of the crystal planes.

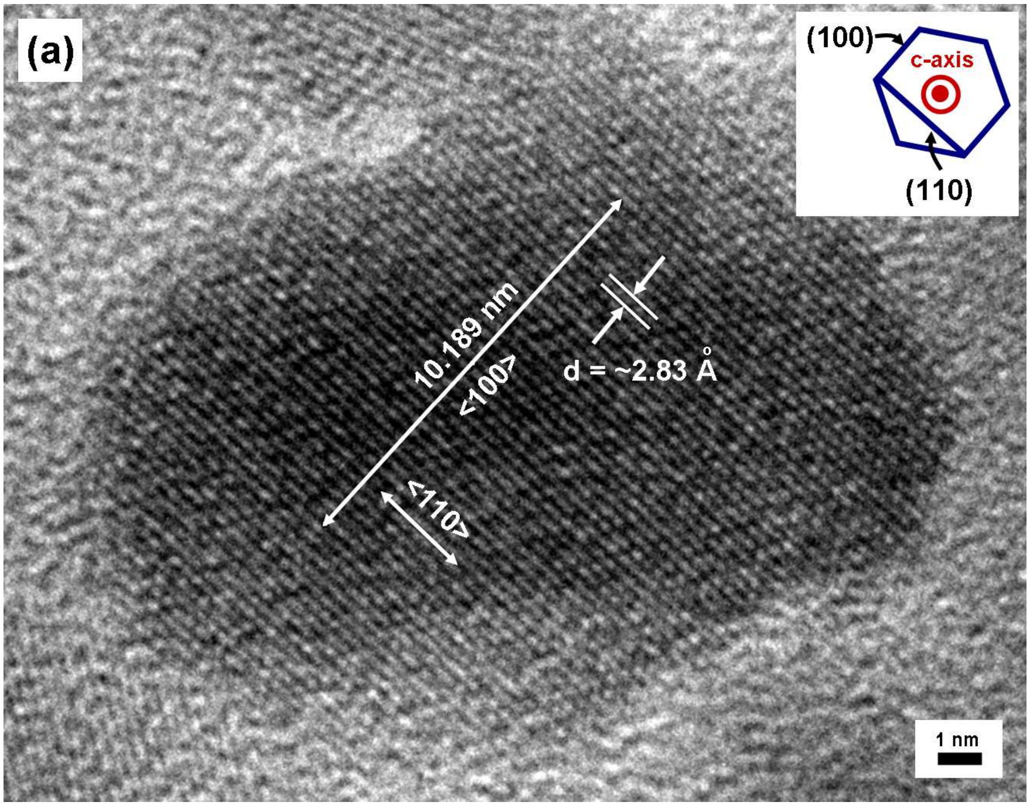

Figure 3.24: (a) A TEM image of 0.06 M NH_4OH-derived seeds grown on the SiO_2 membrane of a TEM grid. The inset in the upper right corner represents a top view of the c-plane of a ZnO wurtzite structure. Labeled lattice directions on the seed image imply that the direction of the c-axis is perpendicular to the seed layer.

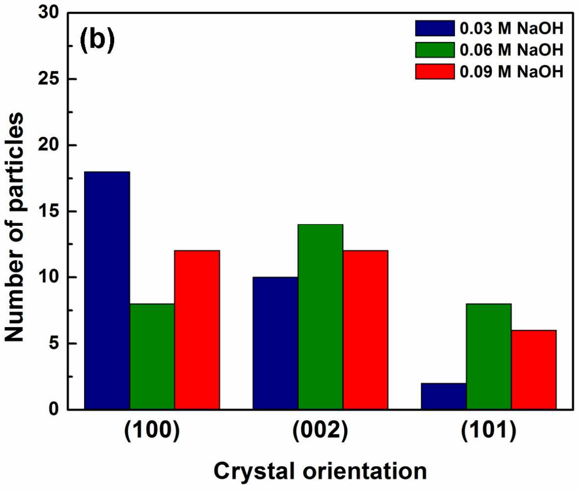

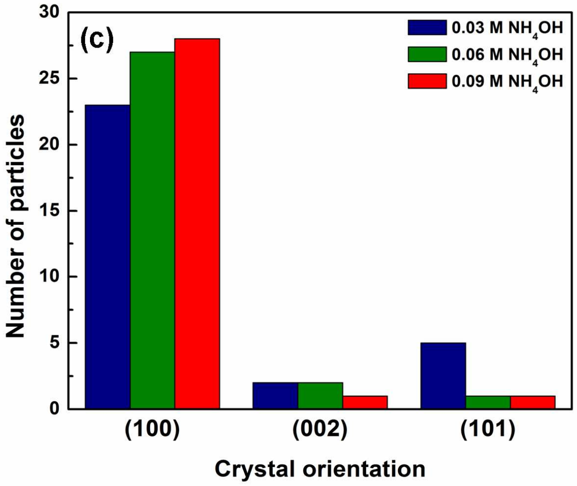

Figure 3.24: Bar graphs (b) and (c) represent histograms of the crystal orientation distribution of ZnO nanocrystalline seeds, which were counted based on the lattice spacing on seed images acquired by TEM. In both histograms, the blue, green, and red bars indicate, respectively, the number of seeds generated from 0.03 M, 0.06 M, and 0.09 M of (a) NaOH and (b) NH_4OH, combined with 0.01 M zinc acetate.

To verify the crystal orientation of the ZnO seed layer as a function of the concentration of different bases, we prepared the ZnO seeds on a TEM grid made of thin silicon dioxide membrane, as shown in Figure 3.13 (Ted Pella, Inc., 18 nm thickness, 0.5x0.5 mm window). This procedure was identical to that used in nanowire growth. Figure 3.24 (a) shows one of the ZnO nanocrystalline seeds synthesized by using the combined solution of 0.06 M NH_4OH with 0.01 M zinc acetate. The lattice constant of the seed crystal in the substrate plane can be directly measured from such images. For example, Figure 3.24 (a) shows a TEM image of a seed particle showing a lattice constant of ~2.83 Å, which corresponds to the separation of (110) planes. We collected random samples of 30 such seed images from each sample and plotted a histogram of observed lattice orientation as a function of the base type and concentration. Elements (b) and (c) of Figure 3.24 show histograms for seed samples prepared with NaOH and NH_4OH solutions, respectively. The histograms show the distinct preference of seeds to orient their (001) planes parallel to the substrate surface when the concentration of NaOH is low (0.03M); however, this preference largely disappears when the NaOH concentration exceeds 0.06 M. In contrast, the seed crystals orient preferentially, with (001) planes parallel to the surface, on substrates in the case of NH_4OH-based solutions regardless of the concentrations.

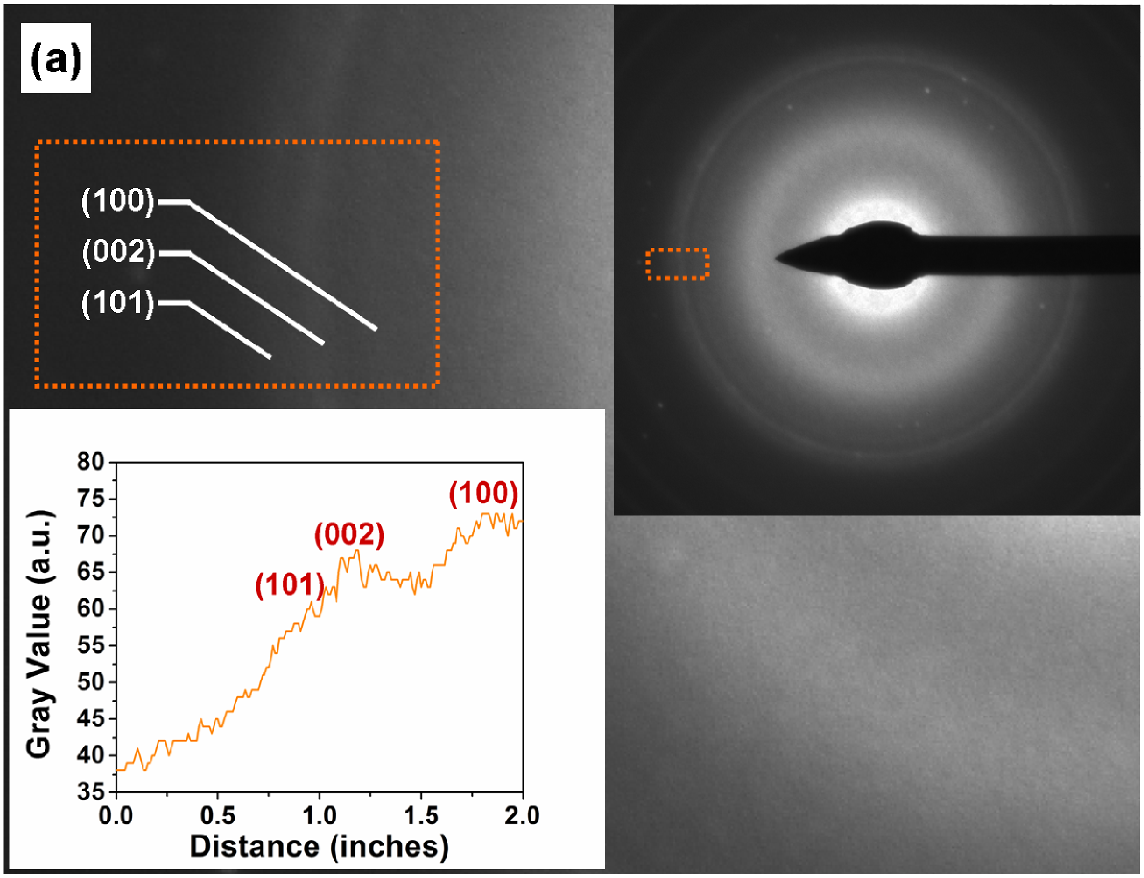

Figure 3.25: (a) A selected area electron diffraction (SAED) image of 0.09 M NaOH-derived seeds containing (002) rings; the upper right inset shows a zoomed-out view, and the bottom left inset shows three shoulders corresponding to (101), (002), and (100) in terms of the gray values.

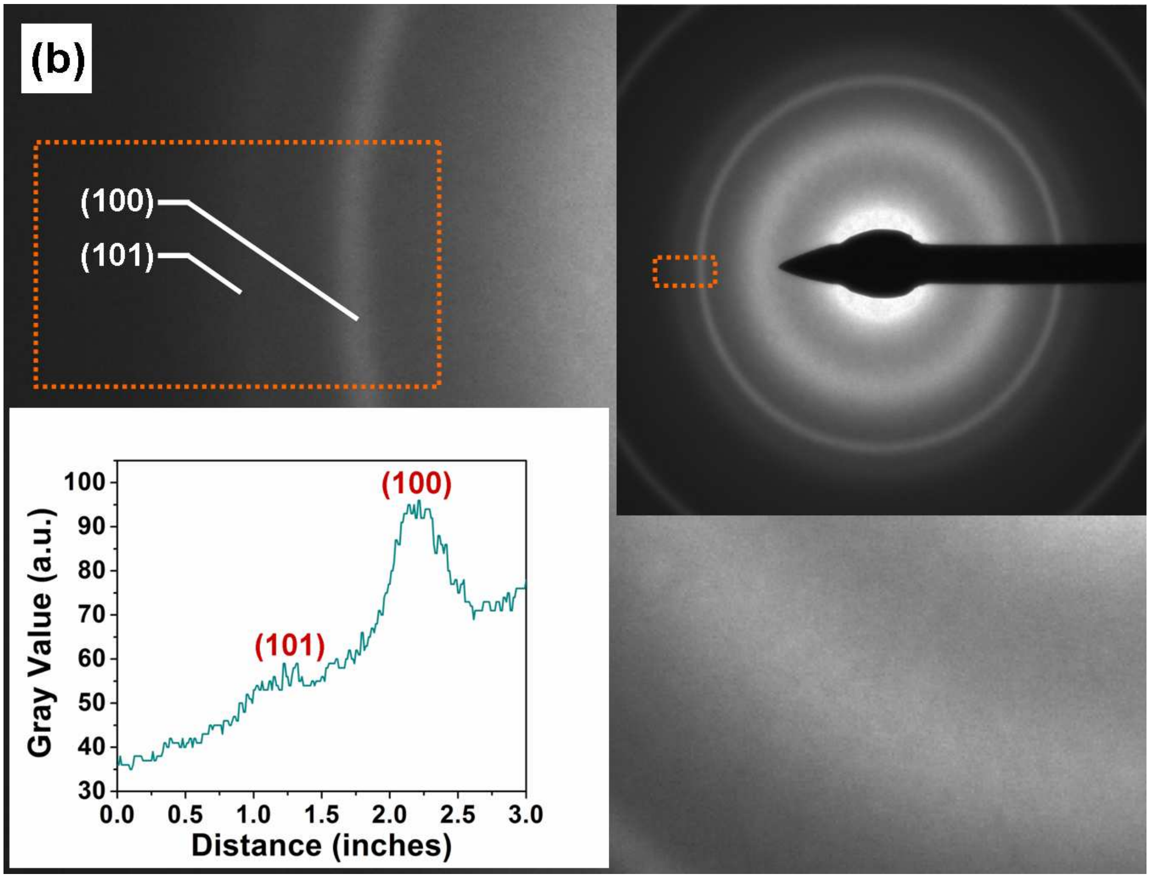

Figure 3.25: (b) a SEAD image of 0.09 M NH_4OH-derived seeds missing their (002) ring confirms the c-axis alignment of seeds; the upper right inset shows a zoomed-out view, and the bottom left inset shows one shoulder and a high peak corresponding to (101) and (100) in terms of gray values.

A similar conclusion can be drawn from the comparison of selected area electron diffraction (SAED) images shown in Figure 3.25. SAED looks at far-field diffraction patterns of electron beams focused on a specific area of the TEM membrane grid. Figure 3.25 (a) corresponds to the seed layers prepared using a NaOH solution. The diffraction rings show three peaks, corresponding to crystal planes (100), (002), and (101) lying in the plane of the substrate membrane. The inset shows the cross-section of rings showing the three peaks. Figure 3.25 (b) shows a similar diffraction of the seed layers prepared using a NH_4OH solution. In this case, the predominant diffraction ring corresponds to the (100) plane, and the (002) peak is missing. These characteristics indicate that most of the seeds have their c-axis aligned perpendicular to the substrate plane. The relative strength of these three peaks is consistent with the statistics of the lattice constants measured directly in (b) and (c) of Figure 3.24.

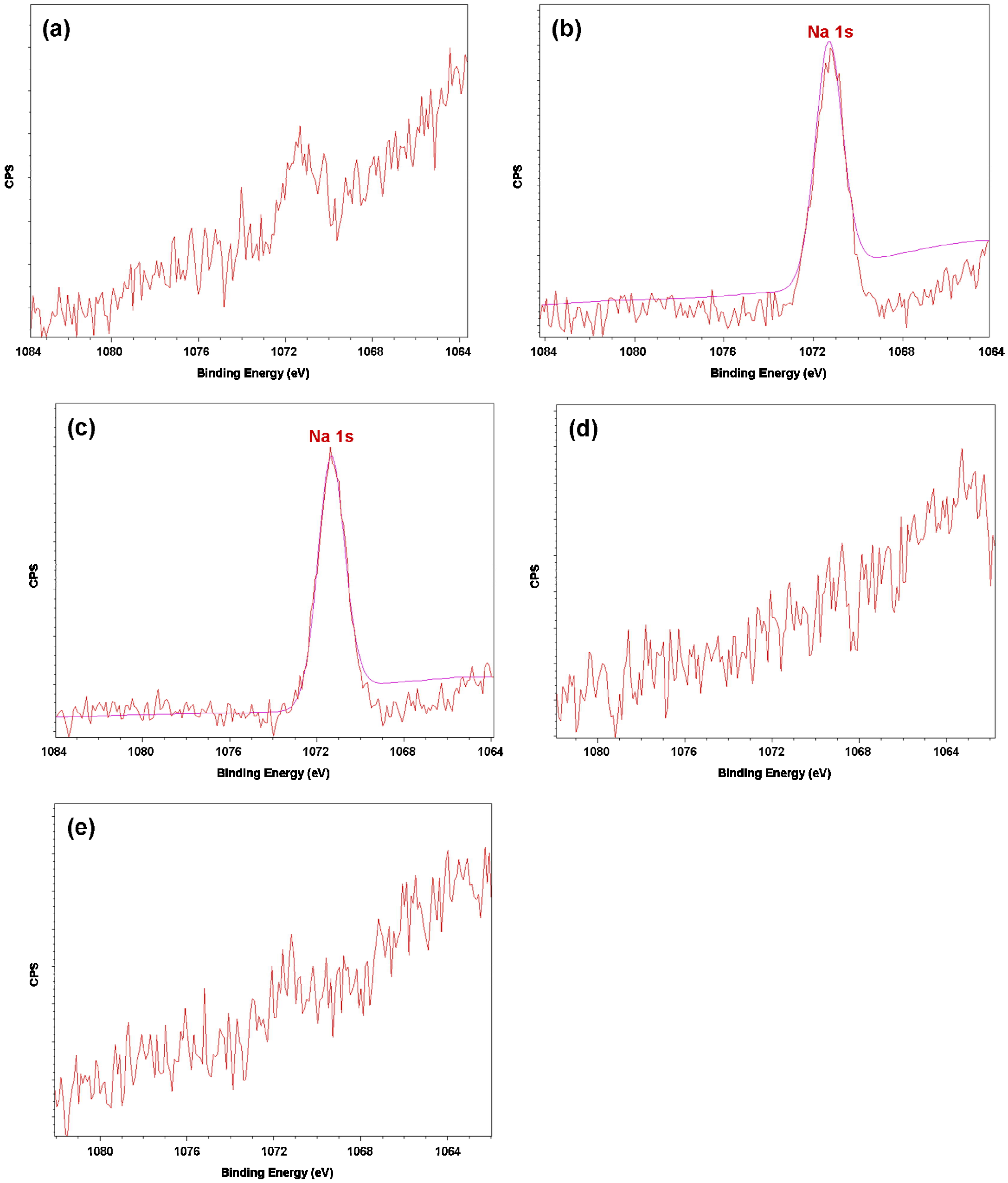

Figure 3.26: Core-level XPS corresponding to the Na 1s peak detected from ZnO nanocrystalline seeds prepared by using 0.01 M zinc acetate combined with (a) 0.03 M NaOH, (b) 0.06 M NaOH, and (c) 0.09 M NaOH; (d) 0.03 M NaOH and 0.06 M sodium acetate (CH_3COONa); and (e) 0.03 M NaOH and 0.06 M sodium nitrate ($NaNO_3$).

Table 3.2: The atomic percentage of Na impurities detected at the surface of ZnO nanocrystalline seeds in XPS

	0.03 M NaOH-based seeds	0.06 M NaOH-based seeds	0.09 M NaOH-based seeds
Na (atom %)	0	2.33	2.41

We attribute the main source of misalignment to the incorporation of metallic Na (or K) impurities in the ZnO seed crystals. X-ray photoelectron spectroscopy (XPS) was performed on SiO_2 substrates coated with ZnO seeds so as to directly detect the presence of metallic Na impurities. Figure 3.26 (a)-(e) show the core-level spectra of Na in XPS. Although 0.03 M NaOH-based seeds on the substrate do not show any peak during regional scanning in XPS, ZnO seeds on substrates derived from 0.06 M and 0.09 M NaOH solutions show the sodium 1s peak, which indicates the presence of sodium impurities and therefore, their role in the subsequent misalignment of nanowires. Table 3.2 shows the atomic concentrations of Na in XPS corresponding to Figures 3.26 (a)-(c). The correlation between detected Na levels in the seed, the orientation of seed crystals, and the subsequent alignment of nanowires is a strong indicator that the impurities disorient the crystalline ZnO seeds.

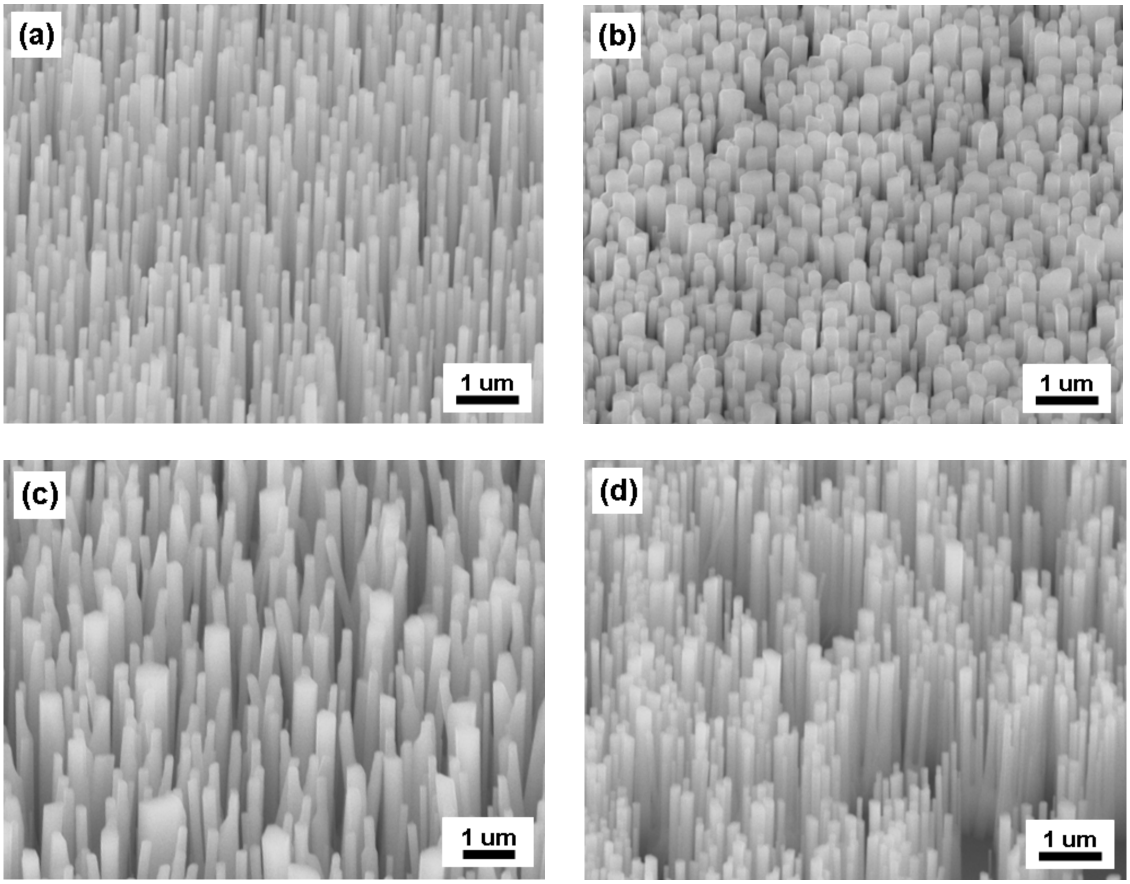

Figure 3.27: SEM images of ZnO nanowire arrays grown from seeds synthesized by using 0.01 M zinc acetate combined with (a) 0.03 M sodium hydroxide (NaOH) and 0.06 M sodium acetate (CH_3COONa); (b) 0.03 M sodium hydroxide (NaOH) and 0.06 M sodium nitrate ($NaNO_3$); (c) 0.09 M ammonium hydroxide (NH_4OH) and 0.09 M sodium chloride (NaCl); and (d) 0.09 M ammonium hydroxide (NH_4OH) and 0.27 M sodium acetate (CH_3COONa). Images were taken from a 60° angle with respect to the substrate.

To understand the mechanism of Na incorporation into the seeds, we performed control experiments that used varying concentrations of Na in the seed solution while holding the OH^- concentration constant. Figure 3.27 shows SEM images of vertically aligned ZnO nanowires grown from the nanocrystalline seeds synthesized by using 0.01 M zinc acetate ($Zn(O_2CCH_3)_2$) in several combinations. These are (a) 0.03 M sodium hydroxide (NaOH) and 0.06 M sodium acetate (CH_3COONa); (b) 0.03 M sodium hydroxide (NaOH) and 0.06 M sodium nitrate ($NaNO_3$); (c) 0.09 M ammonium hydroxide (NH_4OH) and 0.09 M sodium chloride (NaCl); and (d) 0.09 M ammonium hydroxide (NH_4OH) and 0.27 M sodium acetate (CH_3COONa). Although the total level of sodium cations (Na^+) in the seed solution was equivalent to 0.09 M in Figure 3.27 (a), (b), (c) and much higher in (d), we consistently saw well-aligned nanowires in all of these samples. Furthermore, XPS measurement confirmed that no sodium component was detected in the seed crystals on the surface of the substrates in these samples (two of them as shown in Figure 3.26 (d) and (e)). These experiments indicate that high levels of Na concentration alone do not lead to incorporation of Na into the seeds.

Table 3.3: Estimation of the levels of hydroxide ions (OH^-) in each seed solution. Each seed solution was made by mixing 0.03-0.09 M NaOH with 0.01 M zinc acetate in a methanol solvent and by mixing 0.03-0.09 M NH_4OH with 0.01 M zinc acetate in a methanol solvent.

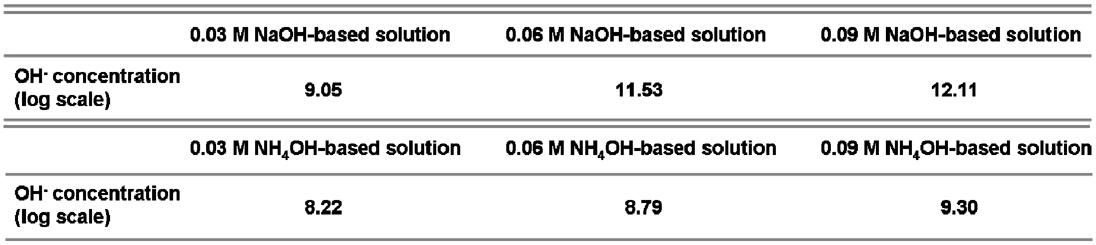

	0.03 M NaOH-based solution	0.06 M NaOH-based solution	0.09 M NaOH-based solution
OH^- concentration (log scale)	9.05	11.53	12.11
	0.03 M NH_4OH-based solution	0.06 M NH_4OH-based solution	0.09 M NH_4OH-based solution
OH^- concentration (log scale)	8.22	8.79	9.30

We measured the concentration of OH^- in various seed solutions by using a conventional pH meter (although methanol was the solvent in our experiments). The OH^- concentrations increased dramatically for NaOH-based solutions as the concentrations of NaOH were increased from 0.03 M to 0.06 M as shown in Table 3.3; this is consistent with the strength of NaOH as a base. For the NH_4OH-based solutions, the OH^- concentration remained relatively low at all levels of NH_4OH concentrations (consistent with the weakness of NH_4OH as a base). Addition of high concentrations of sodium chloride and sodium acetate to 0.09 M NH_4OH-based seed solutions did not lead to either sodium incorporation or misoriented nanowires; this result strongly indicates that high OH^- concentrations drive incorporation of metallic impurities.

At low levels of hydroxide ions (OH^-) in the seed solutions, the neutral zinc hydroxide particles ($Zn(OH)_2$) do not interact with sodium cations (Na^+) as they adsorb to the substrate, and all sodium cations (Na^+) are washed away. Thus, zinc hydroxide ($Zn(OH)_2$) particles on the surface produce ZnO nanocrystalline seeds upon annealing with the c-axis alignment normal to the substrate; this leads to vertically aligned nanowires. On the other hand, high levels of OH^- concentrations lead to zincate ions ($Zn(OH)_4^{2-}$) in the seed solution. As these ions adsorb on the surface, they must combine with the available cations to maintain their charge neutrality as the solution dries on the surface of the substrate. This leads to formation of sodium zincate ($Na_2Zn(OH)_4$)

particles on the surface, which, upon annealing, lead to ZnO seeds with a substantial amount of Na impurities incorporated into them. The crystal orientation of the ZnO seeds is randomized in this process, leading to misaligned nanowires after the growth process.

3.3.5 Summary

Through this study, we have successfully synthesized vertically aligned ZnO nanowires on amorphous substrates by using seed crystals grown from a mixture of ammonium hydroxide (NH_4OH) and zinc acetate ($Zn(O_2CCH_3)_2$. We also have provided an explanation of the mechanism involved in the creation of misaligned nanocrystalline seeds arising from incorporation of metallic (Na or K) impurities when the seed solution contains high OH^- concentrations. The seed orientations studied by TEM indicate that NH_4OH-derived seeds lead to c-axis alignment normal to the substrate. From these studies, we conclude that (1) pure ZnO nanocrystals prefer to orient on a flat substrate with their c-axis perpendicular to the surface, and (2) impurities incorporated into the ZnO seed crystals at high NaOH (or KOH) concentrations destroy the preferred orientation of the nanocrystal seeds and result in the growth of misaligned nanowires. This advance in understanding of how to control the growth orientation of nanowires makes it possible to grow ZnO nanostructures through a process compatible with widely used Si fabrication technology.

4. ZnO Sea Urchin Structures: Synthesis, Material Characterization and Growth Mechanism

In this chapter, I will introduce the synthesis and growth mechanism of ZnO sea urchin-like structures. The ZnO sea urchin-like structures are composed of a core containing a mixture of Zn_3P_2 and ZnO phase, of composition: ZnO_xP_y, encased in ZnO shell layers on which ZnO nanowires are grown. Based on material characterization and control experiments, we propose a novel synthetic method and growth mechanism that leads to the formation of ZnO sea urchin-like structures.

4.1 Introduction to the Sea Urchin Composed of 1D Nanowires with 3D Sphere

Rational synthesis and assembly are key for the exploitation of quasi one-dimensional (1-D) nanostructures as either building blocks or interconnecting units for integrated nanodevices on a chip[110,111]. The progress of nanotechnology through a bottom-up approach is hinged on the constant accumulation of facile methodology to synthesize 1-D nanostructures with specific morphologies, compositions and heterostructures[112,113].

Various well known architectures of ZnO nanostructures have previously been synthesized, studied, and exploited for their unique optoelectronic properties. ZnO structures such as nanowires and nanoparticles have been successfully used to improve devices like electrical generators[114-116], nanolasers[91], phosphors[117,118], light-emitting diodes[20,46], and biosensors[119]. The polar wurtzitic lattice structure of ZnO crystals leads to discriminatory growth only along certain facets. This behavior is responsible for the variety of morphologies possible with ZnO.

Recently, substantial efforts to integrate 1-D nanostructures into 3-D microstructures resulted in urchin-like zinc oxide (ZnO) superstructures, hereafter termed ZnO sea urchins[120-124]. ZnO sea urchin is a micro-sized architecture in which a core spherical structure is the growth base for an array of nanowires. Compared with their 3-D bulk counterparts, the sea urchins have unique advantages in their high density, porosity, large surface area, and increased photosensitivity due to the high surface-to-volume ratio of the 1-D supplements[120]. Such structures offer an increase in effective surface area of the nanowire array when compared to a planar configuration. For example, devices such as dye-sensitized solar cells (DSSCs) made using ZnO sea urchins have shown higher power conversion efficiency than that of simple nanowires array[125]. The success of these devices are due in large part to the superior density of the nanowire arrays owing to the three dimensional base morphology which allows for a more efficient use of substrate surface area. The facile synthesis of these structures has therefore been the subject of great interest and research.

To synthesize ZnO sea urchins, previous attempts prepared micro-scaled spheres as the template to grow nanowires using either a solution-based method or a chemical vapor transport technique[120,122]. In these cases, the chemical coating or deposition of the spherical template made the synthetic processes complicated and inefficient. Skipping the preparation of a spherical template and instead using simple evaporation of zinc powder has disadvantages including low-crystalline quality and incomplete morphologies of the sea urchins, termed as microbowls.

In this study, we report on the novel facile synthesis of ZnO sea urchins made using a chemical vapor transport method in which Zn_3P_2 powder is added to ZnO and graphite (C) powders. Scanning electron microscopy (SEM) reveals that highly-dense and uniform ZnO nanowires are grown on the surfaces of microspheres. X-ray diffraction (XRD) patterns indicate that these materials are mainly composed of ZnO. The lattice-resolved images and electron diffraction patterns using high-resolution transmission electron microscopy (HRTEM) show that the outer nanowires on the sea urchins are ZnO grown from the c-axis of wurtzite structure. The mapping images using energy-dispersive x-ray spectroscopy (EDS) in HRTEM indicate that the surfaces of the microspheres are composed of a ZnO layer as a result of oxidation. However, a control experiment, in which the as-grown sea urchins, bare microspheres, and microbowls were annealed, indicates that the core region of the sea urchin and bare microspheres are composed of Zn_3P_2 and ZnO in a mixture phase in the form of ZnO_xP_y, whereas microbowls are completely composed of pure a ZnO shell. Based on material characterization and control experiments, we suggest the growth mechanism of ZnO sea urchins obtained using novel synthetic method.

4.2 Facile Method Using Applied Carbonthermal Reduction Process for the Synthesis of ZnO Sea Urchins

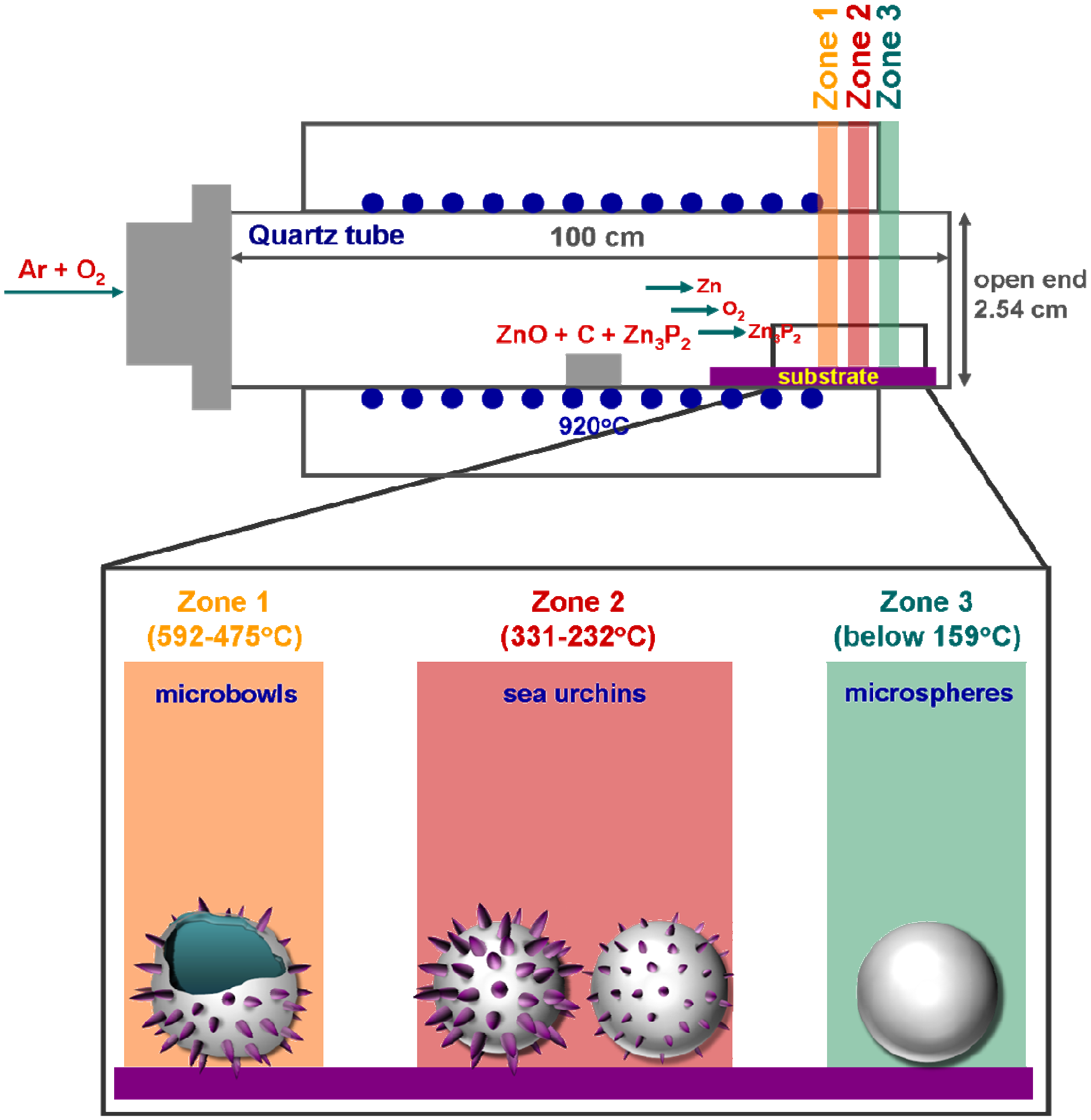

Figure 4.1: A schematic illustrating the growth process producing ZnO sea urchins. Zone 1, Zone 2 and Zone 3 are approximately labeled based on both the temperature measurement results in the tube furnace as shown in Figure 4.2 and the as-synthesized morphologies; Zone 1 (592-475°C) including microbowls, Zone 2 (331-232°C) including sea urchins and Zone 3 (below 159°C) including microspheres.

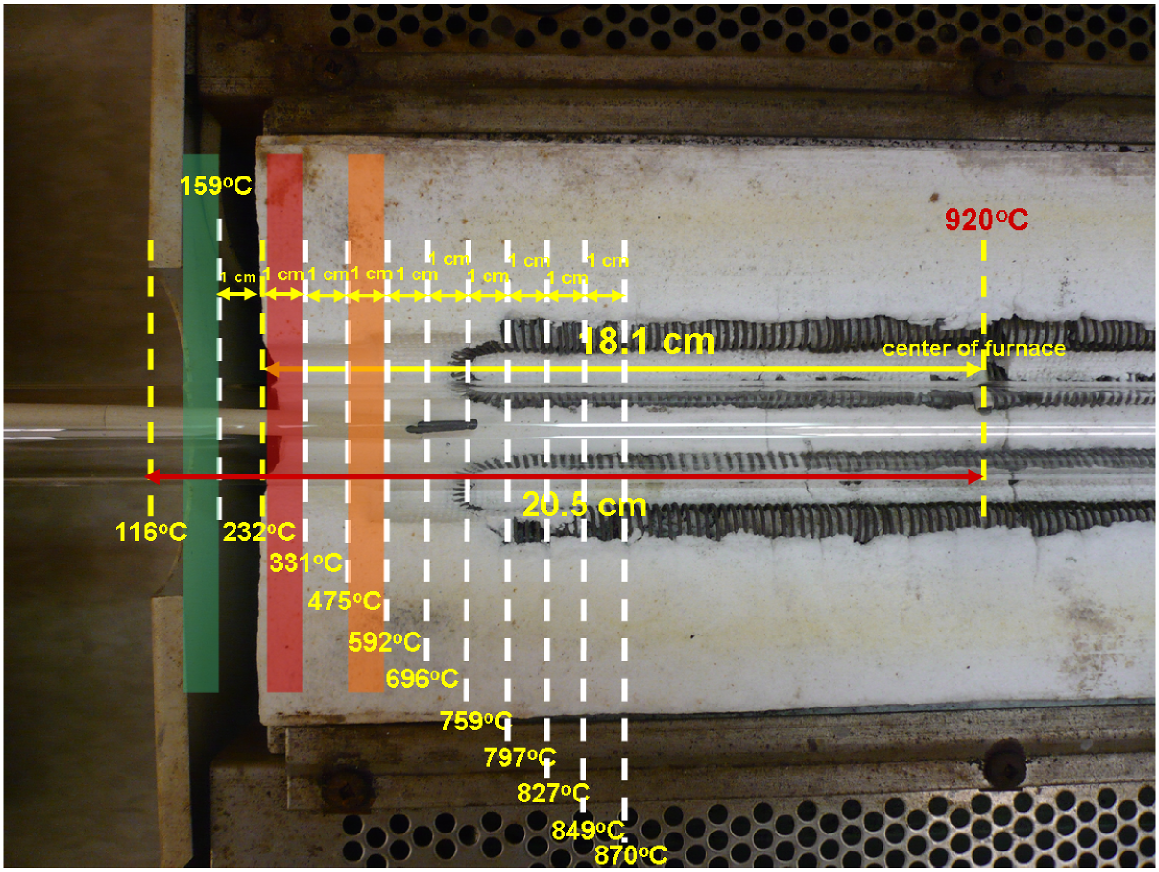

Figure 4.2: A photo of the tube furnace with local temperatures at each spot from the end of the insulator at increments of 1 cm distance when the center of the furnace is 920°C

Figure 4.1 shows a schematic of our chemical vapor transport (CVT) system used to synthesize ZnO sea urchins and other structures. Ground ZnO, graphite (C) and Zn_3P_2 were used as source materials and positioned in the middle of a tube furnace. While source materials evaporated at the central furnace temperature of 920°C, a silicon substrate located downstream in the quartz tube experienced a temperature gradient in which the temperature was lower than the central furnace temperature by a magnitude related to the distance from the center of the furnace. The varying temperatures along the longitudinal dimension of the tube when the input central temperature was set at 920^{o}C were carefully measured using a thermometer. Although it was difficult to segregate unambiguous boundaries on local temperatures, we categorized temperature zones as three main sections depicted in Figure 4.1 on the basis of the as-synthesized morphological differences.

Between certain zones, as shown in Figure 4.2, there are sharp temperature changes near the end of the heating elements in the furnace (between Zone 1 and Zone 2) and the end of the thermal insulating component of the tube furnace (between Zone 2 and Zone 3).

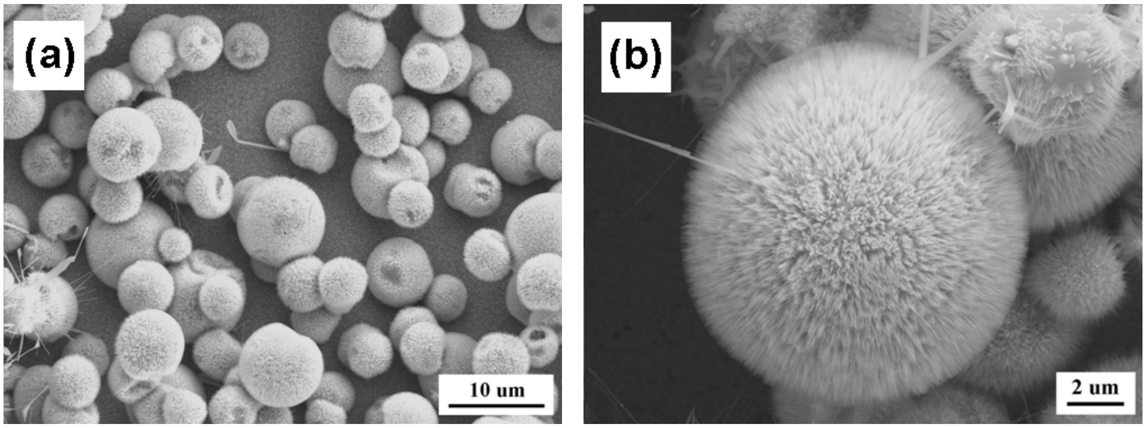

Figure 4.3: SEM images of ZnO sea urchins synthesized using ZnO (0.6 (g)), graphite (C) (0.6 (g)) and Zn_3P_2 (0.2 (g)) in Zone 2. (a) Low-magnification of SEM image of stacked sea urchins. (b) high-magnification of SEM image of a sea urchin from Figure 4.3 (a).

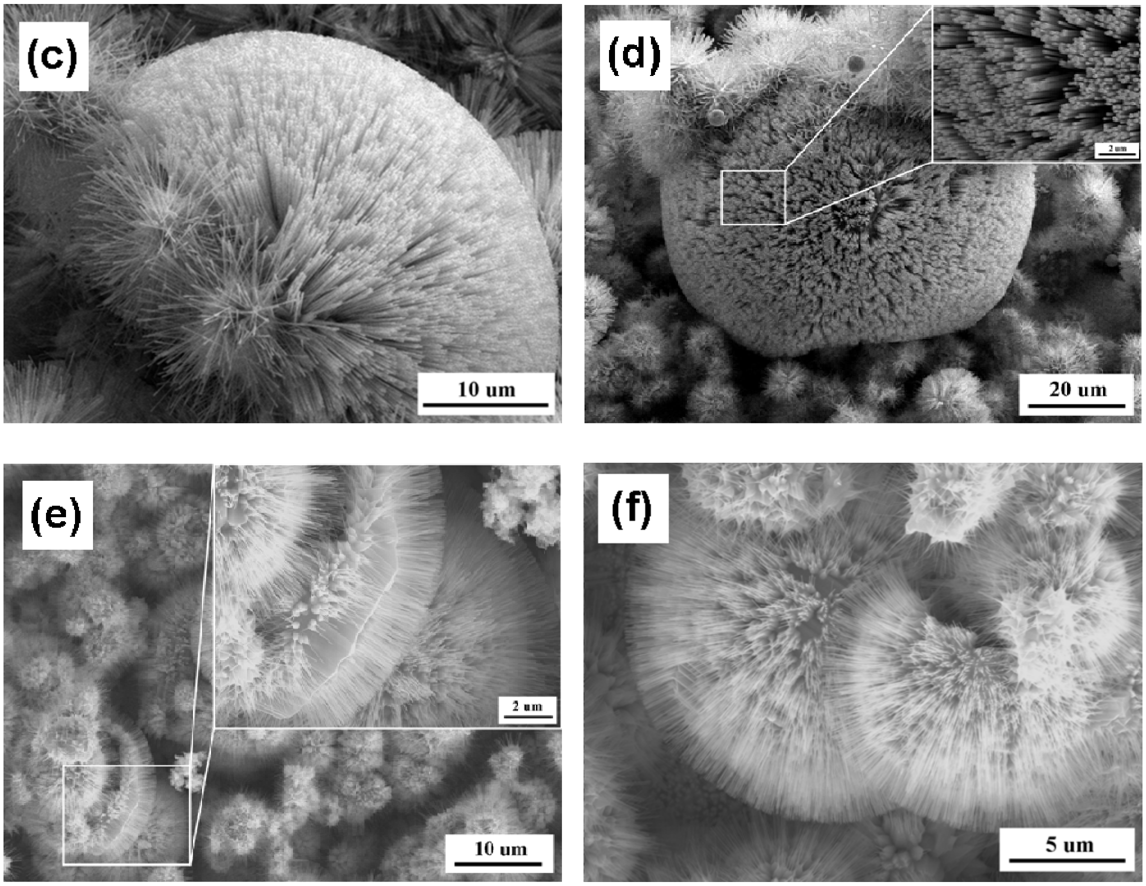

Figure 4.3: SEM images of ZnO sea urchins synthesized using ZnO (0.6 (g)), graphite (C) (0.6 (g)) and Zn_3P_2 (0.2 (g)) in Zone 2. (c) High-magnification of SEM image of a sea urchin of 40 um diameter. (d) Low-magnification of SEM image of a sea-urchin of 60 um diameter treading on stacked sea urchins. The inset shows highly dense as-grown ZnO nanowires on microspheres. (e) A broken sea urchin among complete sea urchins. The inset shows the cross-sectional image. (f) High-magnification of SEM image of complete sea urchins from Figure 4.3 (e).

Figure 4.3 shows SEM images of as-grown ZnO sea urchins generated in the ranges of 232-331^{o}C in zone 2 in Figure 4.1. Densely stacked micro-scaled sea-urchins entirely cover the substrate at these temperature ranges as shown in Figure 4.3 (a), (d) and (e). A sea urchin is comprised of uniformly ordered arrays of outer ZnO nanowires grown on the surfaces of inner microspheres as shown in Figure 4.3 (b)-(f). SEM images reveal that the diameter of microspheres are in the ranges of 5-20 um or sometimes up to ~60 um as shown in Figure 4.3 (c) and (d). The cross-sectional SEM image shown in Figure 4.3 (e) reveals the lengths of nanowires are in the ranges of 2-3 um.

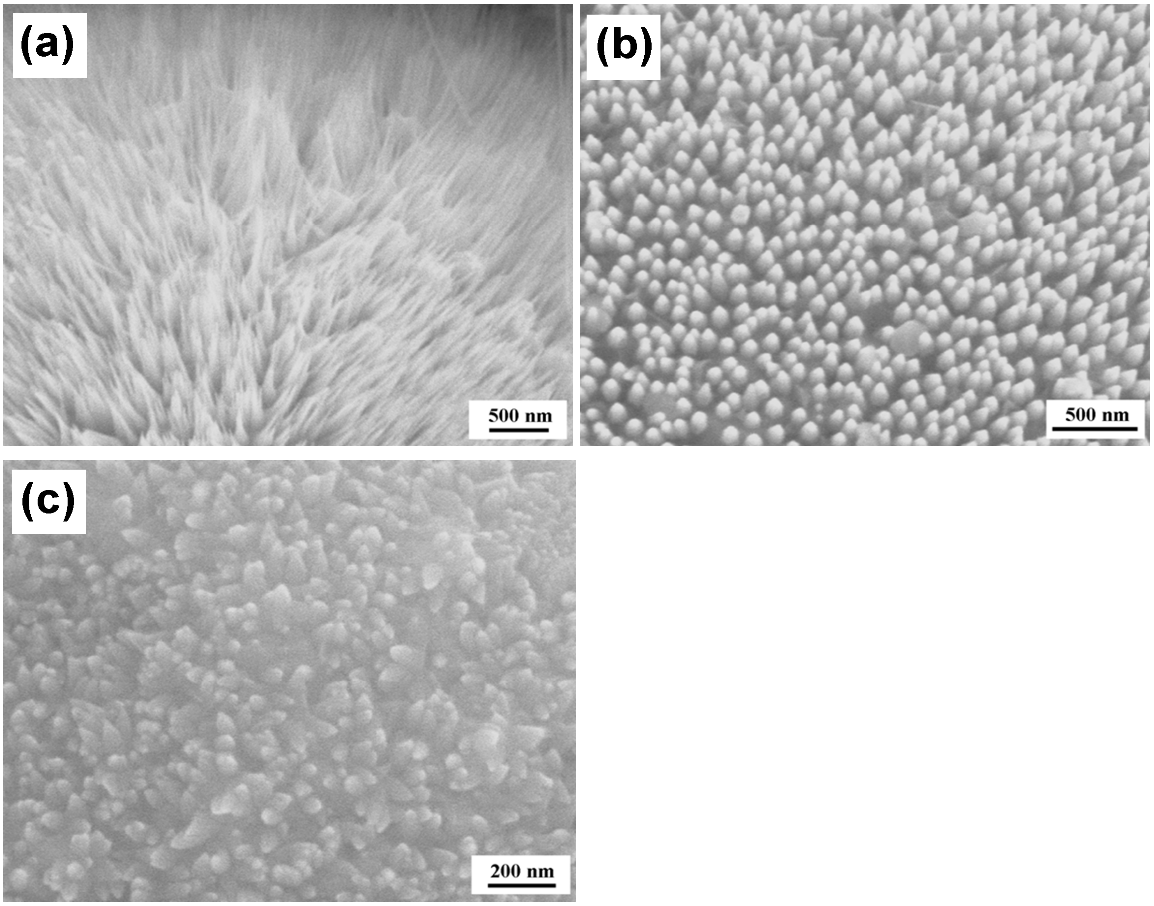

Figure 4.4: SEM images of gradually decreasing nanowire length in the region from Zone 2 to Zone 3 as local temperature decreases

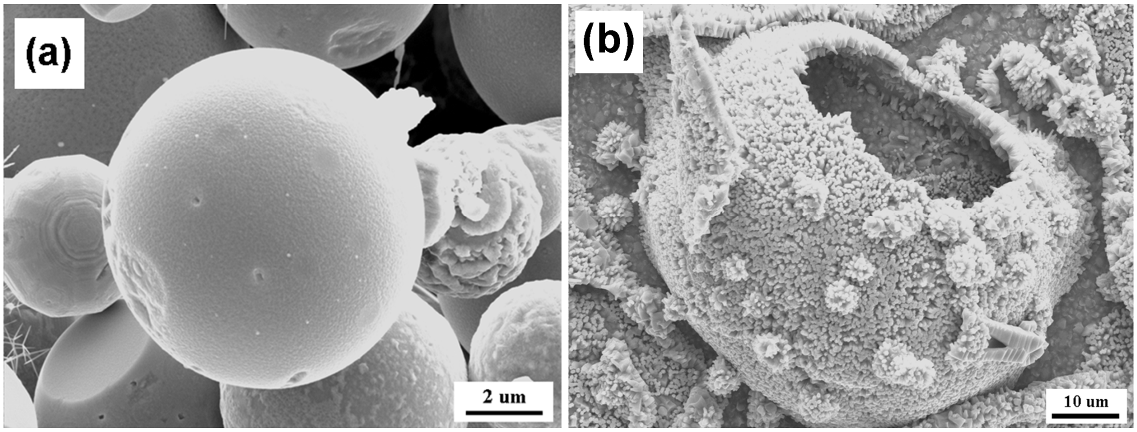

Figure4.5: SEM images of (a) microspheres grown in Zone 3 and (b) microbowls grown in Zone 1.

Sea urchins with long ZnO nanowires as shown in Figure 4.3 were only observed in Zone 2, whereas bare microspheres as shown in Figure 4.5 (a) are observed in Zone 3. From Zone 2 to Zone 3, sea urchins were formed with nanowires whose lengths were gradually decreasing as local temperature decreased as shown in Figure 4.4 (a)-(c). Figure 4.5 (b) show SEM images of bowl-like structures (hereafter termed as microbowls) observed in Zone 1 depicted in Figure 4.1. Detailed mechanism for the formation of these different structures will be discussed in section 4.4.

4.3 Analysis of Material Properties of ZnO Sea Urchins

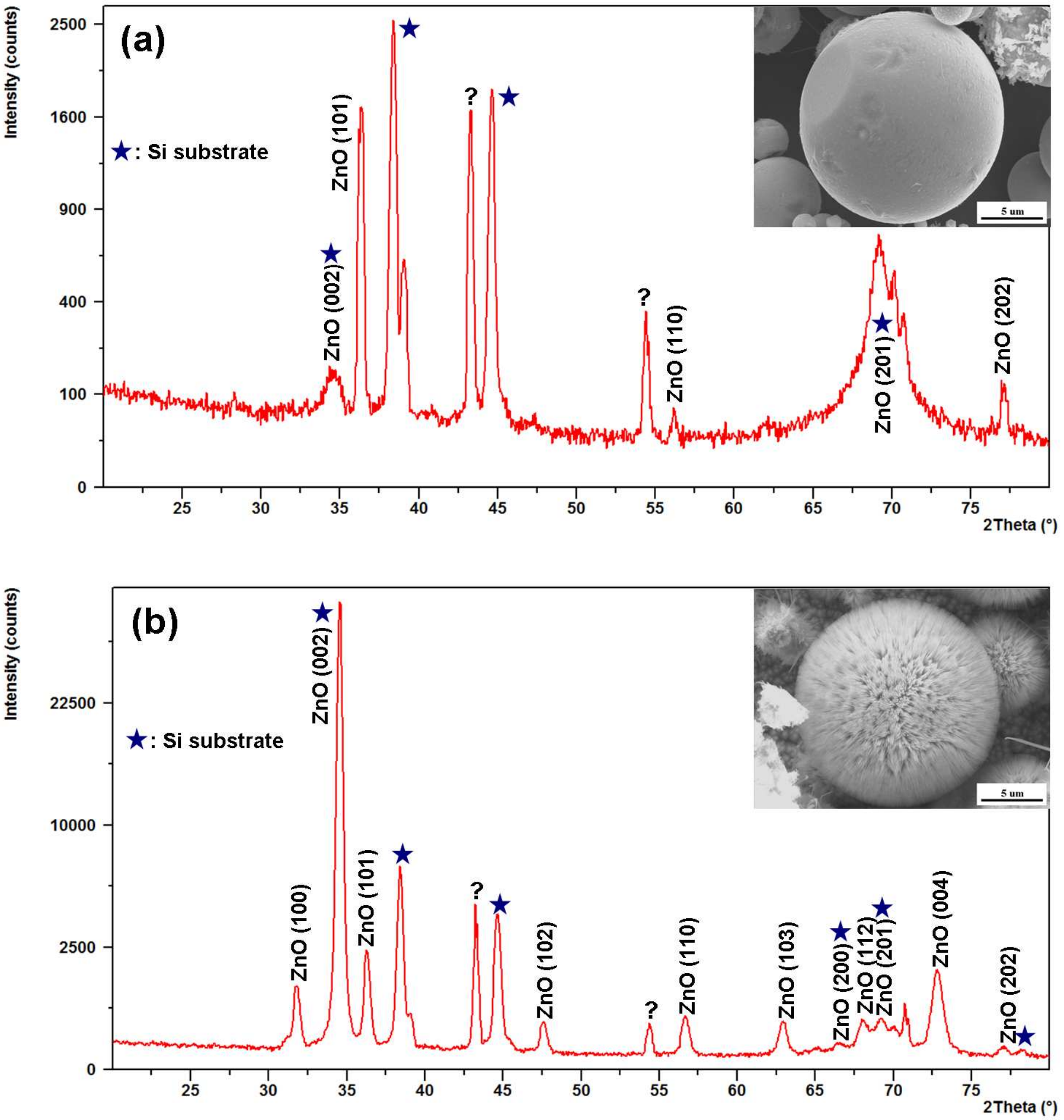

Figure 4.6: X-ray diffraction (XRD) patterns of (a) microspheres measured in Zone 3 and (b) sea urchins measured in Zone 2. The inset in (a) shows a SEM image of as-prepared microsphere used for this XRD measurement; the inset (b) shows a SEM image of the as-prepared sea urchins used for this XRD measurements.

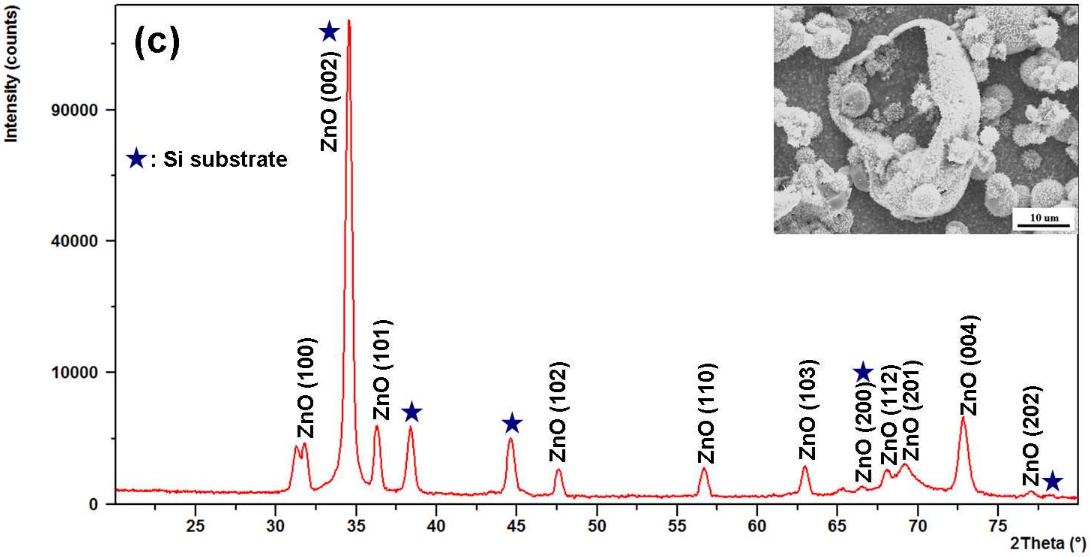

Figure 4.6: X-ray diffraction (XRD) patterns of (c) microbowls in Zone 1. The inset (c) shows a SEM image of the as-prepared microbowls used for this XRD.

X-ray diffraction (XRD) measurements reveal that sea urchins are mainly composed of ZnO. XRD measurements were respectively performed on microspheres (an inset in Figure 4.6 (a)) grown in Zone 3, sea urchins (an inset in Figure 4.6 (b)) grown in Zone 2 and microbowls (an inset in Figure 4.6 (c)) grown in Zone 1. As can be seen in Figure 4.6 (a), as-grown microspheres present distinct ZnO peaks at (101), (110) and (202) which do not overlap with silicon substrate peaks. As microspheres are transformed to sea urchins, various ZnO peaks with increasing intensity are able to be detected along with the aforementioned distinct ZnO peaks as with the pristine microspheres in the XRD patterns shown in Figure 4.6 (b). Additional measurements of XRD patterns of microbowls grown in Zone 1 show that these structures are also completely composed of ZnO as shown in Figure 4.6 (c). The question marks at 43 and 54 degree in the x-ray diffraction angle shown in Figure 4.6 (a)-(b) overlap with the (322) and (216) peaks in Zn_3P_2, respectively. However, since no other distinct Zn_3P_2 peaks were observed, especially below 30 degrees, we cannot conclude that these two peaks indicate the existence of pure Zn_3P_2 phases in the structures. As will be shown in later sections 4.4, the existence of low melting point components was observed by annealing the products in air to 700°C. Thus, it is possible that a mixed ZnO and Zn_3P_2 phase (labeled as ZnO_xP_y) could be present in the core of the structures. The composition of this mixed phase and its existence is a function of the local temperature under which the structures are formed. At the high temperature region, no Zn_3P_2 existed due to evaporation, at the low temperature region, more of the Zn_3P_2 phase survived.

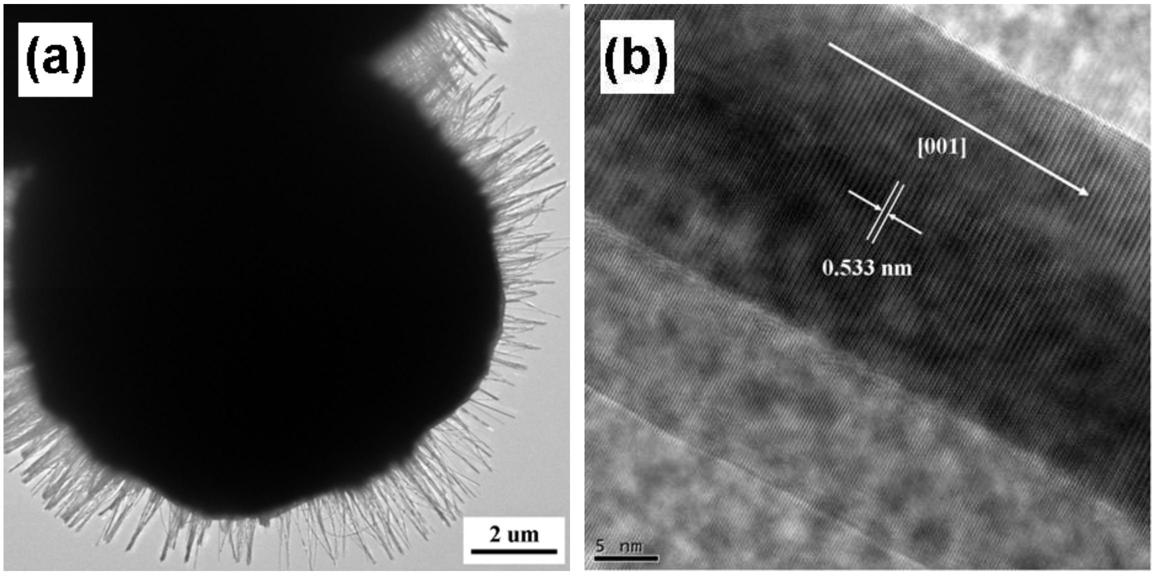

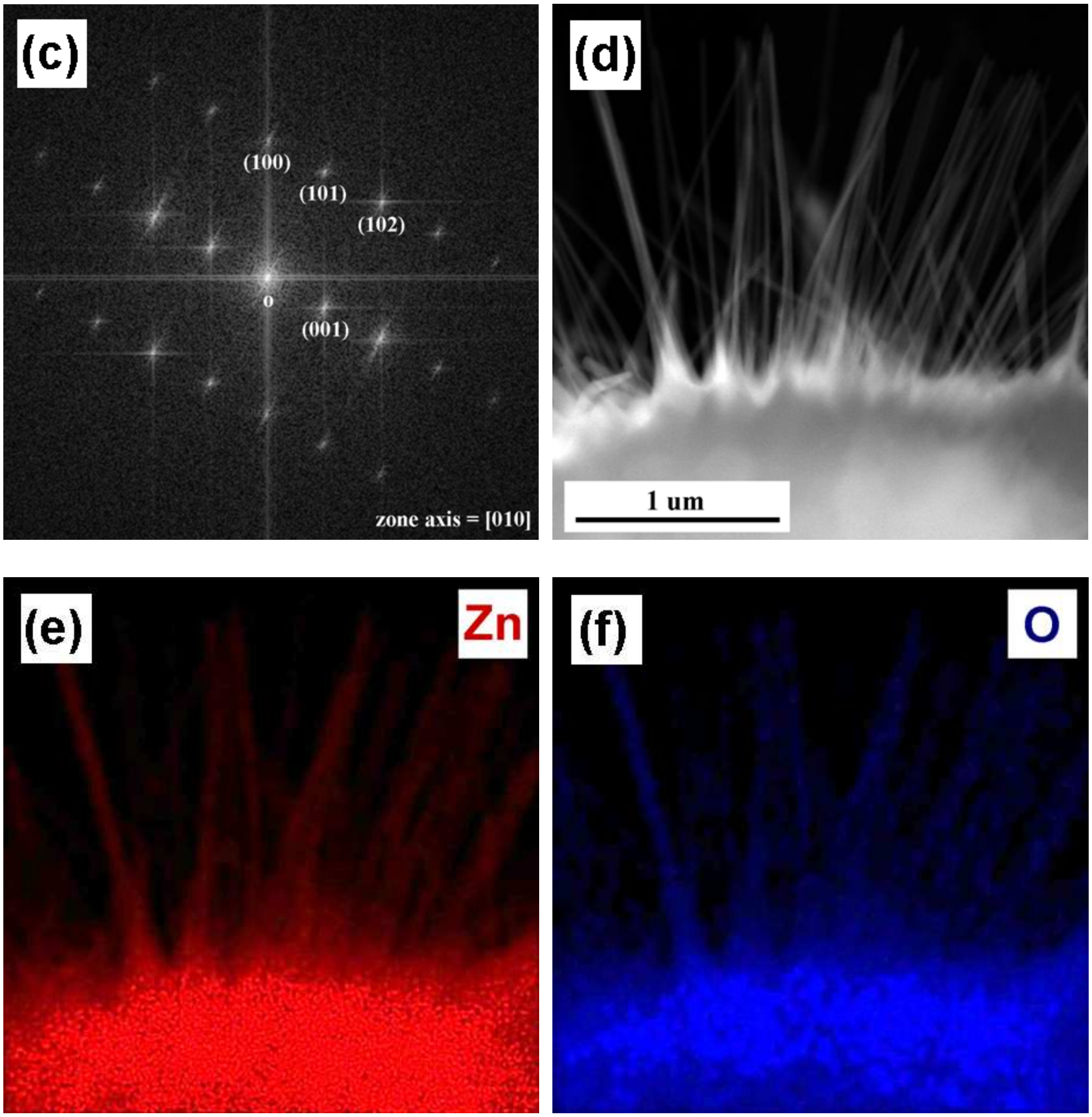

Figure 4.7: (a) Low-magnification of TEM image of a ZnO sea urchin (b) Lattice-resolved image of nanowire outer structure of a sea urchin using HRTEM (c) SAED image from Figure 4.7 (b), (d) Low-magnification HRTEM image focusing the boundary region of a ZnO sea urchin for the EDS mapping, (e) EDS mapping image showing Zn (represented by red) detection from the spot of Figure 4.7 (d), (f) EDS mapping image showing O (represented by blue) detection from the spot of Figure 4.7 (d)

Table 4.1: The quantitative constituents detected on the surface of inner microsphere in a sea urchin using EDS from Figure 4.7 (d).

Element	Zinc (Zn)	Oxygen (O)	Carbon (C)	Phosphorous (P)
Normalized wt.%	93.39	6.61	0	0
Normalized at.%	77.56	22.44	0	0

Table 4.2: The quantitative constituents detected on the outer nanowires in a sea urchin using EDS from Figure 4.7 (d). Carbon component originates from TEM carbon membrane grid.

Element	Zinc (Zn)	Oxygen (O)	Carbon (C)	Phosphorous (P)
Normalized wt.%	70.61	10.52	18.87	0
Normalized at.%	32.64	19.88	47.48	0

To investigate the constituents and likelihood of miscibility between ZnO and Zn_3P_2 in the sea urchins, lattice-resolved images, selected area electron diffraction (SAED) patterns and energy-dispersive x-ray spectroscopy (EDS) mapping images on both outer nanowire and inner microsphere were analyzed using high-resolution transmission electron microscopy (HRTEM). As can be seen in Figure 4.7 (a), it was not possible to analyze the delicate lattice structure on the inner part of sea urchin using TEM due to its bulky size. ZnO has a lattice constant of ~5.2 Å for the gap from top to bottom basal c-planes in its wurtzite crystal structure[33]. Thus, the lattice spacing of ~5.3 Å shown in Figure 4.7 (b) and SAED pattern shown in Figure 4.7 (c) confirm that nanowires are only composed of single-crystalline ZnO grown along c-axis [001] in its wurtzite crystal structure. As shown in Figure 4.7 (d), (e), (f), Table 4.1 and 4.2, the mapping images and quantitative analyses using EDS also verify the constituents of outer nanowires as Zn and O. In Table 4.2, the carbon (C) originates from TEM carbon membrane grid. However, the phosphorus signal from the inner microsphere was not detected by the EDS. Based on the quantitative analysis using EDS, we attribute detecting Zn and O without P in the sea urchin to the surface oxidation of the inner microsphere during the condensation of source vapors prior to growing ZnO nanowires.

4.4 Growth Mechanism of ZnO Sea Urchin Structures

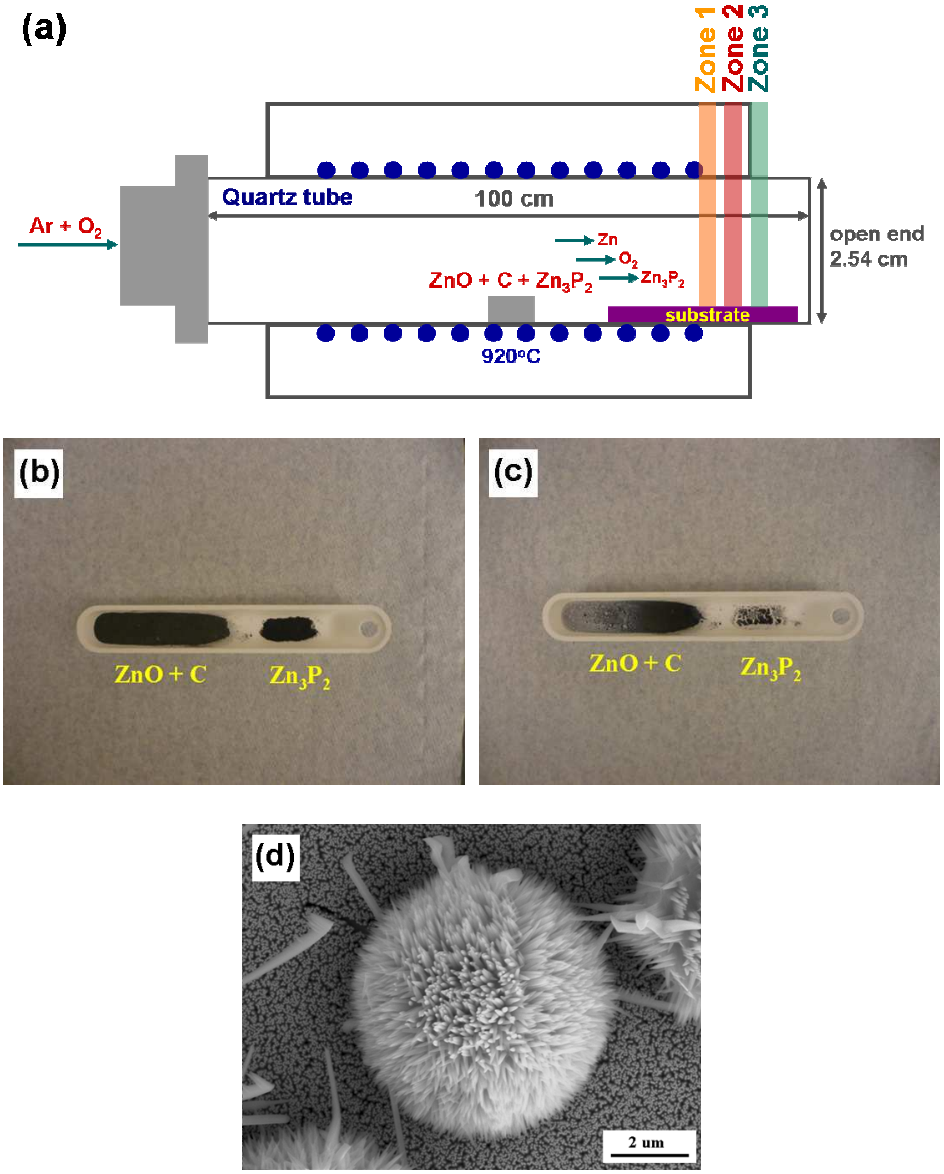

Figure 4.8: (a) A schematic illustrating the source powders in which ground ZnO and C are separated from Zn_3P_2 (b) A photo image of the separation of source materials before the growth process (c) A photo image of separation of source materials after the growth process (d) A SEM image of as-synthesized ZnO sea urchin using source powder separation.

As shown earlier, various structures were observed in different temperature zones in our experiments. In order to understand the growth mechanism we need to take a close look at the evolution of the temperature and the concentration of the various precursors. Looking at the growth mechanism of ZnO nanowires using a vapor-liquid-solid (VLS) process, ground ZnO and C powder have generally been used as source materials. This carbon-thermal reduction happens at 900-1300°C[32];

$$ZnO(s)+C(s)\text{->}Zn(v)+CO(v)$$

In our experiments, we also routinely obtained vertically aligned ZnO nanowires on the substrate coated with ZnO nanocrystal seeds when we intentionally omit Zn_3P_2 powder in the source materials. It is known that Zn_3P_2 could decompose into Zn and P vapors at 600-850°C as follows[126];

$$Zn_3P_2(s) \text{->} 3Zn(v) + 1/2P_4(v)$$

Thus, evaporation of Zn_3P_2 at 420-920°C, which produces Zn_3P_2 as well as Zn and P vapors, directly involved in the creation of the microsphere in the sea urchin structure. To clearly understand the chemical reactions between source materials, we separated Zn_3P_2 from the source materials on a boat during the growth process as shown in Figure 4.8 (a). Figure 4.8 (b) shows a photo image of the sources separated before the growth process, whereas Figure 4.8 (c) shows a photo image after the growth process. As can be seen in Figure 4.8 (c), Zn_3P_2 powder completely evaporated after the growth process since its melting point is 420°C and there is a possibility that the Zn_3P_2 could decompose between 600-850°C. Figure 4.8 (d) shows the as-grown ZnO sea urchin using these source materials separated, equivalent to the sea urchins generated using the mixture of three powders. This result and the as-mentioned carbonthermal reduction indicate that C only reduces ZnO powder, while Zn_3P_2 is exclusively evaporated or decomposed.

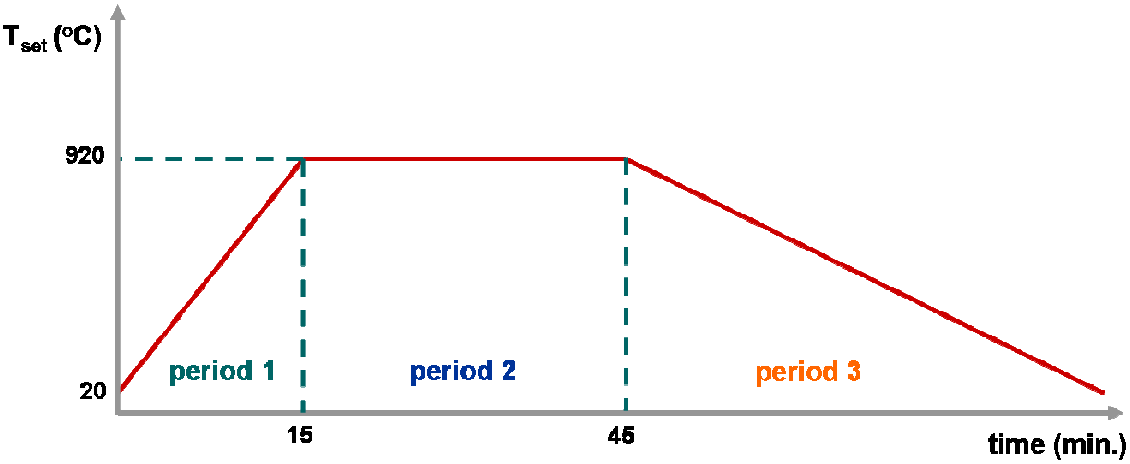

Figure 4.9: Temperature profile of the central furnace during the growth process.

Table 4.3: Morphology and phase variations in each zone at a given growth period as shown in Figure 4.9

	period 1 (20 ➡ 920°C)	period 2 (920°C)	period 3 (920 ➡ 20°C)
Zone 1	microspheres (condensation) (oxidation as temperature increases)	microbowls (incomplete evaporation) (nanowire growth)	microbowls
Zone 2	microspheres (condensation) (oxidation as temperature increases)	sea urchins (no evaporation) (nanowire growth)	sea urchins
Zone 3	microspheres (condensation) (oxidation as temperature increases)	microspheres (no evaporation) (oxidation)	microspheres

Based on the result as shown in Figure 4.8, we propose a condensation process of source vapors and subsequent morphology variations in the different temperature regions. In terms of time domain, we can separate the whole growth process into three different periods as shown in Figure 4.9. Period 1 is the heating of the furnace from room temperature to 920°C. During this period, Zn_3P_2 exclusively starts to evaporate or decompose as the temperature increases beyond its melting point of 420°C. As this vapor transport along the tube, it lands and then condenses[121] into microspheres in Zones 1, 2 and 3 due to the temperature gradient as shown in Table 4.3. Furthermore, the supplied O_2 quickly oxidizes the exposed surface of the microspheres, leading to the formation of ZnO_xP_y microspheres. During Period 2, in which the central furnace temperature reach to and then is maintained at the highest of 920°C, the local temperatures at Zones 1, 2 and 3 also reach and is subsequently maintained at their highest temperatures for 30 min, respectively. Temperature in Zone 1 is around 590-470°C which exceeds the melting point of Zn_3P_2 which causes the deposited microspheres to experience incomplete evaporation leaving behind an oxidized ZnO shell[122]. These shells of ZnO will serve as nucleation sites for the growth of ZnO nanowires forming structures, hereby termed as microbowls (Figure 4.5 (b)). During period 2, the carbon-thermal reduction between ZnO and C takes place and then converts source powders into Zn and CO vapors. As these vapors are transported into each zone experiencing temperature gradient, they condense in Zone 1 as nanowires on the open ZnO shells to form microbowls. In Zone 2, the reaction of Zn and O_2 vapors on the ZnO surface of microspheres leads to the growth of ZnO nanowires array producing sea urchin structures. However, since the proper temperature is particularly essential for the growth speed of ZnO nanowires, sea urchins with long nanowires are only formed in specific regions. Due to the sensitivity of nanowire growth to temperature, nanowires arrays with decreased length are observed on sea urchins located further downstream in Zone 2. When the source vapors reach Zone 3, the local temperature is no longer sufficient to sustain nanowire growth so that microspheres are only observed in Zone 3. During period 3, wherein the central furnace temperature is cooled down to room temperature, source vapors may still grow small amounts of nanowires in Zone 1 as the temperature decreases into a range favorable for nanowire growth. This proposed mechanism is summarized in Table 4.3.

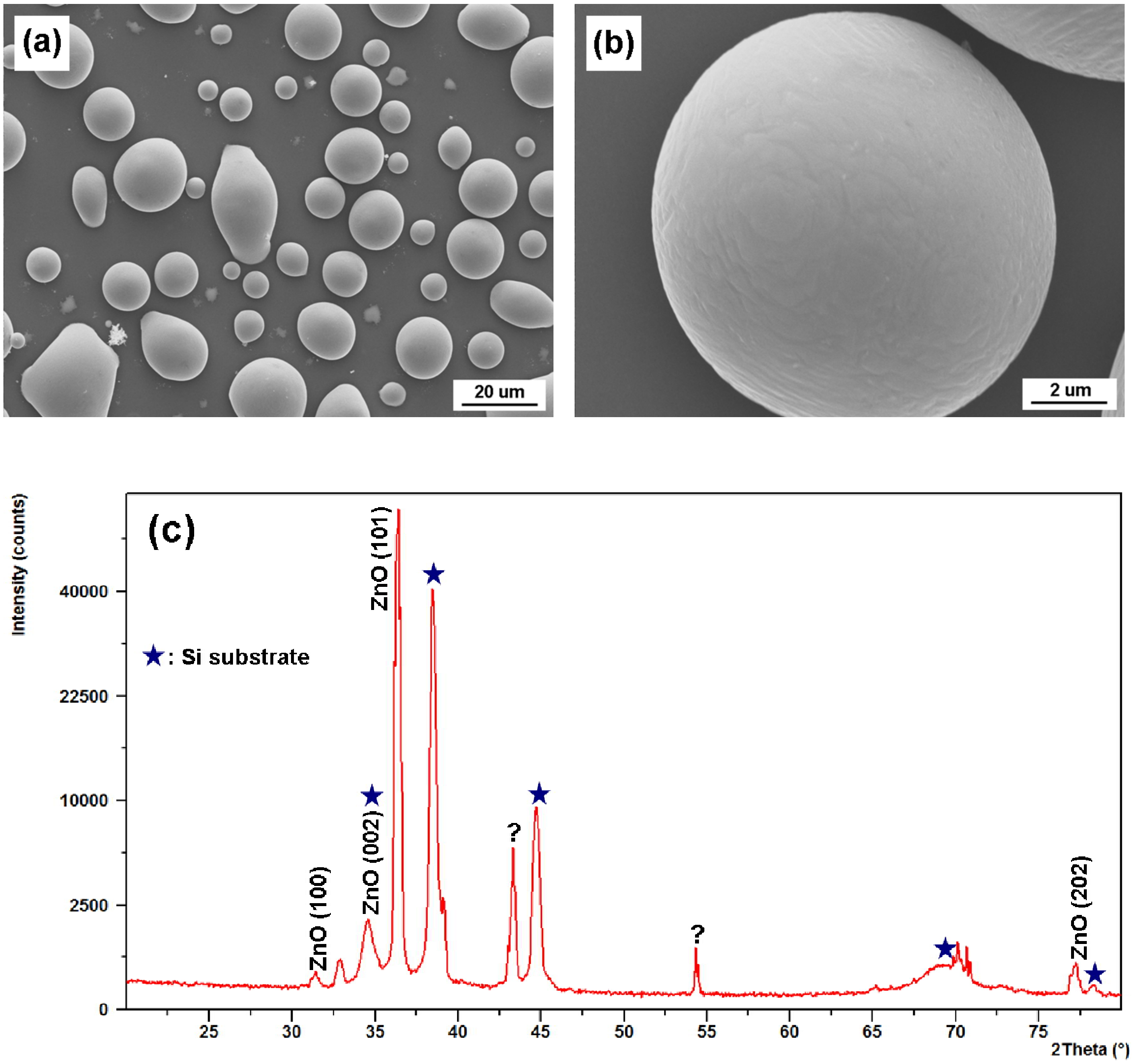

Figure 4.10: (a) A low-magnification SEM image of microspheres on the sample taken at 700°C during the heat ramping to reach 920°C. (b) A high-magnification SEM image of microsphere from Figure 4.10 (a). (c) XRD patterns of the microspheres as shown in 4.10 (a)-(b).

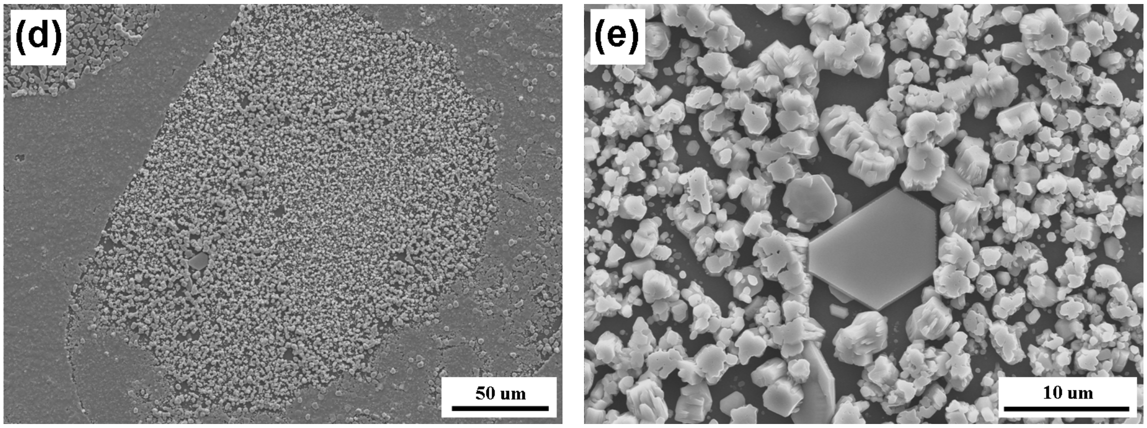

Figure 4.10: (d) A low-magnification SEM image of traces of evaporated microspheres in the higher temperature regions than Zone 1 (592-475°C). (e) A high-magnification SEM image of ZnO nanoplates generated in the trace of evaporated microsphere in Figure 4.10 (d).

To confirm the condensation and oxidation process from source vapors, which initially form liquid droplets and then solidify into microspheres which are subsequently oxidized, we investigated samples taken from the tube furnace when samples are in period 1 as shown in Figure 4.9. The SEM images of a sample taken at 700°C as shown in Figure 4.10 (a)-(b) show that condensation of source vapors occurs in period 1 as described in Figure 4.9 and table 4.3. XRD patterns of microspheres in this sample, shown in Figure 4.10 (c) suggest that ZnO layers may grow on the surface of the growing microspheres as a result of an oxidation process and serve as a self catalyst for the growth of the outer ZnO nanowires in the ZnO sea urchins. After a growth process of 30 min at 920°C central furnace temperature, regions with higher local temperatures than zone, experiencing a temperature above 700°C, had traces of evaporated microspheres (complete evaporation in period 2) leaving behind ZnO plate-like structures, termed as nanoplates, as shown in Figure 4.10 (d)-(e).

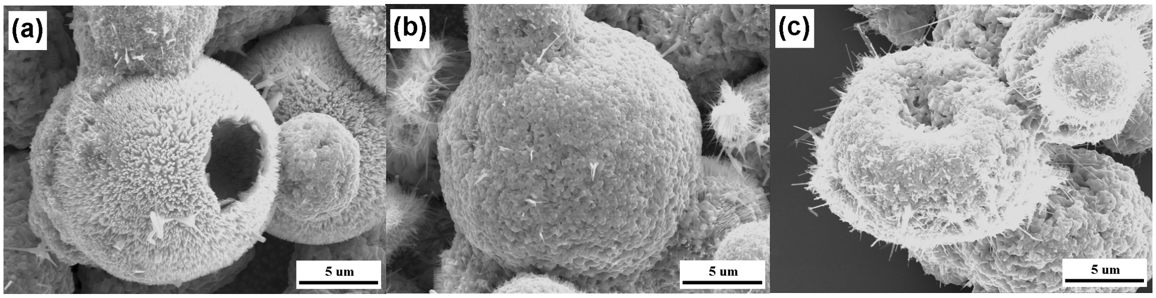

Figure 4.11: SEM images of (a) intact microbowls observed in Zone 1, (b) melted and aggregated sea urchins observed in Zone 2 and (c) melted microsphere with new nanowires due to the oxidation observed in Zone 3 after the annealing at 700°C for 30 min in air.

In a control experiment, the annealing of a sample at 700°C for 30 min in air, plainly shows that the core region of the sea urchin and microsphere are composed of a mixed ZnO and Zn_3P_2 phase (labeled as ZnO_xP_y) which could not be identified in the XRD and EDS. As shown in Figure 4.11 (a), an SEM image of intact microbowls observed in Zone 1 after the annealing process verifies that microbowls are only composed of pure ZnO when we consider the melting point of ZnO (1975°C). As shown in Figure 4.11 (b)-(c), the SEM images of sea urchins observed in Zone 2 and microspheres observed in Zone 3 show that these are melted and shrunken during the annealing at 700°C due to the evaporation of ZnO_xP_y compositions. Provided the surface of sea urchins and microspheres are composed of the ZnO layer based on EDS measurements, melted structures indicate that core regions in these structures are composed of the ZnO_xP_y, which probably has a lower melting point than that of pure ZnO. The composition of this mixed phase and its existence are a function of the local temperature under which the structures are formed. At high temperature regions, no Zn_3P_2 phase existed due to complete evaporation, at low temperature regions, more Zn_3P_2 phase is observed.

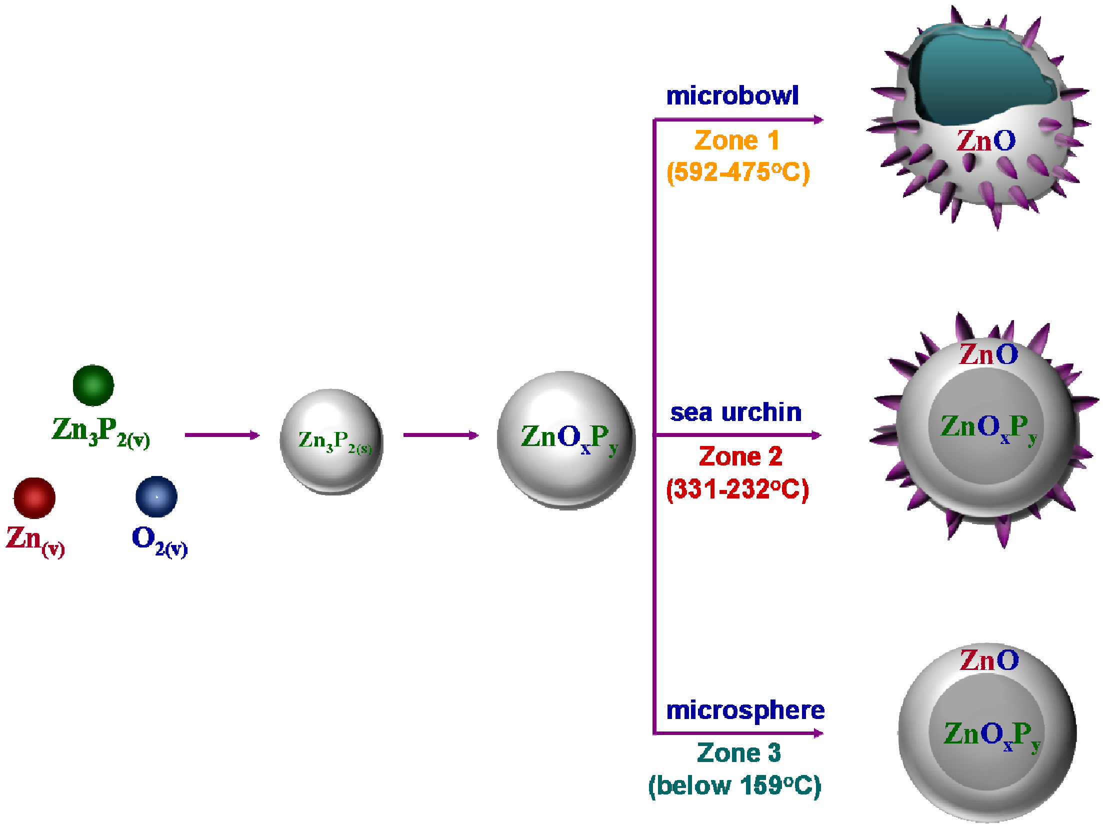

Figure 4.12: A schematic illustrating the growth mechanism of ZnO sea urchins.

Based on both previous reports[121,127,128] and our experimental results shown in Figure 4.9-4.11 and table 4.3, we suggest the growth mechanism of ZnO sea urchin structures as shown in Figure 4.12. During the heating process, the Zn_3P_2 vapors transported by Ar carrying gas from source materials land on the substrate in zone 1, 2 and 3 to form Zn_3P_2 liquid droplets. During and after this condensation process, condensed droplets are oxidized by supplied or already present O_2 in the tube, leading to the formation of the ZnO_xP_y mixed phase. Further oxidation, depending on the temperature and concentration of oxygen, can convert the surface layer of the sphere to pure ZnO, forming a shell. When considering the melting point of pure Zn_3P_2 at 420^oC, in the case of microbowls, ZnO_xP_y in the core region could present an increasing vapor pressure as local temperature increases during period 1 in Zone 1. When local temperature increases beyond ZnO_xP_y's melting point during the period 1, evaporation from core region makes a hole at the surface of ZnO layer in order for ZnO_xP_y to evaporate leading to the hollow ZnO bowl-like frame. Adsorptions of Zn and O_2 vapor to the surface of this ZnO bowl-like frame produce the nanowires leading to the microbowls made of pure ZnO as shown in Figure 4.5 (b) and Figure 4.11 (a). In the case of sea urchins in Zone 2 and microspheres in Zone 3, the sphere structures are maintained without evaporation since the highest local temperatures in period 2 are lower than ZnO_xP_y's melting point. Thus, oxidation generates a thicker and thicker ZnO layer on the core region's ZnO_xP_y and the sphere structures are maintained in the whole growth process. In Zone 2, this ZnO layer would serve as self-catalytic seeds from which the ZnO nanowires could grow using the supplied Zn and O_2 vapors. In Zone 3, however, even lower local temperature does not support the ZnO nanowire growth at the surface of microsphere.

4.5 Summary

In this study, we synthesized ZnO sea urchins using a facile chemical vapor transport method. ZnO sea urchins were readily created by an evaporation and condensation process of source vapors without the need for prefabricated micro-scaled spherical templates. XRD patterns showed that these structures are mainly ZnO. Lattice-resolved and EDS mapping images using HRTEM indicated that the outer structures in the sea urchin are ZnO nanowires with the c-axis of wurtzite grown on the oxidized surface. However, in a control experiment, annealing the as-grown sea urchins and microspheres verified that these structures are not pure ZnO. Based on the material's characterization and the control experiment, we proposed the growth mechanism of the sea urchins; a ZnO layer develops on the surface of the ZnO_xP_y core microsphere, a mixed phase of Zn_3P_2 and ZnO, serving as a self catalyst for the growth of ZnO nanowires. Through this study, we developed the facile methodology for synthesizing large-scale ZnO nanowires growth and integrating of 1-D and 3-D structures. We understand that in order to form high quality sea urchin structures, the local temperature and the precursor concentration are all very important factors. With the detailed understanding of the growth mechanism, we can design new process that can produce uniform sea urchin structures over large areas by controlling temperature and the heating/cooling process.

5. Summary and Future Research Directions

Along with carbon nanotubes and silicon nanowires, the study of ZnO nanostructures has been over the past decade one of the most active research areas in the nanoscience community because of the distinctive optical, piezoelectric, and magnetic properties of these structures and their eco-friendliness[28]. Since the first report of ZnO nanobelts in 2001, various morphologies of ZnO nanostructures have been reported[129-131]. All of these morphologies can be made by using either a chemical vapor transport method or a solution-based method; neither approach requires expensive and complex instruments[62,91,92,98,130]. The morphological diversity of ZnO nanostructures is truly exceptional compared with other nanomaterials[28]. Although various shapes of ZnO nanostructures have been reported, no systematic studies have been undertaken to analyze their growth mechanism with the goal of understanding the principles that govern the creation of complex nanostructures. In the nanoscale realm, sensitive synthetic conditions and doping trials to increase conductance easily alter the material properties. Previous reports have not provided comprehensive information, only incremental details. These are the reasons why my research has focused on the synthesis, doping, and growth mechanism of ZnO nanostructures as fundamental studies.

After discovering that sulfur-doped ZnO powder, made using 900-1000^{o}C annealing in vacuum environment, shows a 10^5 increase in the intensity of visible emissions compared with the intensity of its UV emission, we successfully synthesized sulfur-doped ZnO nanostructures using a facile solution method at 90-100°C. To execute sulfur doping into ZnO nanowires, we chose thiourea ($SC(NH_2)_2$) as the sulfur doping source and added this into the nanowire growth solution, which was a mixture of zinc nitrate and hexamine in water. As the concentration of thiourea increased, hexagonal-shaped ZnO nanowires gradually evolved into hexagonal-shaped ZnO nanostructures termed ZnO nanostars. Density functional theory calculations suggested that the evolution from hexagonal nanowires to nanostars during growth occurs because sulfur atoms prefer to attach to the hexagonal vertices. More interestingly, the enhancement of green light emissions was accompanied by structural variations caused by sulfur adhering to the ZnO material. This phenomenon indicates that sulfur components in a ZnO nanostructure make an efficient radiative channel for green light emission. For a deeper understanding of the fundamental light emission mechanism of ZnO nanostructures, a future theoretical model will have to be established based on a range of optical measurements.

As a second project, the manufacture of well-aligned vertical ZnO nanowires grown on the silicon wafer is an indispensable task in commercializing the promising optical properties of ZnO nanostructures into optoelectronic devices. Light-emitting diodes and solar cells made using ZnO nanowires indicated that orientation, length, and spacing between nanowires significantly affect device performance. Previous studies addressed lattice matching between gold catalysts and sapphire (Al_2O_3) or gallium nitride (GaN) substrates to grow an ordered array of ZnO nanowires. Despite the remarkable progress on this issue, nonconductive and expensive substrates are not suitable engineering devices. Thus, we focused on a homoepitaxy method using ZnO nanocrystal seeds coated on a silicon substrate to make an affordable and versatile product. Previous studies suggested synthetic routes to generate zinc hydroxide ($Zn(OH)_2$) particles in the solution, deriving them from either zinc acetate combined with sodium hydroxide (NaOH) or potassium hydroxide (KOH), or by simply using zinc acetate alone. In our own experiments, we have noticed that at low concentrations of NaOH, the seed solution containing zinc hydroxide ($Zn(OH)_2$) particles led to vertically aligned nanowires. At higher concentrations of NaOH, higher amounts of hydroxide anion (OH^-) produced zincate ion ($Zn(OH)_4^{2-}$) that led to randomly oriented nanowires. Because in our experiments the methods failed to yield vertically aligned ZnO nanowires, we instead decided to study the formative mechanism underlying the preference of ZnO nanocrystal seeds for a c-axis orientation that leads to vertically aligned nanowires. As zincate ions dry on the surface, Na (or K) is incorporated into the seed material to maintain charge neutrality. These metallic impurities, upon annealing, tend to disorient the crystal axis of the ZnO seeds on the surface. When we changed the base needed for the formation of ZnO nanocrystalline seeds to ammonium hydroxide (NH_4OH), well-aligned vertical ZnO nanowire arrays with high surface coverage were obtained consistently at all concentrations of NH_4OH. This novel method permits the use of silicon substrates for the growth of vertically aligned nanowires, making ZnO nanostructures compatible with widely used silicon fabrication technology.

As a third project, we successfully synthesized sea urchin-like structures, termed sea urchins[120,121]. These are micro-sized architecture in which a core spherical structure is the growth base for an array of nanowires. Compared with a planar configuration, such structures offer an increase in the effective surface area of the nanowire array. In previous reports, devices such as dye-sensitized solar cells (DSSCs) that were made using ZnO sea-urchin structures have shown higher efficiency than those of simple nanowires arrays[125]. The success of these devices is in large part because of the superior density of the nanowire arrays; this density is owed to the three dimensional base morphology that allows a more efficient use of the substrate surface area. The most important property of the sea urchins obtained in our experiments was the mixed Zn_3P_2 and ZnO phase that composes the core of the microspheres. This core is encapsulated in a ZnO shell on which ZnO nanowires are grown. These compositions could offer the possibility that these structures are p-type ZnO semiconductors. The facile synthesis of these structures has therefore been the subject of great interest and research. Previous efforts to create ZnO nanowire arrays that utilize a three dimensional growth base, namely the sea urchin configuration, have proved successful only if the spherical core is already present at the time of ZnO deposition. To do this, previous work has used prefabricated templates for spherical growth sites. Such synthetic techniques proved complicated and inefficient. To overcome these problems, we developed a novel, efficient, and facile synthetic method for creating the ZnO sea urchin. By simply adding Zn_3P_2 powder to the C (graphite) and ZnO source powders used to grow ZnO nanowires in an evaporation-condensation synthetic method, we are able to create ZnO sea urchin structures easily and efficiently. The facile method for synthesis of ZnO sea urchins facilitates the preparation of higher ordered arrays of ZnO nanowires. Through control experiments we discovered the growth mechanism of such structures; the oxidation of Zn_3P_2 is the key to the formation of micro-scaled spherical structures during and after the condensation process. Moreover, a ZnO shell layer on the ZnO_xP_y microsphere serves as a self-catalyzing growth base for a ZnO nanowire array. The important issue, naturally proposing the next research direction, is the fact that detailed material characterizations using TEM, EDS and XRD did not show any conclusive evidence for the presence of pure Zn_3P_2 or P atoms in the sea urchins. Only control experiments in which the as-grown sea urchins were annealed at 700^{o}C, and the observation of Zn_3P_2 condensation and oxidation suggests a mixed Zn_3P_2 and ZnO phase core structure in the form of ZnO_xP_y. Thus, more correct and detailed material characterizations, which could be cryogenic- and time-resolved photoluminescence measurements, are needed to analyze the exact compositions of sea urchins. In addition, electrical measurements using nanowire field-effect-transistor (FET), fabricated by detached nanowires from sea urchins, would provide strong evidence of the presence of p-type ZnO nanowires in sea urchins.

References

1. Xia, Y. *et al*. One-Dimensional Nanostructures: Synthesis, Characterization, and Applications. *Advanced Materials* **15**, 353-389, doi:10.1002/adma.200390087 (2003).

2. Wang, X. Large-Scale Patterned Oxide Nanostructure: Fabrication, Characterization and Applications. *Ph.D. dissertation, School of Material Science and Engineering of the Georgia Institute of Technology* (2005).

3. Moore, G. E. Cramming more components onto integrated circuits. *Electronics* **38** (1965).

4. The international technology roadmap for semiconductor (IRTS) (2004).

5. Yabumoto, N., Oshima, M., Michikami, O. & Yoshii, S. Surface Damage on Si Substrates Caused by Reactive Sputter Etching. *Japanese Journal of Applied Physics* **20**, 893-900, doi:10.1143/JJAP.20.893 (1981).

6. Hah, J. H. *et al.* Converging lithography by combination of electrostatic layer-by-layer self-assembly and 193 nm photolithography: Top-down meets bottom-up. *Journal of Vacuum Science & Technology B: Microelectronics and Nanometer Structures* **24**, 2209-2213 (2006).

7. Ulijn, R. V. & Smith, A. M. Designing peptide based nanomaterials. *Chemical Society Reviews* **37**, 664-675, doi:10.1039/b609047h (2008).

8. Lu, W. & Lieber, C. M. Nanoelectronics from the bottom up. *Nature Materials* **6**, 841-850 (2007).

9. Liu, R., Wu, D., Feng, X. & Müllen, K. Bottom-Up Fabrication of Photoluminescent Graphene Quantum Dots with Uniform Morphology. *Journal of the American Chemical Society* **133**, 15221-15223, doi:10.1021/ja204953k (2011).

10. Vieu, C. *et al.* Electron beam lithography: resolution limits and applications. *Applied Surface Science* **164**, 111-117, doi: http://dx.doi.org/10.1016/S0169-4332(00)00352-4 (2000).

11. Gao, P. Piezoelectric nanostructures of ZnO: Synthesis, characterization and devices. *Ph.D. dissertation, School of Material Science and Engineering of the Georgia Institute of Technology* (2005).

12. Xia, Y. & Whitesides, G. M. SOFT LITHOGRAPHY. *Annual Review of Materials Science* **28**, 153-184, doi:doi:10.1146/annurev.matsci.28.1.153 (1998).

13. Yang, P., Yan, R. & Fardy, M. Semiconductor Nanowire: What's Next? *Nano Letters* **10**, 1529-1536, doi:10.1021/nl100665r (2010).

14. Yan, R., Gargas, D. & Yang, P. Nanowire photonics. *Nature Photonics* **3**, 569-576 (2009).

15. Goldberger, J., Sirbuly, D. J., Law, M. & Yang, P. ZnO Nanowire Transistors. *The Journal of Physical Chemistry B* **109**, 9-14, doi:10.1021/jp0452599 (2004).

16. Wan, Q. *et al.* Fabrication and ethanol sensing characteristics of ZnO nanowire gas sensors. *Applied Physics Letters* **84**, 3654-3656, doi:10.1063/1.1738932 (2004).

17. Gudiksen, M. S., Lauhon, L. J., Wang, J., Smith, D. C. & Lieber, C. M. Growth of nanowire superlattice structures for nanoscale photonics and electronics. *Nature* **415**, 617-620 (2002).

18. Bao, J., Zimmler, M. A., Capasso, F., Wang, X. & Ren, Z. F. Broadband ZnO Single-Nanowire Light-Emitting Diode. *Nano Letters* **6**, 1719-1722, doi:10.1021/nl061080t (2006).

19. Hayden, O., Greytak, A. B. & Bell, D. C. Core–Shell Nanowire Light-Emitting Diodes. *Advanced Materials* **17**, 701-704, doi:10.1002/adma.200401235 (2005).

20. Zhang, X.-M., Lu, M.-Y., Zhang, Y., Chen, L.-J. & Wang, Z. L. Fabrication of a High-Brightness Blue-Light-Emitting Diode Using a ZnO-Nanowire Array Grown on p-GaN Thin Film. *Advanced Materials* **21**, 2767-2770, doi:10.1002/adma.200802686 (2009).

21. Qian, F. *et al.* Multi-quantum-well nanowire heterostructures for wavelength-controlled lasers. *Nature Materials* **7**, 701-706 (2008).

22. Law, M., Greene, L. E., Johnson, J. C., Saykally, R. & Yang, P. Nanowire dye-sensitized solar cells. *Nature Materials* **4**, 455-459 (2005).

23. Law, J. B. K. & Thong, J. T. L. Simple fabrication of a ZnO nanowire photodetector with a fast photoresponse time. *Applied Physics Letters* **88**, 133114, doi:10.1063/1.2190459 (2006).

24. Soci, C. *et al.* ZnO Nanowire UV Photodetectors with High Internal Gain. *Nano Letters* **7**, 1003-1009, doi:10.1021/nl070111x (2007).

25. Greytak, A. B., Barrelet, C. J., Li, Y. & Lieber, C. M. Semiconductor nanowire laser and nanowire waveguide electro-optic modulators. *Applied Physics Letters* **87**, doi:http://dx.doi.org/10.1063/1.2089157 (2005).

26. Huang, M. H. *et al.* Room-temperature ultraviolet nanowire nanolasers. *Science* **292**, 1897-1899 (2001).

27. Johnson, J. C. *et al.* Single gallium nitride nanowire lasers. *Nature Materials* **1**, 106-110 (2002).

28. Wang, Z. L. Splendid One-Dimensional Nanostructures of Zinc Oxide: A New Nanomaterial Family for Nanotechnology. *ACS Nano* **2**, 1987-1992, doi:10.1021/nn800631r (2008).

29. http://en.wikipedia.org/wiki/Miller_index.

30. Morkoç, H. & Özgür, Ü. Zinc Oxide fundamentals, materials and device technology. *WILEY-VCH*, 4-6 (2007).

31. Choi, S. Spectroscopic ellipsometry of group-III adatom kinetics on III-V semiconductor surfaces. *Ph.D. dissertation, Department of Physics of Duke University* (2007).

32. Wang, Z. L. ZnO nanowire and nanobelt platform for nanotechnology. *Materials Science and Engineering R* **64**, 33-71, doi:10.1016/j.mser.2009.02.001 (2009).

33. Özgür, Ü. *et al.* A comprehensive review of ZnO materials and devices. *Journal of Applied Physics* **98**, 041301(041301) - 041301(041103), doi:Artn 041301
doi 10.1063/1.1992666 (2005).

34. Kong, X. Y. & Wang, Z. L. Spontaneous Polarization-Induced Nanohelixes, Nanosprings, and Nanorings of Piezoelectric Nanobelts. *Nano Letters* **3**, 1625-1631, doi:10.1021/nl034463p (2003).

35. Wang, Z. L. Self-assembled nanoarchitectures of polar nanobelts/nanowires. *Journal of Materials Chemistry* **15**, 1021-1024, doi:10.1039/b414550j (2005).

36. Schubert, E. F. & Kim, J. K. Solid-State Light Sources Getting Smart. *Science* **308**, 1274-1278, doi:10.1126/science.1108712 (2005).

37. Liu, J. & Kim, J. High Efficiency Light Emitting Diodes using Nanostructured ZnO (Research Funding Proposal). *National Science Foundation (NSF)*, ECCS-0925587 (2010).

38. Littlefair, P. J. The luminous efficacy of daylight: a review. *Lighting Research and Technology* **17**, 162-182, doi:10.1177/14771535850170040401 (1985).

39. Kim, J. S. *et al.* White-light generation through ultraviolet-emitting diode and white-emitting phosphor. *Applied Physics Letters* **85**, 3696-3698, doi:10.1063/1.1808501 (2004).

40. Narendran, N., Gu, Y., Freyssinier, J. P., Yu, H. & Deng, L. Solid-state lighting: failure analysis of white LEDs. *Journal of Crystal Growth* **268**, 449-456, doi:http://dx.doi.org/10.1016/j.jcrysgro.2004.04.071 (2004).

41. Pimputkar, S., Speck, J. S., DenBaars, S. P. & Nakamura, S. Prospects for LED lighting. *Nature Photonics* **3**, 180-182 (2009).

42. Foreman, J. V. Photoexcited Emission Efficiencies of Zinc Oxide. *Ph.D. dissertation, Department of Physics of Duke University* (2009).

43. Willander, M. *et al.* Zinc oxide nanorod based photonic devices: recent progress in growth, light emitting diodes and lasers. *Nanotechnology* **20**, 332001(332001) - 332001(332040), doi:10.1088/0957-4484/20/33/332001 (2009).

44. Edmond, J., Kong, H., Suvorov, A., Waltz, D. & Carter, J. C. 6H-Silicon Carbide Light Emitting Diodes and UV Photodiodes. *physica status solidi (a)* **162**, 481-491, doi:10.1002/1521-396x(199707)162:1<481::aid-pssa481>3.0.co;2-o (1997).

45. Robinson, R. J. & Kun, Z. K. p-n junction zinc sulfo-selenide and zinc selenide light-emitting diodes. *Applied Physics Letters* **27**, 74-76, doi:10.1063/1.88358 (1975).

46. Lim, J. H. *et al.* UV Electroluminescence Emission from ZnO Light-Emitting Diodes Grown by High-Temperature Radiofrequency Sputtering. *Advanced Materials* **18**, 2720-2724, doi:10.1002/adma.200502633 (2006).

47. Zhou, J., Xu, N. S. & Wang, Z. L. Dissolving Behavior and Stability of ZnO Wires in Biofluids: A Study on Biodegradability and Biocompatibility of ZnO Nanostructures. *Advanced Materials* **18**, 2432-2435, doi:10.1002/adma.200600200 (2006).

48. Qian, F. *et al.* Gallium Nitride-Based Nanowire Radial Heterostructures for Nanophotonics. *Nano Letters* **4**, 1975-1979, doi:10.1021/nl0487774 (2004).

49. Look, D. C. & Claflin, B. P-type doping and devices based on ZnO. *physica status solidi (b)* **241**, 624-630, doi:10.1002/pssb.200304271 (2003).

50. Look, D. C., Claflin, B., Alivov, Y. I. & Park, S. J. The future of ZnO light emitters. *Physica Status Solidi a-Applied Research* **201**, 2203-2212, doi:DOI 10.1002/pssa.200404803 (2004).

51. Minegishi, K. *et al.* Growth of p-type Zinc Oxide Films by Chemical Vapor Deposition. *Japanese Journal of Applied Physics* **36**, L1453-L1455, doi:10.1143/JJAP.36.L1453 (1997).

52. Park, C. H., Zhang, S. B. & Wei, S.-H. Origin of p-type doping difficulty in ZnO: The impurity perspective. *Physical Review B* **66**, 073202 (2002).

53. Chu, S. *et al.* Electrically pumped waveguide lasing from ZnO nanowires. *Nature Nanotechnoloy* **6**, 506-510 (2011).

54. Kim, K.-K., Kim, H.-S., Dae-Kue, H., Jae-Hong, L. & Park, S.-J. Realization of p-type ZnO thin films via phosphorus doping and thermal activation of the dopant. *Applied Physics Letters* **83**, 63-65, doi:10.1063/1.1591064 (2003).

55. Xiang, B. *et al.* Rational Synthesis of p-Type Zinc Oxide Nanowire Arrays Using Simple Chemical Vapor Deposition. *Nano Letters* **7**, 323-328, doi:10.1021/nl062410c (2006).

56. Yuan, G. D. *et al.* p-Type ZnO Nanowire Arrays. *Nano Letters* **8**, 2591-2597, doi:10.1021/nl073022t (2008).

57. Teke, A. *et al.* Excitonic fine structure and recombination dynamics in single-crystalline ZnO. *Physical Review B* **70**, 195207 (2004).

58. Meyer, B. K. *et al.* Bound exciton and donor–acceptor pair recombinations in ZnO. *physica status solidi (b)* **241**, 231-260, doi:10.1002/pssb.200301962 (2004).

59. Reynolds, D. C. *et al.* Neutral-donor–bound-exciton complexes in ZnO crystals. *Physical Review B* **57**, 12151-12155 (1998).

60. Ding, M. *et al.* The p-type ZnO film realized by a hydrothermal treatment method. *Applied Physics Letters* **98**, 062102-062102-062103, doi:10.1063/1.3549304 (2011).

61. Hwang, D.-K. *et al.* Study of the photoluminescence of phosphorus-doped p-type ZnO thin films grown by radio-frequency magnetron sputtering. *Applied Physics Letters* **86**, 151917-151917-151913, doi:10.1063/1.1895480 (2005).

62. Greene, L. E. *et al.* Low-Temperature Wafer-Scale Production of ZnO Nanowire Arrays. *Angewandte Chemie International Edition* **42**, 3031-3034 (2003).

63. Wang, X., Summers, C. J. & Wang, Z. L. Large-Scale Hexagonal-Patterned Growth of Aligned ZnO Nanorods for Nano-optoelectronics and Nanosensor Arrays. *Nano Letters* **4**, 423-426, doi:10.1021/nl035102c (2004).

64. Wang, F. *et al.* Solution−Liquid−Solid Growth of Semiconductor Nanowires. *Inorganic Chemistry* **45**, 7511-7521, doi:10.1021/ic060498r (2006).

65. Pacholski, C., Kornowski, A. & Weller, H. Self-Assembly of ZnO: From Nanodots to Nanorods. *Angewandte Chemie International Edition* **41**, 1188–1191 (2002).

66. Vayssieres, L., Keis, K., Hagfeldt, A. & Lindquist, S.-E. Three-Dimensional Array of Highly Oriented Crystalline ZnO Microtubes. *Chemistry of Materials* **13**, 4395-4398, doi:10.1021/cm011160s (2001).

67. Wei, A. *et al.* Growth mechanism of thbular ZnO formed in aqueous solution. *Nanotechnology* **17**, 1740- 1744, doi:10.1088/0957-4484/17/6/033 (2006).

68. Geng, B. Y. *et al.* Synthesis and optical properties of S-doped ZnO nanowires. *Applied Physics Letters* **82**, 4791-4793, doi:10.1063/1.1588735 (2003).

69. Schmidt-Mende, L. & MacManus-Driscoll, J. L. ZnO – nanostructures, defects, and devices. *Materials Today* **10**, 40-48, doi:http://dx.doi.org/10.1016/S1369-7021(07)70078-0 (2007).

70. Kröger, F. A. The Chemistry of Imperfect Crystals. *North Holland, Amsterdam* **2nd Edition**, 73 (1974).

71. Djurišić, A. B. *et al.* Photoluminescence and electron paramagnetic resonance of ZnO tetrapod structure. *Advanced Functional Materials* **14**, 856-864, doi:DOI 10.1002/adfm.20030582 (2004).

72. Djurišić, A. B. & Leung, Y. H. Optical Properties of ZnO Nanostructures. *Small* **2**, 944-961, doi:10.1002/smll.200600134 (2006).

73. Chen, Y. Q. *et al.* Growth mechanism and characterization of ZnO microbelts and self-assembled. *Materials Letters* **59**, 3280-3283, doi:DOI 10.1016/j.matlet.2005.05.059 (2005).

74. Meng, X. Q. *et al.* The structural and optical properties of ZnO nanorod arrays. *Solid State Communications* **135**, 179-182, doi:DOI 10.1016/j.ssc.2005.04.015 (2005).

75. Wang, R. C., Liu, C. P., Huang, J. L. & Chen, S. J. ZnO symmetric nanosheets integrated with nanowalls. *Applied Physics Letters* **87**, 053103, doi:Artn 053103 Doi 10.1063/1.2005386 (2005).

76. Chen, Z. *et al.* Effect of N_2 flow rate on morphology and structure of ZnO nanocrystals synthesized via vapor deposition. *Scripta Materialia* **52**, 63-67, doi:10.1016/j.scriptamat.2004.08.024 (2005).

77. Ng, H. T. *et al.* Optical properties of single-crystalline ZnO nanowires on m-sapphire. *Applied Physics Letters* **82**, 2023-2025, doi:Doi 10.1063/1.1564870 (2003).

78. Lin, B., Zhuxi, F. & Jia, Y. Green luminescent center in undoped zinc oxide films deposited on silicon substrates. *Applied Physics Letters* **79**, 943-945, doi:10.1063/1.1394173 (2001).

79. Yang, Q., Tang, K., Zuo, J. & Qian, Y. Synthesis and luminescent property of single-crystal ZnO nanobelts by a simple low temperature evaporation route. *Applied Physics A* **79**, 1847-1851, doi:10.1007/s00339-004-2939-9 (2004).

80. Liu, X., Wu, X. H., Cao, H. & Chang, R. P. H. Growth mechanism and properties of ZnO nanorods synthesized by plasma-enhanced chemical vapor deposition. *Journal of Applied Physics* **95**, 3141-3147, doi:Doi 10.1063/1.1646440 (2004).

81. Garces, N. Y. *et al.* Role of copper in the green luminescence from ZnO crystals. *Applied Physics Letters* **81**, 622-624, doi:Doi 10.1063/1.1494125 (2002).

82. Reynolds, D. C., Look, D. C. & Jogai, B. Fine structure on the green band in ZnO. *Journal of Applied Physics* **89**, 6189-6191 (2001).

83. Heo, Y. W., Norton, D. P. & Pearton, S. J. Origin of green luminescence in ZnO thin film grown by molecular-beam epitaxy. *Journal of Applied Physics* **98**, 073502, doi:10.1063/1.2064308 (2005).

84. Zhao, Q. X. *et al.* Deep-level emissions influenced by O and Zn implantations in ZnO. *Applied Physics Letters* **87**, 211912, doi:Artn 211912
Doi 10.1063/1.2135880 (2005).

85. Kresse, G. & Furthmüller, J. Efficiency of ab-initio total energy calculations for metals and semiconductors using a plane-wave basis set. *Computational Materials Science* **6**, 15-50, doi:http://dx.doi.org/10.1016/0927-0256(96)00008-0 (1996).

86. Kresse, G. & Hafner, J. Ab initio molecular dynamics for open-shell transition metals. *Physical Review B* **48**, 13115-13118 (1993).

87. Wang, Y. & Perdew, J. P. Correlation hole of the spin-polarized electron gas, with exact small-wave-vector and high-density scaling. *Physical Review B* **44**, 13298-13307 (1991).

88. Monkhorst, H. J. & Pack, J. D. Special points for Brillouin-zone integrations. *Physical Review B* **13**, 5188-5192 (1976).

89. Yu, D., , T. T., , J. T. M., , V. C. & Taylor, C. R. ZnO Nanowires Synthesized by Vapor Phase Transport Deposition on Transparent Oxide Substrates. *Nanoscale Research Letters* **5**, 1333-1339 (2010).

90. Lu, W. & Leber, C. M. Topical Review: Semiconductor nanowires. *Journal of Physics D: Applied Physics*, R387 - R406 (2006).

91. Huang, M. H. *et al.* Room-temperature ultraviolet nanowire nanolasers. *Science* **292**, 1897-1899 (2001).

92. Greene, L. E. *et al.* General Route to Vertical ZnO Nanowire Arrays Using Textured ZnO Seeds. *Nano Letters* **5**, 1231-1236 (2005).

93. Wang, X., Song, J. & Wang, Z. L. Nanowire and nanobelt arrays of zinc oxide from synthesis to properties and to novel devices. *Journal of Materials Chemistry* **17**, 711 - 720, doi:10.1039/b616963p (2007).

94. Lucas, M., Wang, Z. L. & Riedo, E. Growth direction and morphology of ZnO nanobelts revealed by combining in situ atomic force microscopy and polarized Raman spectroscopy. *Physical Review B* **81**, 045415 (045411-045415), doi:10.1103/PhysRevB.81.045415 (2010).

95. Wu, Y. & Yang, P. Direct Observation of Vapor-Solid-Liquid Nanowire Growth. *Journal of American Chemical Society* **123**, 3165 - 3166, doi:10.1021/ja0059084 (2001).

96. Wang, Z. L., Kong, X. Y. & Zuo, J. M. Induced Growth of Asymmetric Nanocantilever Arrays on Polar Surfaces. *Physical Review Letters* **91**, 185502 (185501-185504), doi:10.1103/PhysRevLett.91.185502 (2003).

97. Wang, X. *et al.* Growth of Uniformly Aligned ZnO Nanowire Heterojunction Arrays on GaN, AlN, and $Al_{0.5}Ga_{0.5}N$ Substrates. *Journal of The American Chemical Society* **127**, 7920–7923 (2005).

98. Park, W. I., Kim, D. H., Jung, S.-W. & Yi, G.-C. Metalorganic vapor-phase epitaxial growth of vertically well-aligned ZnO nanorods. *Applied Physics Letters* **80**, 4232 - 4234, doi:10.1063/1.1482800 (2002).

99. Weintraub, B., Wei, Y. & Wang, Z. L. Optical Fiber/Nanowire Hybrid Structures for Efficient Three-Dimensional Dye-Sensitized Solar Cells. *Angewandte Chemie International Edition* **48**, 8981–8985 (2009).

100. Xu, S. *et al.* Ordered Nanowire Array Blue/Near-UV Light Emitting Diodes. *Advanced Materials* **22**, 4749–4753 (2010).

101. Newton, M. C., Leake, S. J., Harder, R. & Robinson, I. K. Three-dimensional imaging of strain in a single ZnO nanorod. *Nature Materials* **9**, 120–124 (2010).

102. Utama, M. I. B. *et al.* Vertically Aligned Cadmium Chalcogenide Nanowire Arrays on Muscovite Mica: A Demonstration of Epitaxial Growth Strategy. *Nano Letters* **11**, 3051–3057 (2010).

103. Wei, Y. *et al.* Wafer-Scale High-Throughput Ordered Growth of Vertically Aligned ZnO Nanowire Arrays. *Nano Letters* **10**, 3414–3419 (2010).

104. Xu, S. *et al.* Patterned Growth of Vertically Aligned ZnO Nanowire Arrays on Inorganic Substrates at Low Temperature without Catalyst. *Journal of The American Chemical Society* **130**, 14958–14959 (2008).

105. Kim, Y.-J. *et al.* Controlled selective growth of ZnO nanorod and microrod arrays on Si substrates by a wet chemical method. *Applied Physics Letters* **89**, 163128 (2006).

106. Lu, M.-P. *et al.* Piezoelectric Nanogenerator Using p-Type ZnO Nanowire Arrays. *Nano Letters* **9**, 1223–1227 (2009).

107. Alias, S. S., Ismail, A. B. & Mohamad, A. A. Effect of pH on ZnO nanoparticle properties synthesized by sol-gel centrifugation. *Journal of Alloys and Compounds* **499**, 231-237 (2010).

108. www.tedpella.com/grids_html/silicon-dioxide-details.htm.

109. Vayssieres, L. Growth of Arrayed Nanorods and Nanowires of ZnO from Aqueous Solutions. *Advanced Materials* **15**, 464 - 466, doi:10.1002/adma.200390108 (2003).

110. Shen, G., Bando, Y. & Golberg, D. Synthesis and Structures of High-Quality Single-Crystalline II3−V2 Semiconductors Nanobelts. *The Journal of Physical Chemistry C* **111**, 5044-5049, doi:10.1021/jp068792s (2007).

111. Shen, G. & Chen, D. One-Dimensional Nanostructures and Devices of II–V Group Semiconductors. *Nanoscale Research Letters* **4**, 779-788, doi:10.1007/s11671-009-9338-2 (2009).

112. Shen, G., Chen, P.-C., Bando, Y., Golberg, D. & Zhou, C. Single-Crystalline and Twinned Zn3P2 Nanowires: Synthesis, Characterization, and Electronic Properties. *The Journal of Physical Chemistry C* **112**, 16405-16410, doi:10.1021/jp806334k (2008).

113. Shen, G., Chen, P.-C., Bando, Y., Golberg, D. & Zhou, C. Bicrystalline Zn3P2 and Cd3P2 Nanobelts and Their Electronic Transport Properties. *Chemistry of Materials* **20**, 7319-7323, doi:10.1021/cm802516u (2008).

114. Xu, S. *et al.* Self-powered nanowire devices. *Nature Nanotechnology* **5**, 366 - 373 (2010).

115. Wang, Z. L. & Song, J. Piezoelectric Nanogenerators Based on Zinc Oxide Nanowire Arrays. *Science* **312**, 242-246 (2006).

116. Wang, X., Song, J., Liu, J. & Wang, Z. L. Direct-Current Nanogenerator Driven by Ultrasonic Waves. *Science* **316**, 102-105, doi:10.1126/science.1139366 (2007).

117. Vanheusden, K. *et al.* Mechanisms behind green photoluminescence in ZnO phosphor powders. *Journal of Applied Physics* **79**, 7983-7990, doi:10.1063/1.362349 (1996).

118. Foreman, J. V., Everitt, H. O., Yang, J. & Liu, J. Influence of temperature and photoexcitation density on the quantum efficiency of defect emission in ZnO powders. *Applied Physics Letters* **91**, 011902-011902-011903, doi:10.1063/1.2753540 (2007).

119. Yeh, P.-H., Li, Z. & Wang, Z. L. Schottky-Gated Probe-Free ZnO Nanowire Biosensor. *Advanced Materials* **21**, 4975-4978, doi:10.1002/adma.200902172 (2009).

120. Elias, J. *et al.* Hollow Urchin-like ZnO thin Films by Electrochemical Deposition. *Advanced Materials* **22**, 1607-1612, doi:10.1002/adma.200903098 (2010).

121. Shen, G., Bando, Y. & Lee, C.-J. Synthesis and Evolution of Novel Hollow ZnO Urchins by a Simple Thermal Evaporation Process. *The Journal of Physical Chemistry B* **109**, 10578-10583, doi:10.1021/jp051078a (2005).

122. Gu, Z., Paranthaman, M. P., Xu, J. & Pan, Z. W. Aligned ZnO nanorod arrays grown directly on zinc foils and zinc spheres by a low-temperature oxidization method. *ACS Nano* **3**, 273-278, doi:10.1021/nn800759y (2009).

123. Liu, B. & Zeng, H. C. Fabrication of ZnO "Dandelions" via a Modified Kirkendall Process. *Journal of the American Chemical Society* **126**, 16744-16746, doi:10.1021/ja044825a (2004).

124. Wang, X., Hu, P., Fangli, Y. & Yu, L. Preparation and Characterization of ZnO Hollow Spheres and ZnO−Carbon Composite Materials Using Colloidal Carbon Spheres as Templates. *The Journal of Physical Chemistry C* **111**, 6706-6712, doi:10.1021/jp070382w (2007).

125. Guerin, V. M., Elias, J., Nguyen, T. T., Philippe, L. & Pauporte, T. Ordered networks of ZnO-nanowire hierarchical urchin-like structures for improved dye-sensitized solar cells. *Physical Chemistry Chemical Physics* **14**, 12948-12955, doi:10.1039/c2cp42085f (2012).

126. Chu, T. L., Chu, S. S., Murthy, K., Stokes, E. D. & Russell, P. E. Deposition and properties of zinc phosphide films. *Journal of Applied Physics* **54**, 2063-2068, doi:10.1063/1.332254 (1983).

127. Yang, R. *et al.* Single-Crystalline Branched Zinc Phosphide Nanostructures: Synthesis, Properties, and Optoelectronic Devices. *Nano Letters* **7**, 269-275, doi:10.1021/nl062228b (2006).

128. Wu, P. *et al.* Novel Type-II Zn3P2/ZnO Core/Shell Nanowires: Synthesis, Characteristic, and Photoluminescence Properties. *Crystal Growth & Design* **11**, 1417-1421, doi:10.1021/cg101221z (2011).

129. Pan, Z. W., Dai, Z. R. & Wang, Z. L. Nanobelts of Semiconducting Oxides. *Science* **291**, 1947-1949, doi:10.1126/science.1058120 (2001).

130. Kong, X. Y., Ding, Y., Yang, R. & Wang, Z. L. Single-Crystal Nanorings Formed by Epitaxial Self-Coiling of Polar Nanobelts. *Science* **303**, 1348-1351, doi:10.1126/science.1092356 (2004).

131. Gao, P. X. *et al.* Conversion of Zinc Oxide Nanobelts into Superlattice-Structured Nanohelices. *Science* **309**, 1700-1704, doi:10.1126/science.1116495 (2005).

Biography

Jinhyun Cho

Place and Date of Birth

Incheon, Republic of Korea, January 19, 1979

Education and Experience

B.E., Inha University, Electronics Engineering, Incheon, Republic of Korea, 1999-2007

Military service as signal corpsman, 51st (Army) Division of the Republic of Korea, 1999-2001

Honors

Fellowship from Duke Graduate Certificate Program in Nanoscience for spring semester 2008

Honor student in fall semester of 2004

Publications

1. **Jinhyun Cho**, Qiubao Lin, Sungwoo Yang, Jay G. Simmons Jr., Yingwen Cheng, Erica Lin, Jianqiu Yang, John V. Foreman, Henry O. Everitt, Weitao Yang, Jungsang Kim and Jie Liu, "Sulfur-doped Zinc Oxide (ZnO) Nanostars: Synthesis and Simulation of Growth Mechanism," (Back Cover Picture) Nano Research, Vol. 5, Issue 1, 20-26 (2012).

2. **Jinhyun Cho**, Najah Salleh, Sungwoo Yang, Chul-Jin Lee, Young-Woo Kim, Jungsang Kim, Jie Liu, "Novel Synthetic Methodology for Controlling the Orientation of Zinc Oxide Nanowires Grown on Amorphous Silicon Oxide Substrates," accepted in Nanoscale (August, 2013)

3. **Jinhyun Cho**, Si-in Kim, Carlos Blanco, Jay G. Simmons Jr., Jaehong Park, Aubrey Temple, Gyeong Hee Lee, Kendall Dawkins, Bongsoo Kim, Henry O. Everitt, Jungsang Kim, Jie Liu, "Synthesis of ZnO Sea Urchin Structures Composed of a Core Containing a Mixture of Zn_3P_2 and ZnO ," manuscript preparation (2013)